November 1999 • NREL/SR-520-27535

Subcontractor Report

Efficiency and Throughput Advances in Continuous Roll-to-Roll a-Si Alloy PV Manufacturing Technology

Annual Technical Progress Report 22 June 1998 — 21 June 1999

M. Izu
Energy Conversion Devices, Inc.
Troy, Michigan

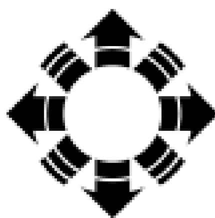

NREL

National Renewable Energy Laboratory

1617 Cole Boulevard
Golden, Colorado 80401-3393

NREL is a U.S. Department of Energy Laboratory
Operated by Midwest Research Institute • Battelle • Bechtel

Contract No. DE-AC36-98-GO10337

November 1999 • NREL/SR-520-27535

Efficiency and Throughput Advances in Continuous Roll-to-Roll a-Si Alloy PV Manufacturing Technology

Annual Technical Progress Report 22 June 1998 — 21 June 1999

M. Izu
Energy Conversion Devices, Inc.
Troy, Michigan

NREL Technical Monitor: R.L. Mitchell

Prepared under Subcontract No. ZAX-8-17647-09

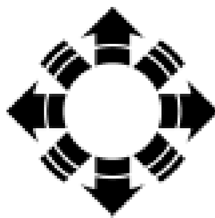

National Renewable Energy Laboratory

1617 Cole Boulevard
Golden, Colorado 80401-3393

NREL is a U.S. Department of Energy Laboratory
Operated by Midwest Research Institute • Battelle • Bechtel

Contract No. DE-AC36-98-GO10337

NOTICE

This report was prepared as an account of work sponsored by an agency of the United States government. Neither the United States government nor any agency thereof, nor any of their employees, makes any warranty, express or implied, or assumes any legal liability or responsibility for the accuracy, completeness, or usefulness of any information, apparatus, product, or process disclosed, or represents that its use would not infringe privately owned rights. Reference herein to any specific commercial product, process, or service by trade name, trademark, manufacturer, or otherwise does not necessarily constitute or imply its endorsement, recommendation, or favoring by the United States government or any agency thereof. The views and opinions of authors expressed herein do not necessarily state or reflect those of the United States government or any agency thereof.

Available electronically at http://www.doe.gov/bridge

Available for a processing fee to U.S. Department of Energy and its contractors, in paper, from:

U.S. Department of Energy
Office of Scientific and Technical Information
P.O. Box 62
Oak Ridge, TN 37831-0062
phone: 865.576.8401
fax: 865.576.5728
email: reports@adonis.osti.gov

Available for sale to the public, in paper, from:
U.S. Department of Commerce
National Technical Information Service
5285 Port Royal Road
Springfield, VA 22161
phone: 800.553.6847
fax: 703.605.6900
email: orders@ntis.fedworld.gov
online ordering: http://www.ntis.gov/ordering.htm

Printed on paper containing at least 50% wastepaper, including 20% postconsumer waste

PREFACE

This Phase I annual technical progress report covers the work performed by Energy Conversion Devices, Inc. (ECD) for the period of June 22, 1998 through June 21, 1999 under DOE/NREL Subcontract No. ZAX-8-17647-09 entitled "Efficiency and Throughput Advances in Continuous Roll-to-Roll a-Si Alloy PV Manufacturing Technology." This is the first Annual Technical Progress Report for this subcontract. The subcontract is scheduled to be performed from June 22, 1998 through June 21, 2001. The following personnel at ECD have participated in this program:

Hank Bianchi
Gennady Bondarenko
Ray Crucet
Joe Doehler
Tim Ellison
Eric Haggard
Masat Izu
Scott Jones
Rob Kopf
Arun Kumar
Art Myatt
Herb Ovshinsky

This program has been supported by the following United Solar personnel:

Eric Akkashian
Arindam Banerjee
Jon Call
Subhendu Guha
Kevin Hoffman
Mark Lycette
Gerard Pietka
Mike Walters
Jeff Yang

This program has also been supported by our subcontractor Scientific Applications International Corp. (SAIC). SAIC staff that worked on this program include:

Ellis Hyman
Barton Lane

EXECUTIVE SUMMARY

The objective of this program over the three-year period is to continue to advance ECD's amorphous silicon (a-Si) solar cell PV manufacturing technology to improve the stable module efficiency to increase the throughput, to reduce the manufacturing costs, and to pave the way for production expansion. The three-year goal is to achieve a 25-30% reduction in module cost ($/W) and a 60% increase in manufacturing capacity (MW/Year) over the United Solar's 1997 4th Quarter annual manufacturing capacity.

To achieve this objective, ECD shall perform the following tasks:

1. Development, design and installation of improved heating system for United Solar's continuous roll-to-roll a-Si deposition machine,
2. Development of new in-line hardware and software cell diagnostic systems that can be used for in-line QA/QC and on-line continuous process optimization,
3. Advance the new backreflector deposition process in order to reduce the cost and to obtain higher deposition rates,
4. Development of a new cathode hardware design which will demonstrate and improve solar cell performance and deposition uniformity.

During the first-year Phase I program, ECD proposed to perform the following four tasks:

Task 1:	Process Control Improvements: Substrate Heating and Temperature Monitoring Systems
Task 2:	Process Control Improvements: In-Line Characterization Sensors
Task 3:	Improvements to Backreflector Deposition Process
Task 4:	Improvements in the a-Si Deposition Cathode Configuration

Major Accomplishments in this Phase I Program:

1. Completed design and construction of new, improved substrate heater.
2. Tested and verified improved performance of the new substrate heater in the pilot machine.
3. Verified improved performance of the new substrate heater in the production machine.
4. Designed and bench-tested a new infrared temperature sensor.
5. Installed a prototype new infrared temperature sensor in the production machine for evaluation.
6. Designed a new rolling thermocouple temperature sensor.
7. Designed and bench-tested a reflectometer for the backreflector deposition machine.
8. Designed and bench-tested in-line non-contacting cell diagnostic sensor; PV capacitive diagnostic (PVCD) system.
9. Installed the in-line cell diagnostic sensor in the 5 MW a-Si deposition machine for evaluation.
10. Demonstrated a new low-cost zinc metal process in the pilot backreflector machine.
11. Fully tested a new cathode design for improved uniformity.

TABLE OF CONTENTS

	Page
Preface	2
Executive Summary	3
Table of Contents	4
List of Figures	6
List of Tables	8
Background	9
Overview of ECD/United Solar's PV Manufacturing Technology	9
Current Manufacturing Procedures	10
Advantages of the Present Manufacturing Process	12
Problems with the Present Manufacturing Process	12
Task 1 - Process Control Improvements: New Substrate Heating and Temperature Monitoring Systems	14
The New Substrate Heating System	14
Introduction	14
System Design	14
Work Performed	15
Summary Evaluation: Improved Substrate Heaters	17
New Temperature Monitoring Systems	19
Introduction	19
IR Temperature Sensor	19
Description of IR Temperature Sensors	21
Rolling Thermocouple Concept	23
Testing the New Temperature Monitoring Systems	23
Task 2 - Process Control Improvements: Development of In-Line Sensors and Diagnostic Systems	25
Introduction	25
Backreflector Characterization Sensors	26
Objectives	26
Benchtop System Descriptions	26
Backreflector ZnO Film Thickness Measurement System	26
Backreflector Scatterometer	26
Data Analysis: Backreflector Scatterometer	28
Laser Diode Stability	28
Sample Measurements	28
Light I-V Correlation Studies	30
Correlation vs. Scattering Angle	30
Dependence of Diffuse Reflectance on Incident Angle	32
Data Analysis: ZnO Thickness Measurement	33
2nd Generation Sensor Development	33
Backreflector Scatterometer	33
Backreflector ZnO Film Thickness Measurement System	33
PV Capacitive Diagnostic (PVCD) System	34
Introduction	34
Principle Of Operation	34

TABLE OF CONTENTS (continued)

	Page
Bench-Top System Design	35
Establish Basic Operation	36
Compensation for Finite Time Constant	37
Measurement Reproducibility	38
Summary of Selected Preliminary Measurements	38
Design of the Second Generation Device for Installation in the 5 MW	40
Task 3 – Development of Reactive Sputtering Process Using Inexpensive Zn Metal Targets for Back Reflector Preparation	42
Background	42
Objective of Backreflector Studies	43
Experimental	43
Results of Work Completed During Phase I of the Program	44
Web Handling Procedures	44
Reactive Sputtering Optimization	46
Preparation for Tests in 5MW Production Machine	48
Plans for Phase II of the Program	49
Task 4 - Cathode Hardware Studies for a-Si(Ge):H i-layer Depositions	50
Background	50
Objective of Cathode Hardware Studies	51
Experimental	52
Results of Work Completed During Phase I of the Program	54
The 5MW Style Cathode in the Single R&D Chamber	54
Testing Similarity to Cathodes Used in Production	54
Attempts to Improve Uniformity Using 5 MW Style Cathode	56
Testing of New Cathode Design in the Single R&D Chamber	57
Establishment of Baseline "5MW-like" Cathode in Pilot Roll-to-Roll Machine	60
Plans for Phase II of the Program	60
Modeling for Amorphous Silicon Deposition	61
Introduction	61
Simulation Strategy	61
One-Point Simulations	62
RF-Global Simulation	62
The Boltzmann Code	63

LIST OF FIGURES

		Page
Figure A.	Structure of a triple-junction spectrum-splitting solar cell produced in the ECD/United Solar continuous roll-to-roll manufacturing process.	9
Figure B.	Schematic drawing of ECD's roll-to-roll solar cell deposition process.	10
Figure 1	Photograph of a quartz IR heating lamp from the 5 MW production machine.	14
Figure 2	Photograph of the new low temperature ribbon heater element.	15
Figure 3	Mechanical schematic of the experimental housing for the ribbon heaters.	16
Figure 4	Temperature profile at the two extreme shapes possible with the housing shown in the previous figure.	16
Figure 5	Ribbon-type heaters installed in the production machine.	18
Figure 6	Ribbon heater assembly detail.	18
Figure 7	Polar radiation pattern from heated surfaces.	19
Figure 8	Infrared sensor installed on production machine.	21
Figure 9	Copy of blueprint showing installed temperature sensor.	22
Figure10	Layout of the new cathode test system being designed for installation in the pilot amorphous Si machine showing the two new rolling thermocouple assemblies.	24
Figure 11	Schematic of the benchtop backreflector ZnO film thickness measurement system.	27
Figure 12	Schematic of the benchtop backreflector scatterometer.	27
Figure 13	Diffuse reflection comparison of various samples.	29
Figure 14	Plot of correlation coefficients for each cell parameter calculated at single scattering angles (17 R&D samples).	31
Figure 15	Plot of correlation coefficients for each cell parameter calculated at single scattering angles (12 5BR production samples).	31
Figure 16	Schematic of the modified scatterometer configuration.	32
Figure 17	Comparison of light scatter for 5BR 531 using 2 different angles of incidence. "Angle" is with respect to the specularly reflected beam.	32
Figure 18	Electrical schematic of the PVCD.	34
Figure 19	Light (laser) and voltage waveforms from the PVCD.	35
Figure 20	Photograph of the PVCD bench-test system. The oscilloscope is displaying the waveforms of the laser pulse (the step function) and the output of the PVCD. Notice the similarity between the stored traces on the oscilloscope and the waveforms in Figure 18.	36
Figure 21	Oscilloscope traces of a PV cell using both the bench-top PVCD (upper trace) and a probe in direct contact with the ITO. (10 ms/div). The laser is pulsed on after 10 ms, and switched of after 20 ms.	37
Figure 22	Measurement of PVCD time constant. A simple single pole filter with a time constant of 1.3686, fits the data over 3 seconds with less than a 0.01% relative error.	37
Figure 23	Oscilloscope traces of the laser diode module current monitor (top) and output of a photodetector (bottom). The oscilloscope recorded the peak voltages for each of these signals.	38
Figure 24	PVCD waveforms and fitted curves resulting from a 4-parameter fit.	39
Figure 25	Parameter resulting from fit of PVCD waveform plotted vs. measured open circuit voltage for cell with a different number of layers.	39
Figure 26	Mechanical schematic showing the mounting of the PVCD in the take-up chamber of the 5 MW.	41
Figure 27	United Solar's roll-to-roll backreflector machine. This machine is also part of United Solar's decommissioned 2 MW plant and will be used for the bulk of Task 2, and for part of Task 1.	44

List of Figures (continued)

Page

Figure 28 Dependence of Jsc for a-SiGe:H cells on oxygen flow. 46
Figure 29 Variation of Ge content and deposition rate across cathode. 51
Figure 30 Double-junction roll-to-roll plasma-CVD processor, previously used as United Solar's production machine. This machine will be used as an experimental machine for much of the work proposed in Tasks 1 and 3. 52
Figure 31 Single chamber system used for cathode development. 53
Figure 32 a-Si:H single-junction cell structure. 53
Figure 33 Thickness profiles for films made at different applied rf powers. 55
Figure 34 Orientation of film thickness measurements. 55
Figure 35 Variation of deposition uniformity over length of cathode as a function of deposition rate. 56
Figure 36 Uniformity across width of web (cathode) from deposits made using different gas flows from outside cathode and gas manifold hardware. 57
Figure 37 Deposition rate profiles across new cathode at different deposition rates. 58
Figure 38 Plot of fill factor versus short circuit current for cells made using the new and 5MW style cathodes. 59
Figure 39 Plot of efficiency versus short circuit current for cells made using the new and 5MW style cathodes. 59
Figure 40 (a-f) Electron Impact Cross Sections (cm^2):
a. H_2 momentum transfer; 66
b. Lowest threshold H optical excitation; 67
c. SiH_4 optical excitation; 68
d. H_2 ionization; 69
e. lowest threshold H_2 vibrational excitation; 70
f. lowest threshold SiH_4 vibrational excitation; 71
g. dissociative attachment from the v=1 and v=2 vibrational states of H_2. 72
Figure 41 Modeled RF Reactor Subchamber Design. 73
Figure 42 (a-d) Electron Energy Distribution Functions at Various Times after Turn-on:
a. $1.75x10^{-8}$ s; 75
b. $1.34x10^{-6}$ s; 76
c. $9.77x10^{-5}$ s; 77
d. $9.90x10^{-3}$ s. 78
Figure 43 (a-e) Evolution of Neutral Species (cm^{-3}):
a. H_2, SiH_4, H, SiH_3, Si_2H_6: 79
b. H_2, H_2(v=1), H_2(v=2); 80
c. Si_2H_5, SiH_2, SiH, Si; 81
d. Si_2H_4, Si_2H_2, Si_2H, Si_2; 82
e. Si_2H_3, Si_3H_8, Si_3H_5, Si_3H_4. 83
Figure 44 (a-c) Evolution of Positive Ions (cm^{-3}):
a. SiH_3^+, SiH_2^+, SiH^+, $Si_2H_7^+$, $Si_2H_5^+$; 84
b. $Si_2H_4^+$, $Si_2H_3^+$, $Si_2H_2^+$, Si_2H^+, $Si_3H_7^+$; 85
c. $Si_3H_6^+$, $Si_3H_5^+$, $Si_3H_4^+$, H_3^+, H_2^+, H^+. 86
Figure 45 Evolution of Negative Ions (cm^{-3}) : H^-, SiH_3^-, $Si_2H_5^-$, $Si_3H_7^-$. 87
Figure 46 Evolution of Positive and Negative Ions and Electrons (cm^{-3}): total positive ions, total negative ions, electrons. 89
Figure 47 Evolution of Average Electron Energy (ev). 90
Figure 48 Measured Thickness of Amorphous Silicon Deposition (nm) in Reactor. 91

List of Tables

		Page
Table 1	Ribbon Heater Engineering Details.	17
Table 2	Influence of Various Stray Objects.	20
Table 3	Correlation Coefficients for 5BR# 534 Samples.	30
Table 4	Measured Reflection Minima for 15 R&D Backreflector Samples.	33
Table 5	Comparison of Data for a-Si:H Cells Co-Deposited on Al/ZnO Backreflectors. Cell Measurements Completed Using AM1.5 Light.	42
Table 6	Data for Cells Prepared Using the Different Backreflectors after Different Exposure Environments and Exposure Times.	45
Table 7	Data for a-SiGe:H Cells Prepared with Backreflectors Made Using Reactive Sputtering Technique Under a Variety of Deposition Conditions.	47
Table 8	Data for a-SiGe:H Cells Whose Backreflectors were Made Using Targets With Different Al Contents.	47
Table 9	Data for a-SiGe:H Cells Whose Backreflectors were Made with the Reactive Sputtering Process Using Zn Metal Targets and the Standard Process Using ZnO Targets.	48
Table 10	Data for 44.5 cm^2 Modules Made With Different Backreflectors.	48
Table 11	Data for a-SiGe:H Cells Made at Different Applied Powers but Similar i-layer Deposition Rates.	56
Table 12	Data for a-SiGe:H Cells Made Using the New and the 5 MW Style Cathodes.	59

BACKGROUND

Overview of ECD/United Solar's PV Manufacturing Technology

Key features of ECD/United Solar's photovoltaic manufacturing technology are summarized below.

Spectrum Splitting, Triple-Junction Cell Design
High conversion efficiencies are obtained by using a triple-junction triple-bandgap cell that has high-quality bandgap profiled a-SiGe alloy for the middle and bottom intrinsic layers. The cell structure is shown in Figure A.

Grid	Pattern
Transparent Conductive Oxide	
p-type microcrystalline Si alloy	
i-type a-Si:H alloy	
n-type a-Si:H alloy	
p-type microcrystalline Si alloy	
i-type a-SiGe:H alloy	
n-type a-Si:H alloy	
p-type microcrystalline Si alloy	
i-type a-SiGe:H alloy	
n-type a-Si:H alloy	
Textured Back Reflector Ag/ZnO	
Stainless Steel Substrate	

Figure A. Structure of a triple-junction spectrum-splitting solar cell produced in the ECD/United Solar continuous roll-to-roll manufacturing process.

United Solar has recently demonstrated 14.6% initial and 13% stable, small-area energy conversion efficiency a-Si alloy solar cell devices with an a-Si//a-SiGe//a-SiGe triple-junction design. United Solar has also demonstrated stable 10.2% efficiency for a 1 ft^2 panel using this triple junction solar cell design.

Low-cost, large-scale continuous roll-to-roll operation
The nine layers of a-Si alloy material used in the solar cell are deposited sequentially in a single pass onto a 2500 ft. long substrate in a roll-to-roll process, as is shown in Figure B. This stable steady-state process has proven to be reliable and capable of producing cells with a high degree of uniformity. The operating cost, which includes materials, maintenance and labor, is low.

Flexible thin stainless steel substrate
The substrate, a 5 mil thick, 14 in. wide, 2500 ft long stainless steel roll has many advantages over glass substrates: (1) it is lightweight, flexible, and will not shatter or be damaged during manufacture, handling, and subsequent operation in the field; (2) the thin stainless steel substrate has a thermal time constant of less than 10 ms and, consequently, can be quickly heated and cooled, thus eliminating any waiting time for temperature stabilization; and (3) the substrate transport mechanism in the deposition chambers is simple and reliable with negligible component wear, resulting in very low machine maintenance costs.

Lightweight polymer encapsulated PV module
EVA and Tefzel are used for module encapsulation. These modules are flexible, lightweight, and shatterproof.

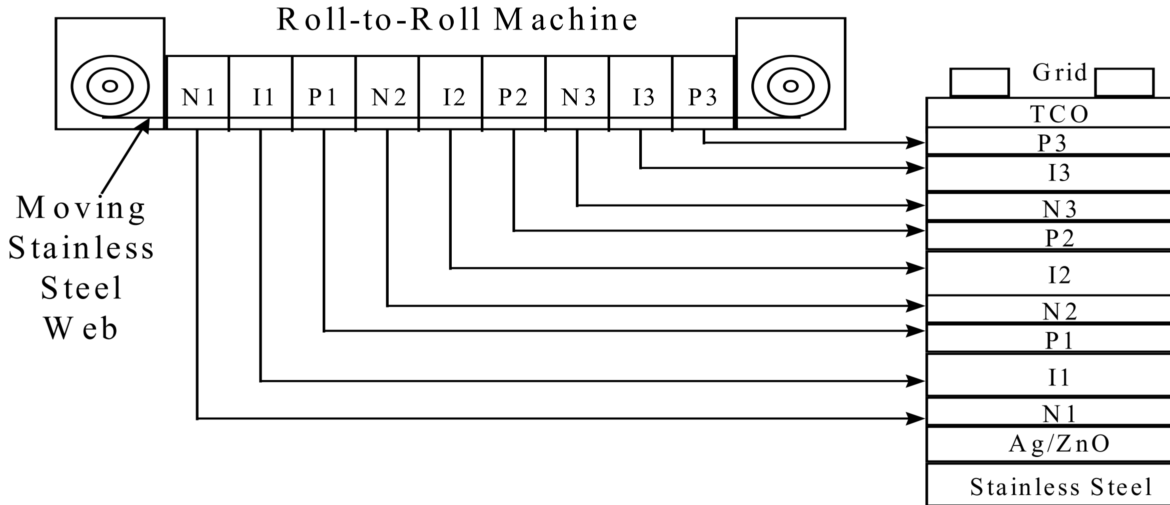

Figure B. Schematic drawing of ECD's roll-to-roll solar cell deposition process.

Current Manufacturing Procedures

The present manufacturing plant in Troy, Michigan at United Solar, ECD's manufacturing joint venture with Canon Inc., produces amorphous silicon alloy based solar cells and photovoltaic modules with a triple-junction, triple-bandgap configuration. ECD/United Solar's proprietary roll-to-roll continuous substrate process is employed to produce complete solar cell structures on stainless steel rolls. These rolls, typically 2500 ft. long, 14 in. wide, and 5 mil thick, are processed at 2 ft. per minute.

The stainless steel rolls are coated consecutively, in roll-to-roll deposition machines, with a back reflector consisting of a metal and metal oxide layer, nine layers of amorphous silicon alloy, and a transparent conducting oxide top contact layer. The rolls are then cut into appropriate sizes for assembly into photovoltaic modules.

ECD/United Solar's proprietary solar cell manufacturing process is divided into two distinct sequences: (1) roll-to-roll solar cell deposition (front-end), and (2) module assembly (back-end). The ability to divide manufacturing into these two sequences which can be located in quite different locations, is a unique advantage of our process. The output of the front end feeds the semi-automated back-end assembly lines in place for producing 17 different products: 7 types of framed rigid modules; 3 types of flexible modules; 2 types of folding modules and 5 types of building integrated roofing modules.

Specifically, our current solar cell production involves the following process steps and equipment:

I. Current Front-End Roll-to-Roll Deposition Plant for Solar Cell Production

<u>I.1 Substrate Washing Machine</u>
The stainless steel roll, purchased from a supplier, is first washed to produce clean, dry, particle-free substrate material suitable for a-Si alloy deposition. The washing machine is a continuous roll-to-roll processing system which transports the stainless steel web though a detergent cleaning station, multiple de-ionized water rinsing baths, and an infrared drying oven.

I.2 Back-Reflector Machine

The roll is then transferred to the back-reflector (BR) machine, also a continuous roll-to-roll processing system. The BR machine sequentially deposits a reflective metal alloy layer and a metal oxide "buffer" layer onto the cleaned stainless steel web by magnetron sputtering. The proprietary metal alloy and metal oxide buffer layers provide ohmic contact to the solar cell and an improved infrared response. The metal alloy layer adheres to the stainless steel and texturizes the surface to provide a diffuse optically-reflective layer. This texturing enhances absorption of the infrared portion of the solar spectrum by providing an increased optical length for reflected light in the thin film solar cell structure.

I.3 Amorphous Silicon Alloy Deposition Machine

After the back-reflector deposition, the roll is loaded into the amorphous silicon alloy deposition machine. This machine is a continuous roll-to-roll rf plasma-enhanced CVD processing system which sequentially deposits, in a single pass, nine thin films of doped and undoped amorphous silicon alloy semiconductors.

Mixtures of feedstock gases are decomposed at a pressure of approximately 1 Torr in a series of rf PECVD plasma chambers to continuously deposit amorphous thin film layers onto the substrate which is heated to approximately 250°C. The multi-section amorphous silicon alloy deposition machine consists of a pay-off chamber section, nine process chamber sections for deposition of the triple (graded) junction, triple bandgap solar cells, and a take-up section. The process gas mixture in each deposition chamber is dynamically isolated from adjacent chambers by proprietary "gas gates" that isolate the gas mixtures in adjacent chambers even though no actual physical impediment is present.

The substrate transport system, which controls the web speed, tension, and steering accurately positions the substrate in the various process chambers and ensures that the substrate is properly wound. The deposition takes place on the underside of the substrate, thus minimizing film defects due to particulates.

I.4 Transparent Conducting Oxide (TCO) Deposition Machine

The substrate roll, now coated with back reflector and semiconductor layers, is finally transferred to another continuous roll-to-roll machine which deposits a transparent electrically-conducting oxide (TCO) layer on top of the solar cell structure. The substrate is heated to approximately 200°C and the film is deposited by reactive sputtering of an indium-tin alloy in an oxygen atmosphere. The TCO layer has two functions: first, it provides an electrical top contact between the current-generating photovoltaic layers and the current collection grid; second, its thickness is chosen so that it acts as an anti-reflective coating for the amorphous silicon alloy, thus increasing the utilization of incident light.

II Current Semi-Automated Back-End Module Assembly Plant

II.I Slabbing

A finished roll of TCO coated a-Si alloy solar cell material is cut by a semi-automatic press into 35.2 cm x 35.6 cm "slabs". The press also punches various geometric shapes at the edges of the slabs to facilitate later interconnect attachments.

II.2 QA/QC

The die press also cuts 10.2 cm x 35.6 cm samples at preset intervals throughout the deposition roll. These samples are processed into test solar cells for QC qualification. In this manner, the entire deposited roll of solar cell material is characterized.

II.3 TCO Scribing

The slabs are then processed through an automated machine that etches the ITO from the borders of the cells; the cell size is electronically selectable.

II.4 Short Passivation

Defects in the solar cell that could give rise to electrical shorts on the coated web are electrically isolated by electrolytically converting the transparent top conductor into an insulator at the defect sites through a proprietary process. This automatic short passivation operation involves treating the web with electrolyte solution and subjecting the cell to reverse electrical bias. After short passivation, the residual electrolyte is rinsed off with de-ionized water, and the web is dried with hot air. This process is also performed by an automated machine.

II.5 Screen Print Grid Pattern

Another automated machine is used to apply the collection grid wires to the cells, and then coat the cells with a clear lacquer.

II.6 Final Assembly

The final assembly process includes the following steps:

- Cell Interconnect - Cells are interconnected to make the cell block assembly. Suitable fixtures are provided to ease the assembly process.
- Laminating - The finished cell block is laminated in a vacuum laminator. Tefzel and EVA are used for the front cover.
- Module Finishing - The laminated cell block is trimmed to size and a junction box is attached. Other framing and connector details are added for specific products.
- Testing and Packaging - The module is finally tested in a solar simulator which measures the I-V curve of the finished modules under simulated AM 1.5 conditions and provides a printout of the I-V characteristics. Modules are then packaged, ready for shipment.

Advantages of the Present Manufacturing Process

The ECD/United Solar a-Si alloy based thin film PV cell design and manufacturing technology offers several fundamental advantages:

1. Low semiconductor material cost; the device thickness is < 1 µm,
2. Low-process cost; the continuous roll-to-roll process offers significant economies of scale as the process is scaled up,
3. Thin stainless steel substrate; the ECD/United Solar PV modules are lightweight, rugged, and flexible. This reduces the installed cost of PV systems. In addition, there is a significant cost advantage in handling and processing the flexible stainless steel substrate, as compared with other substrates,
4. The modules are composed entirely of environmentally safe materials.

Problems with the Present Manufacturing Process

During the start-up and optimization of the new United Solar 5 MW plant, which was designed and constructed by ECD, a number of manufacturing processing and hardware problems that limit stable module efficiency, yield, and throughput have been identified. With the expanded back-end facilities, including the addition of automated processing equipment, improvements in the throughput of the new front-end equipment will provide substantial economy of scale module cost reductions. In addition the stable efficiency of the PV modules, which are currently being manufactured at United Solar, is approximately 30% lower than that which can be expected from data obtained in the batch processes. The purpose of this program is to solve and implement solutions for the key problems that are limiting the module throughput of the 5 MW plant and the conversion efficiency of the modules. Below we review the major factors that are limiting the throughput of the equipment and the stable conversion efficiency of the modules.

1. Breakage of the quartz IR lamps that are used in the deposition machines to heat the substrate leads to considerable downtime, and expense. The IR lamp's quartz envelope becomes coated over time by stray depositing species diffusing out of the reaction zones. This coating absorbs the lamp's IR radiation and thermally stresses the glass envelope, which cracks after time.

2. The process consistency of the machine can be further improved. Typically, the efficiency of solar cells produced on a 2500 ft. long stainless steel roll substrate varies by as much as 10% within one roll. This problem, and uncontrolled run-to-run variations in material quality, also make it extremely difficult to adiabatically fine tune to processes to maximize the cell efficiency. Furthermore, data from QA/QC analysis is available until after final deposition of the TCO onto the roll of solar cells and the roll is slabbed. This delay in feedback limits the effectiveness of ongoing optimization and may result in large yield losses when a machine malfunctions. These shortcomings can be traced to the lack of on-line sensing devices which can monitor the quality of the material produced in the machines and correlate these data with other processing variables and the results of QA/QC measurements.

3. The performance of the back-reflector material produced in the 5 MW line at production line speed results in PV cell efficiency that is approximately 10% lower than that which can be obtained with thicker back-reflector produced at slower line speeds. We have made engineering compromises to sacrifice material quality in order to maintain the required line speed. The present processing speed is limited by the sputtering of zinc-oxide; this processing step is also dominates the front-end material costs of the PV material.

4. Another reason for lower stable efficiency results from the fact that the materials produced in large-scale machines, including this 5 MW manufacturing line have significantly lower quality than the intrinsic materials produced in small-scale R&D machines.

Task 1 - Process Control Improvements: New Substrate Heating and Temperature Monitoring Systems

The New Substrate Heating System

Introduction

A new heating system has been designed and tested. The lifetime of the heater elements used in this new system is at least an order of magnitude higher than the lifetime of the heaters used in the previous system. This new system will eliminate the cost of replacement heaters, unscheduled downtime due to heater breakage, and scheduled downtime for replacing heaters.

The new substrate heating system was of high priority due to the unreliability of the present quartz IR heaters installed when the new 5 MW production machine was built. The quartz IR heaters needed replacement at about an 8 – 10 week interval. The hardware cost alone for this replacement is on the order of 10 k$ per set. Also, there were substantial additional costs associated with the downtime needed to change the lamps and lamp breakage leading to unscheduled downtime towards the end of the lamp lifetime. Consequently it was decided to accelerate this program as much as possible. A prototype heater, using the new lower temperature metal ribbon heaters was assembled and installed initially in the pilot machine and then in the production machine where we could immediately obtain reliability data in a production environment. The heater was installed in the I-1 chamber where the quartz IR heaters had the shortest lifetime. The system was monitored to determine if this new design would be more reliable than the quartz IR heaters, and to determine what design changes would be needed to increase their reliability.

System Design

Quartz IR lamp heaters have been used in our production machine to maintain the substrate temperature. As shown in Figure 1, these lamps, because they run hot, accumulate thermally decomposed material on the envelope of the lamp.

Figure 1. Photograph of a quartz IR heating lamp from the 5 MW production machine.

The accumulation of material, in combination with the unavoidable temperature cycles, eventually results in severe flaking and in physical stresses large enough to break the quartz envelopes. Even though the deposition takes place on the underside of the substrate, the growing film is not protected from physical damage from the flakes and from the glass debris. Breakage of the quartz IR lamps that are used in the deposition machines to heat the substrate further leads to considerable downtime, and expense.

We proposed to replace the quartz heaters in the roll-to-roll deposition machine with low-temperature, long-lasting NiChrome (a Nickel Chrome alloy) resistance heaters. These heaters operate at lower, more stable, temperatures. More importantly, they were thought to require little, if any, maintenance. They further offer considerable freedom in their design. We proposed to design, prototype, test, and retrofit the deposition machines with a new substrate heating system using flat ribbon-shaped elements held in place over the web with ceramic insulators, in a basic “flat sheet” configuration shown in Figure 2.

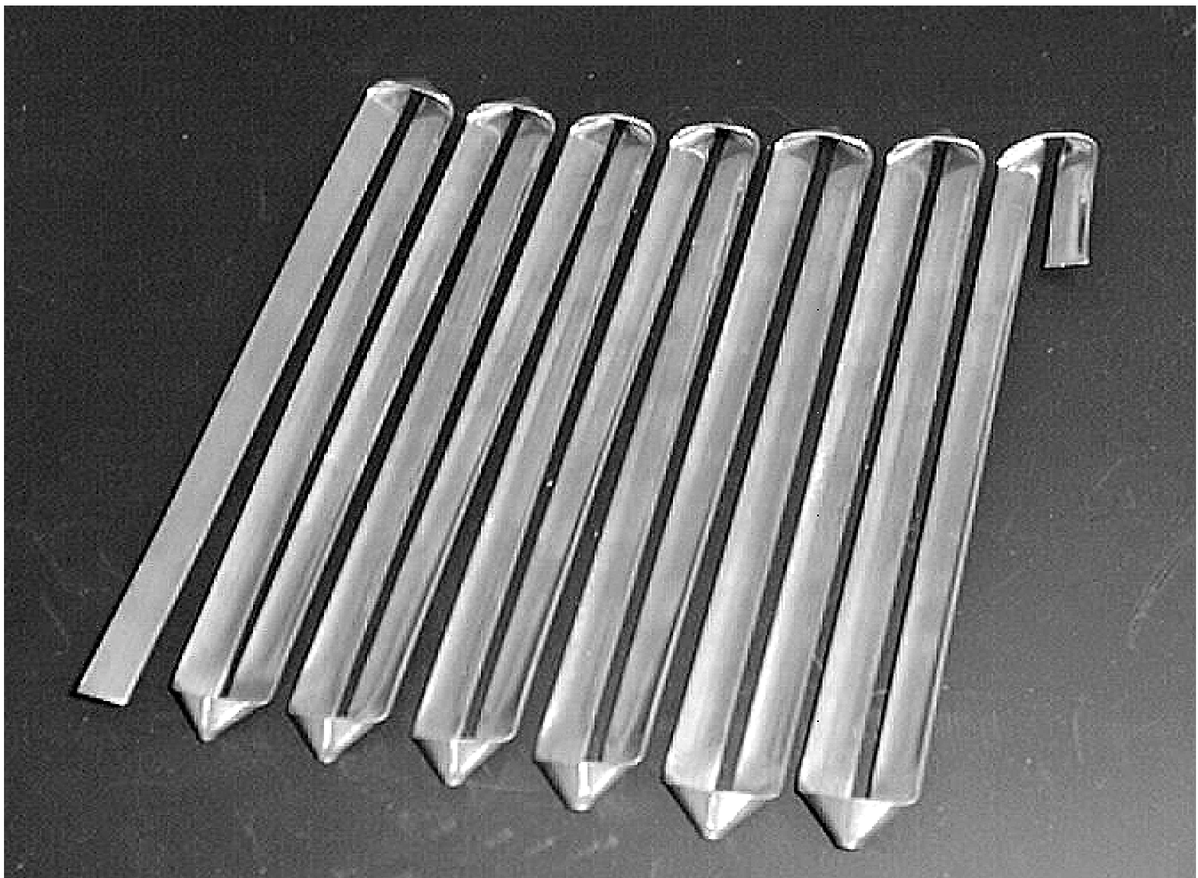

Figure 2. Photograph of the new low temperature ribbon heater element.

Work Performed

Ribbon heaters were initially installed in the pilot machine, using a housing that allowed the shape of the “flat sheet” to be adjusted to a large degree (see Figure 3).

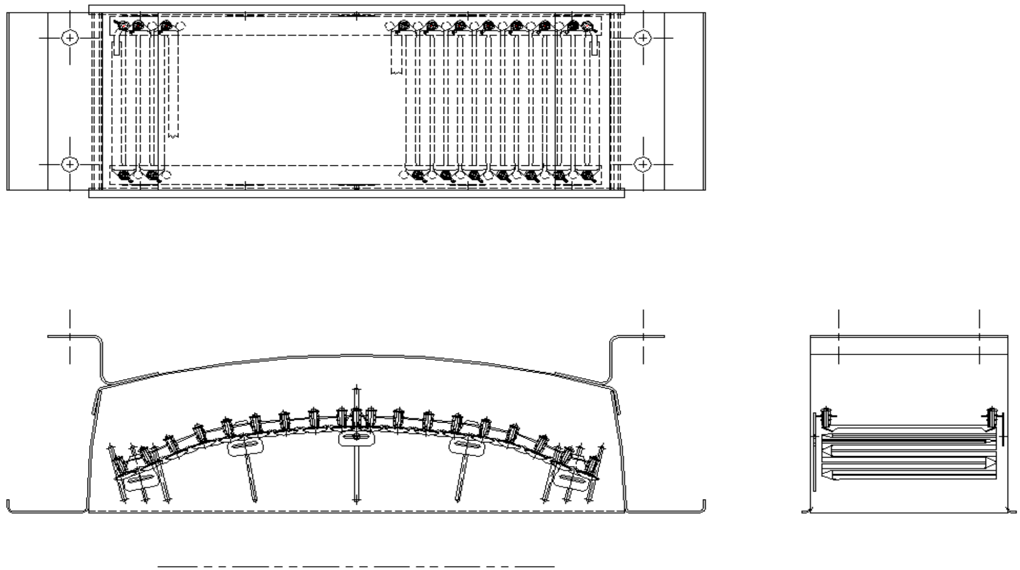

Figure 3. Mechanical schematic of the experimental housing for the ribbon heaters.

The idea behind the adjustment is to be able to compensate for the generally higher temperatures the centerline of the web experiences with uniform heating. However, the temperature profile was found to be very insensitive to changes in the shape of the heating surface (see Figure 4) and very similar in nature to the profile obtained with the infrared lamps.

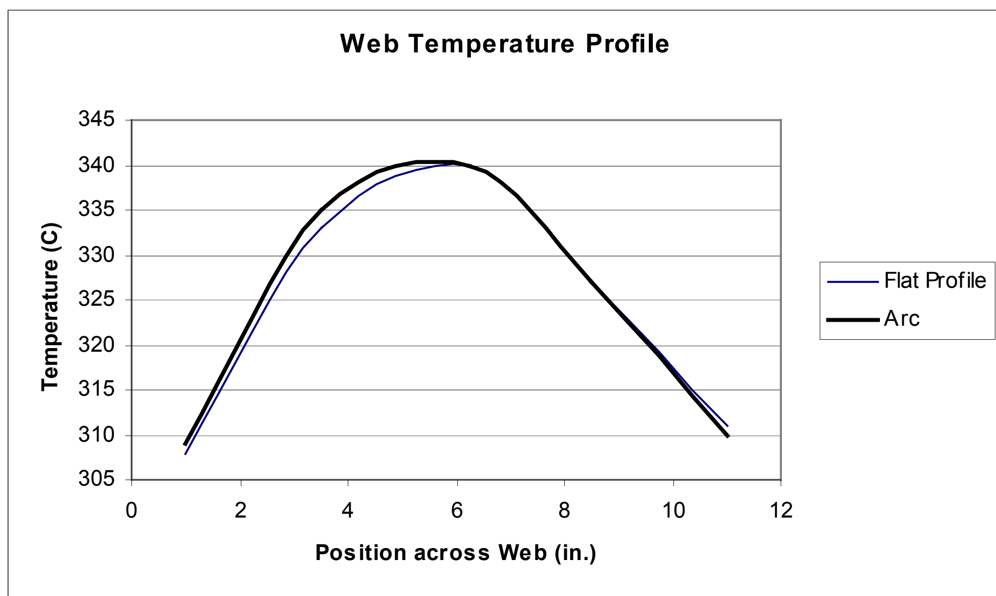

Figure 4. Temperature profile at the two extreme shapes possible with the housing shown in the previous figure.

It soon became evident that the reliability of the ribbon heaters was vastly superior to that of the infrared lamps. So we decided, well ahead of schedule, to construct and install ribbon-type heaters in a portion of the production machine. The engineering details are listed in Table 1, while Figures 5 and 6 show their installation.

As of June 25, 1999, the ribbon heaters have been tested in many production runs without any failure nor any sign of degradation. In contrast, the old style infrared lamps would have had to be replaced at least two times for a similar production quantity, at a total material cost of at least $20,000.

Summary Evaluation: Improved Substrate Heaters

The improved substrate heaters have been installed in a portion of the roll-to-roll amorphous silicon production machine. They have operated without failure for over 100 production runs, without requiring maintenance other than visual inspection. The cost savings we anticipated in our proposal have been achieved well ahead of schedule. We are currently working on improving the temperature uniformity across the web.

Table 1. Ribbon Heater Engineering Details.

Electrical Design

Description	Value	Unit
Width	0.375	Inches
Thickness	0.0285	Inches
Primary Voltage	480	V
Design Voltage	80	V
Connection Type	Single	
Voltage per phase	80	V
Power per phase	2.128	kW
Current	26.6	A
Cold Resistance	2.8643	Ohm
Material	"A"	
Resistivity	510	Ohm/sq. mil
Unit Resistance	0.04772	Ohm/ft
Wire Core Temp.	900	F (Max)
Resistivity Change	1.05	x
Power Density	3.66	W/sq.in
Length	60.02	ft/phase
Unit Weight	0.039	lb/ft
Length/lb	25.66	ft/lb
Total Weight /EL.	2.34	lb/ft
Elements/phase	1	
Phases	1	
Total Power	2.13	kW/circuit
Total Ribbon	60.02	ft
Total Weight /EL.	2.34	lb

Mechanical Design

Description	Value	Unit
Elements per phase	2	
Rows per element	2	
Spacing	0.125	in
Pitch	0.5	in
Number of Strands	72	
Loops / element	18	
Wire per strand	10	in
Straight Length	9.75	in
Overall Loop Height	9.75	in
Wire per element	60.02	ft
Loop Centers	1	in
O.A. length cc loops	17	in
O.A. Length	17 7/8	in

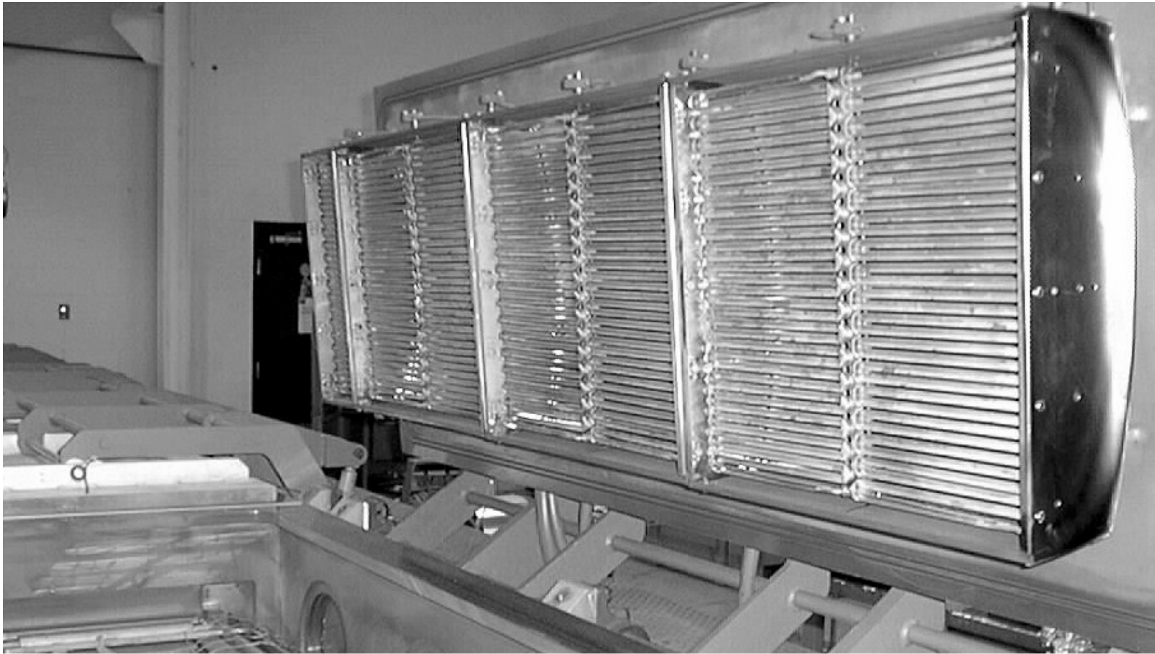

Figure 5. Ribbon-type heaters installed in the production machine.

Figure 6. Ribbon heater assembly detail.

New Temperature Monitoring Systems

Introduction

Accurate temperature sensing is essential in all of the deposition machines. The present sensor system used in our production machines are thermocouples which are placed in close proximity of the back side of the substrate. The accuracy of the temperature measurement is based upon conductive heat transfer from the web to the thermocouple. As a result, while the temperature sensor system in the amorphous silicon machine is accurate due to higher conductive heat transfer in the machine, the present sensors in the backreflector (BR) and top conductive oxide (TCO) sputtering machines are not. The combination of an order of magnitude less conductive gas (Ar vs. H) and three orders of magnitude lower pressure, all but eliminate the thermal coupling between the web and the thermocouples in the BR and TCO machines. To solve this problem we are testing two new temperature monitoring systems: an IR temperature sensor system, and a rolling thermocouple design.

IR Temperature Sensor

The remote temperature sensor, based on the analysis of the blackbody radiation emitted by the heated stainless steel web, must have the following features:

- It should operate in a wavelength range at which the glass windows used on the vacuum vessels at the production machines are transparent. This constrains the wavelength range to less than 1.8um, approximately.
- Because the radiation emitted at those wavelengths, at the typical temperatures of interest, is small, efficient radiation detectors, operating near the room-temperature thermal detection limit are required. This constrains the detector types to Silicon-based semiconductor detectors, or to S1-type phototubes, both of which further limit the possible wavelength range to near 1um.
- The sensor must further be capable of detecting the radiation from a specular surface, which reduces the already-low emissivity of stainless steel.
- Objects with specular surfaces radiate blackbody energy at angles that differ from that emitted by diffuse objects; the detector must therefore be configured to detect from specific angles. Figure 7 compares the blackbody emission from a diffuse surface ("A", on the left) with that of a specular one ("B", on the right):

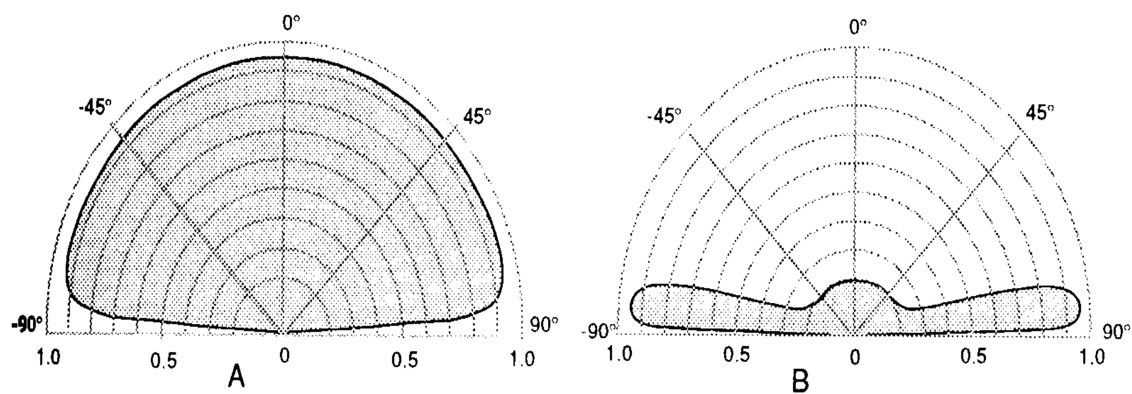

Figure 7. Polar radiation pattern from heated surfaces.

As a result, the infrared blackbody radiation from a heated stainless steel web has initially been found to be rather weak and difficult to detect. The infrared sensor we used is built around a Model M77LS infrared detector, manufactured by Mikron Instruments Company. Although adequate for the detection of the blackbody radiation from ordinary objects at elevated temperatures, it did not have, as received, sufficient sensitivity to detect the

signal from specular objects such as polished stainless steel, which forms the substrate onto which the solar cells we produce are deposited. Only after positioning to detect radiation from a grazing angle was a signal detected.

Bench top measurements revealed:

- When comparing the temperature deduced from the infrared emission of polished stainless steel with that from a piece of black, diffuse, graphite, both heated to 200C, differences in excess of 50C were observed.
- The temperature deduced from the infrared emission depends strongly on observation angle. Variations in observation angles of +/-5 degrees introduce errors of the order of +/-40 C.
- Because the reflectivity of any specular surface unavoidably approaches 100% as the observation angle nears grazing incidence, the reflected images of stray objects come into any infrared sensor's field of view. If the temperature of that stray object varies, its parasitic radiation affects the deduced temperature of the section of web of interest. Table 2 summarizes the errors introduced by various stray objects.

Table 2. Influence of Various Stray Objects.

Stray Object	**ΔT(Stray object) (C)**	**ΔT (Deduced) (C)**
Diffuse graphite	20	5
Stainless steel oblique to optical Path	20	2
Stainless steel normal to optical Path	20	1

Consequently, an infrared-based remote sensor must be used with the following constraints:

- The observation angle must be large and constant. In our production machines, the web is held up and flat over the deposition areas with magnetic rollers. In between these rollers, the web can warp in a random fashion, and present randomly varying angles to the sensor. Thus, only observation areas near magnetic rollers are usable.
- The deduced temperature depends upon the emissivity of the web's surface, which depends upon the nature and diffusivity of its coating. If the diffusivity of the coating depends upon the deposition temperature, as it does for the backreflector layers we produce, then a temperature feedback loop based upon this technique can "run-away."
- The remote sensor must be calibrated for each step in a multilayer process.
- Care must be applied in designing the optical path.

The sensor was installed in the roll-to-roll rf plasma-enhanced CVD processing system, which operates at a pressure of approximately 1 Torr; this machine was selected instead of the backreflector machine because of its higher operating pressure that will allow for a more accurate calibration. Figure 8 shows the installed sensor.

Description of IR Temperature Sensors

The infrared sensor is built around a Model M77LS infrared detector, manufactured by Mikron Instruments Company. The unit's internal gain was increased to compensate for the lower emissivity of specular stainless steel. It is configured to detect the blackbody radiation emitted at grazing angles. Thanks to its operating

wavelength in the near infrared spectral region, it views the web through a standard quartz vacuum window, and therefore does not operate in the hostile environment inside the deposition chambers.

To minimize the influence of stray objects on the temperature measurements, a piece of specular stainless steel is placed in the reflected field of view of the infrared detector.

At present, the sensor, as shown in Figure 9, views the bottom side of the web, the side that is not illuminated by the heaters.

Figure 8. Infrared sensor installed on production machine.

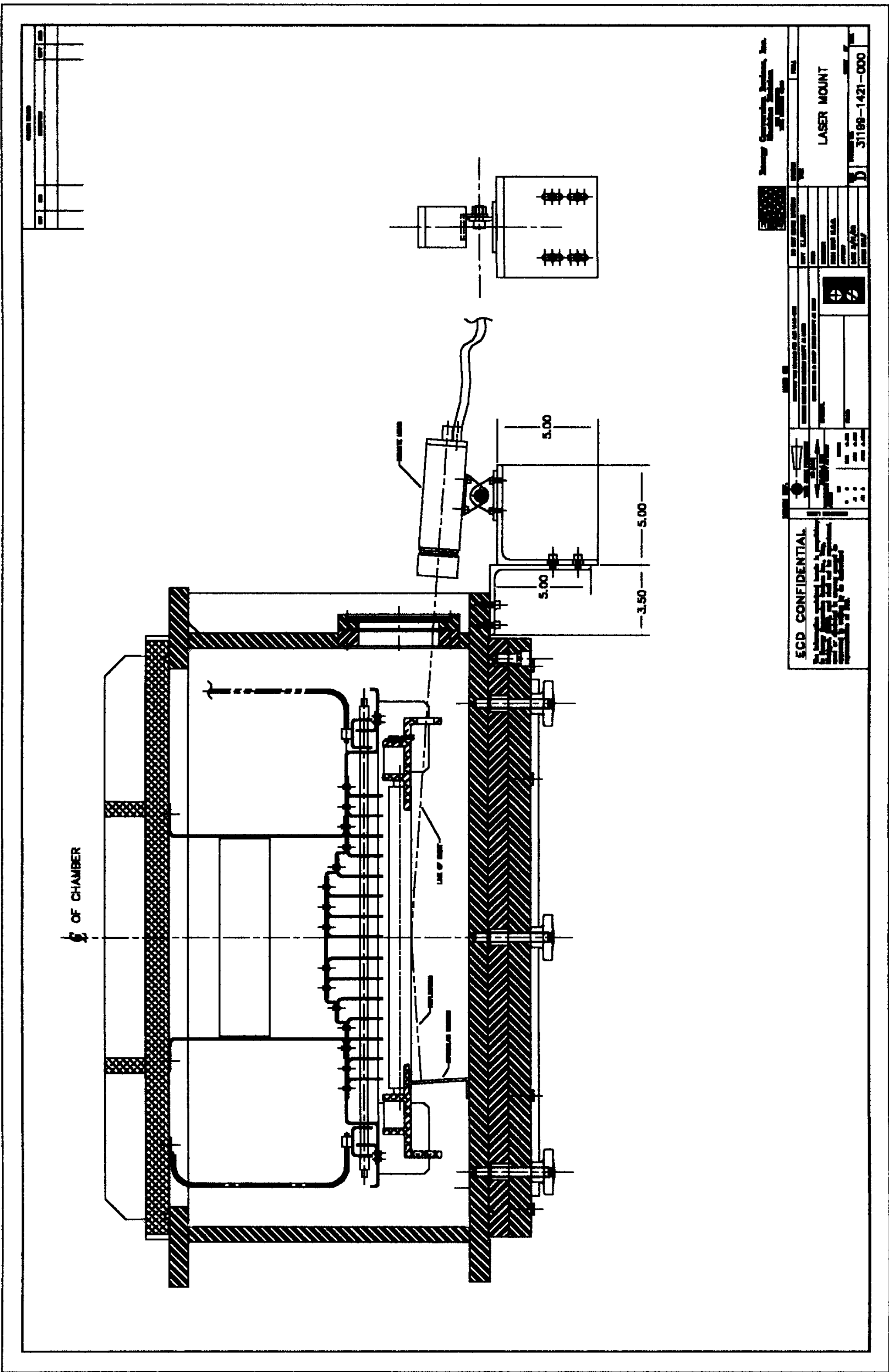

Figure 9. Copy of blueprint showing installed temperature sensor.

Rolling Thermocouple Concept

The rolling thermocouple concept is quite simple: the thermal time constant of the 5 mil thick stainless steel substrate is very short – about 10 ms. Consequently, as soon as the web makes contact with one of the magnetic rollers, the web assumes the temperature of the roller. Therefore, in principle, one can measure the temperature of the web just after any of the magnetic rollers by measuring the magnetic roller temperature. To do so we have designed a rolling thermocouple system that has the following features:

- A thermocouple is mounted inside of roller that makes contact with the magnetic roller. In this way we obtain a strong thermal coupling without need to directly contact the web, which leads to scratching.
- The thermocouple roller spans the full width of the web. Consequently, if this roller affects the temperature of the roller, it will affect the temperature uniformly across the width of the web so that the temperature control circuits can compensate for its effect.
- The thermocouple is mounted inside of a non-rolling tube mounted inside the roller to prevent the thermocouple from hanging up on a moving surface.
- The bearings have been designed so that as the roller heats up, it expands in a way to prevent binding of the bearings.
- Two types have been designed and are being built – one is built of magnetic materials to increase contact with the magnetic roller, and the other of non-magnetic materials

The low thermal coupling of the present thermocouple system to the web, which prevents accurate measurement of the web temperature, is still present in this new system. However, this low coupling should lead to long thermal time constant rather than inaccurate measurement of the web temperature.

This new system has been designed into the new cathode assembly that is being engineered for the amorphous silicon pilot machine and will be tested in about 1 month. These rollers are depicted in Figure 10.

This new system will be compared against the present system which works well in the pressure/gas regimes used in the amorphous silicon machine. We shall measure both the system accuracy and time constant and extrapolate the time constant for operation in the TCO and BR machines where the gas has a much lower conductivity.

Testing the New Temperature Monitoring Systems

While we believe that the two new systems being developed will be effective in the TCO and BR machines, testing them becomes an interesting problem since we do not have an accurate system to compare them with. The solution we have devised is to test them in the amorphous silicon machine where we have accurate temperature monitoring systems. The IR sensor will be tested using existing windows in the 5 MW production machine, where we have the most accurate temperature monitoring system. Since this sensor is completely external to the machine, it will not affect operations. The rolling thermocouple, however, would require modifications of internal components in the production machine; consequently, it is being tested in the pilot amorphous silicon deposition machine where we are testing the new cathode designs, thus eliminating any risk to production.

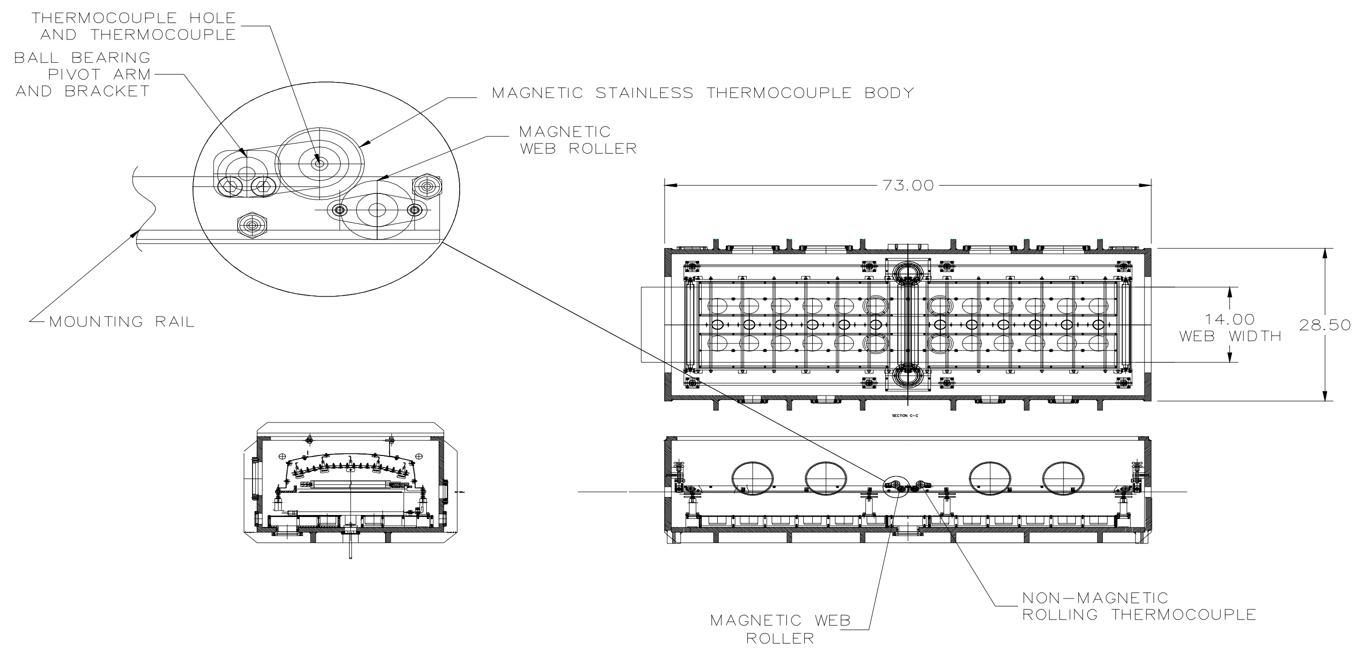

Figure 10. Layout of the new cathode test system being designed for installation in the pilot amorphous Si machine showing two new rolling thermocouple assemblies.

Task 2 - Process Control Improvements: Development of In-Line Sensors and Diagnostic Systems

Introduction

United Solar manufactures its PV material using 2500 ft. long substrates that are processed sequentially through a series of roll-to-roll deposition machines: the backreflector (BR), amorphous silicon (a-Si), and top conductive oxide (TCO) machines. The QA/QC process takes place after deposition in final roll-to-roll machine, after the long substrate has been slabbed. This is a highly efficient manufacturing process, but can be improved with in-line diagnostic systems:

1. In-line diagnostics will immediately notify operators of any significant problems, consequently reducing the probability that equipment malfunctions or operator errors go unrecognized until the later QA/QC process.
2. The feedback rate for continual optimizing the machines using incremental variations in the standard processing conditions the feedback rate could potentially be reduced by several orders of magnitude to less than 1/hr from the present 1/few days.
3. The operators would be able to identify and track fluctuations in process parameters that lead to variations in the quality of cells produced, consequently increasing the material quality.

We already have highly-instrumented and automated production machines with hardware and software feedback systems. These machines, however, are operated open-loop in that sensors monitor process parameters (e.g. temperature, rf power, pressure, etc.) rather than characteristics of the deposited coatings (e.g. Voc, efficiency, Jsc, diffusivity of the backreflector, conductance and thickness of the ITO, etc.). In this program, ECD and United Solar are developing a system of in-line, real-time diagnostic systems to measure the characteristics of material produced in the 3 deposition machines: the backreflector (BR), amorphous silicon (a-Si), and top conductive oxide (TCO) machines. At a minimum, these devices have the potential of alerting operators to production problems in a timely fashion; the potential also exists to eventually use these systems for online optimization of material during the production process. By using in-line sensors and diagnostic systems which will be developed under this program in our production machines, we expect to improve PV module efficiency, yield, and throughput.

In the first year of this program, the hardware systems were developed and tested on the bench, and new second generation systems designed for installation in the deposition equipment vacuum systems. In the second year, these systems will be used in a production environment and we will begin developing software for data acquisition, analysis, and interfaces to the operator. During the third year, we will begin to develop a data base to connect results of online measurements with data from the complete offline QA/QC measurements of the final product.

During this program period, we are working on the following systems:

- BR Machine: Most work for the backreflector is concentrated on developing a new device, a Scatterometer, to characterize the absolute and diffuse/specular reflectance of the backreflector. The backreflector consists of a layer of reflective metal (either Aluminum or Silver) covered by a layer of transparent, conducting ZnO. Both the metal and the oxide have textured surfaces, such that at least part of the light that did not get absorbed in the a-Si on the first pass is reflected at an angle. Such a backreflector increases the probability of absorption, along with the solar cell efficiency, by about 20%. In addition, we are also developing a spectrometer to measure the thickness of the ZnO.
- a-Si Machine: We are developing a new system, the PV Capacitive Diagnostic (PVCD) to measure the properties of the a-Si material as it is being deposited in the a-Si machine.

- TCO machine: This machine already uses an optical spectrometer to measure thickness and n and k of the TCO. Our goal is to be able to be able to eventually use this diagnostic as part of a closed loop system to control the thickness and composition of the oxide in the later part of this program.

Below we describe the work that has taken place during the first year of this program in developing the new Scatterometer and PVCD.

Backreflector Characterization Sensors

Objectives

The objectives include the development of prototype backreflector characterization sensors for measuring ZnO film thickness and backreflector light scatter (texture).

- design and construction of the benchtop measurement systems
- software programming for system control and data acquisition
- measurement system characterization (i.e. stability, repeatability, etc.)
- backreflector sample measurements
- data analysis and correlation studies
- evaluation of various system configurations
- development of the 2nd generation deposition machine sensors

The overall objective is to develop real-time, in-line sensors for monitoring and/or controlling backreflector properties which will provide for continuous process improvement and contribute to our overall PVMat 5A goals of 5% increase in PV efficiency, 3% increase in yield and 10% increase in throughput.

Benchtop System Descriptions

Backreflector ZnO Film Thickness Measurement System

The ZnO film thickness system measures the normal specular reflectance vs. wavelength (360-1000 nm) and from the reflection minima wavelengths, estimates ZnO film thickness. The system consists of a PC-interfaced, 2048 element spectrometer, a quartz-tungsten-halogen light source, a bifurcated fiber optic cable with reflection probe, and probe and sample mounting hardware as shown in Figure 11. A Visual Basic 4.0 program controls the spectrometer, acquires the data, and performs the spectral analysis.

Backreflector Scatterometer

The backreflector scatterometer, or diffuse reflectance system measures diffuse (scattered) reflectance vs. scattering angle of laser light. The resulting data is an indirect measurement of backreflector film texture and can be correlated with final solar cell device parameters such as Isc, Voc, FF, and Pmax. A basic schematic of the backreflector scatterometer is shown in Figure 12.

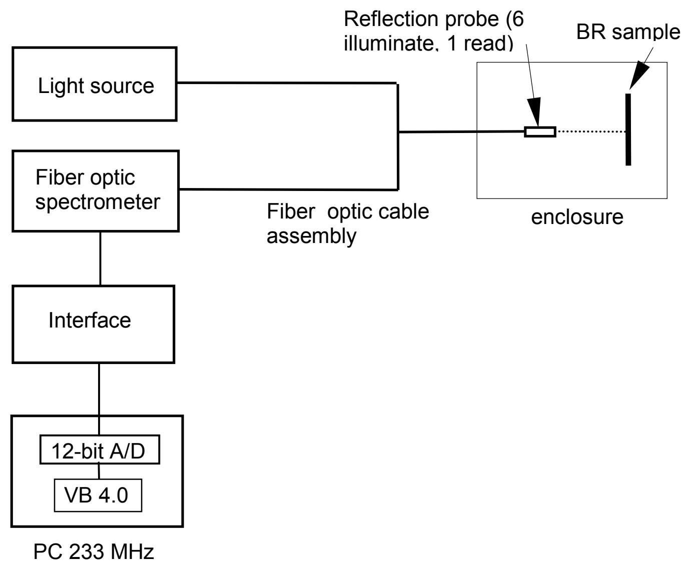

Figure 11. Schematic of the benchtop backreflector ZnO film thickness measurement system.

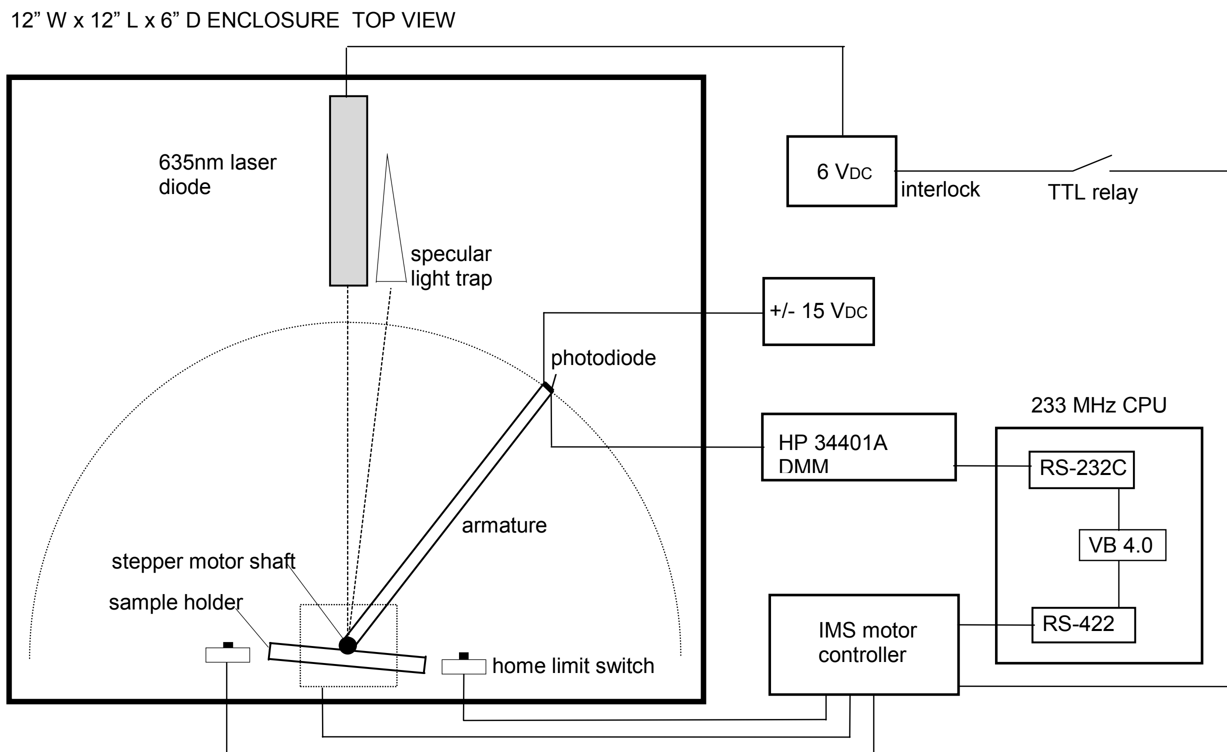

Figure 12. Schematic of the benchtop backreflector scatterometer.

This benchtop system consists of a 4 mW, 635 nm laser diode light source which illuminates a backreflector sample at some off-normal angle. A 5 mm^2 silicon photodiode is mounted to a stepper-motor armature and is coplanar with the incident laser beam. The armature is rotated under computer control to detect reflected light from the sample over 180 degrees. The photodiode has an integrated amplifier which provides current-to-voltage conversion for input to a voltmeter or A/D board. The stepper motor is controlled by sending commands to its controller over the RS-422 port which is installed in the computer. A limit switch is installed to provide a reference "home" position. Laser operation is controlled by a digital relay connected to a digital output on the stepper motor controller. A Visual Basic 4.0 program was written to control the instrumentation and acquire data. The program displays a real-time graph and saves data to an ASCII file for further analysis. The laser diode, photodiode, and sample are enclosed in a 12" x 12" x 6" enclosure to eliminate ambient light effects. The interior of the enclosure and mounting hardware have been painted with ultra-flat black paint a specular light trap is used to minimize multiple reflections. Diffuse reflectance scans are automatic while specular measurements require more precise positioning of the detector and the use of a neutral density filter to attenuate the signal (to avoid detector saturation). Some of the system characteristics are listed below:

- laser diode output stability: <1% (after 1 minute warm-up)
- laser diode lifetime: 50,000 hrs. typical (dependent on operating temp, current spiking)
- optical axis: 75 mm from inside bottom surface of the enclosure
- distance from detector to sample: 112 mm
- distance from laser to sample: 160 mm (inside laser face)
- detector area: 5 mm^2 diameter = 2.52 mm
- signal noise level: ~ 0.05 mV
- dynamic range: ~ 2.8 E+5 (0.05 mV - 14 V)
- repeatability: <1% difference per data point over +70° to -70°
- scan time: ~0.9 sec/reading, ~2 minutes for complete scan at 1.3° resolution

Data Analysis: Backreflector Scatterometer

Laser Diode Stability

The stability of the laser output has been measured over short periods of time after power up. These measurements were performed because having the laser turned off between production deposition scans in order to increase laser diode lifetime would be desirable. Various cycling routines were tested and the reproduciblity of laser output was found to be about 1% even when cycling the laser diode off and on and allowing as little as 1 minute warm up.

Sample Measurements

Scans have been performed on various types of samples such as:

1. silver mirror
2. labsphere spectralon sample (near ideal diffuse sample)
3. 5 mil stainless steel substrates
4. 5BR production samples with specular aluminum and thick ZnO layer
5. 5BR production samples with textured aluminum and thin ZnO layer
6. R&D experimental samples with varying silver texture and varying ZnO layer thicknesses

As one would expect, each type listed above exhibits a different diffuse reflectance characteristic. A plot comparing the six different samples is shown in Figure 13. The spectralon sample has the highest and most lambertian scattered signal with no specular component, while the silver mirror has the lowest scattered signal with the highest specular component. The stainless steel substrate has a slightly more diffuse signal when compared to the silver mirror. All of the backreflector samples, production and R&D, have diffuse signals ranging between that of the stainless steel substrate and spectralon sample.

Significant differences in the measured scattered reflection are also observed for the 2 types of production 5BR samples, namely, specular aluminum with thick ZnO (5BR 79) and textured aluminum with thin ZnO (5BR 494). However, the Jsc of devices deposited on these types of backreflectors are not so different. The scattered component beyond 15-18 degrees of the specular aluminum backreflector is much lower than that of the textured aluminum backreflector. Also note that the textured aluminum backreflector shows higher scattered reflection between 27-45 degrees than around 20 degrees from incident. This is a very distinct characteristic not seen in any other types of backreflector. Also note that the specular peaks vary and are clipped in the graph.

Another observation is that the stainless steel substrate has a grating-like, or grooved, characteristic in one direction (along the length of the web). This striation results in an increase in the diffuse signal within 30 degrees of specular. It was decided to orientate all samples with the striation parallel to the measurement plane thus eliminating this effect from the measurement.

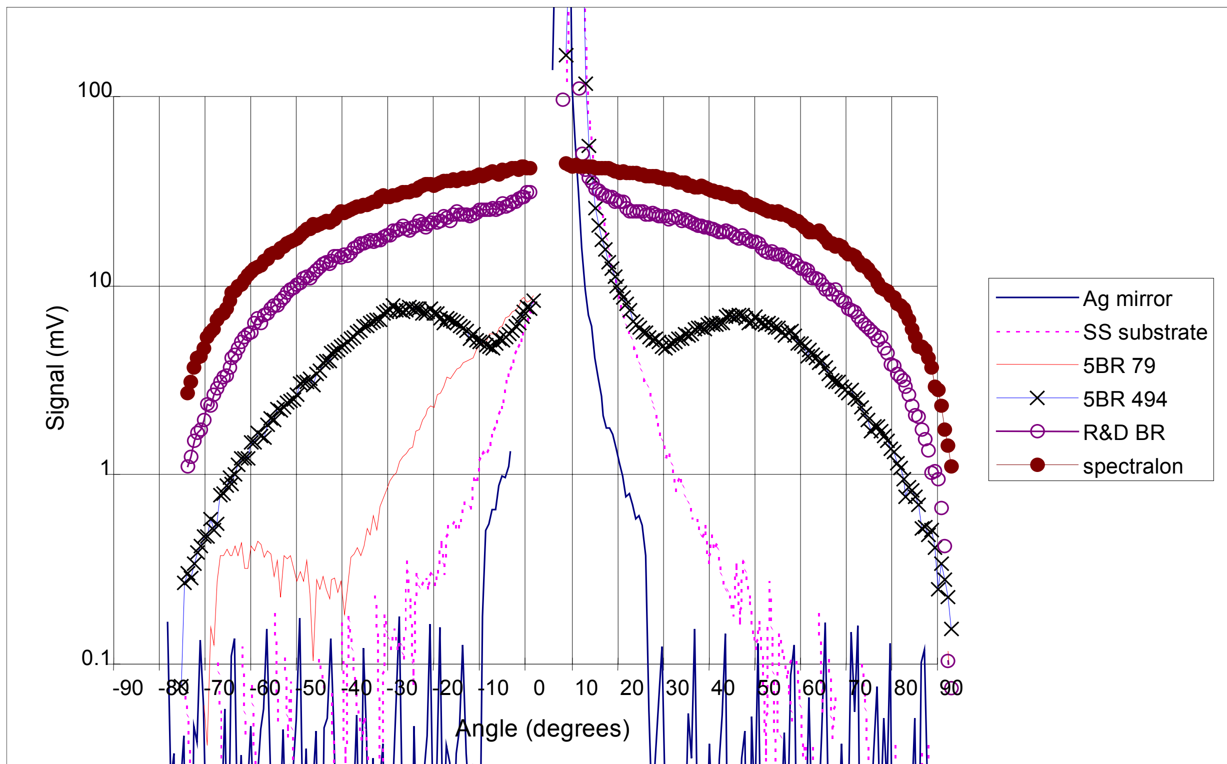

Figure 13. Diffuse reflection comparison of various samples.

Light I-V Correlation Studies

A correlation study was performed in order to determine the relationship between diffuse and specular reflectance and cell I-V data. Seventeen backreflector samples from 5BR run number 534 were used for the study. The samples were part of an R&D experimental run which varied Ag texture and ZnO thickness. The diffusivity curves were similar in shape with slight differences in the scattered reflection component.

The application software, Statistica 5, was used to generate Pearson correlation coefficients, r, and p-levels (probability of error) which are listed in Table 3. In Table 3, larger r values (positive or negative) indicate stronger correlations. P-values less than 0.05 indicate correlations that are significant or "reliable". Although the sample size is relatively small, it appears that a correlation does exist between diffuse reflectance and the 4 measured cell parameters (Q>610, Pmax, Voc, and FF). Q>610 is the quantum efficiency for wavelengths > 610 nm. Thus, Q>610 is a measure of the amount of current collected from red light. There is also a correlation between specular reflectance and Pmax and FF.

Table 3. Correlation Coefficients for 5BR# 534 Samples.

Parameter	specular		Diffuse	
	R	p	r	P
Q>610	-0.443	0.098	0.559	0.030
Pmax	-0.796	0.000	0.869	0.000
Voc	-0.557	0.031	0.590	0.021
FF	-0.881	0.000	0.883	0.000

In Table 3, larger r values (positive or negative) indicate stronger correlations. P-values less than 0.05 indicate correlations that are significant or "reliable".

Correlation vs. Scattering Angle

Additional correlation studies were conducted on the diffuse reflectance data for the 17 experimental samples discussed in the previous section. The relationship between cell parameters (Q>610, Pmax, Voc, FF) and the following diffuse reflectance data were investigated:

- diffuse reflectance at single angles
- diffuse reflectance integrated over 5° sections
- diffuse reflectance integrated over 10° sections

The study was conducted in an attempt to determine whether stronger correlations exist for particular scattering angles, or smaller integrated sections versus the larger integration which has been studied prior. The result of this study may be related to the 2nd generation sensor design where constraints imposed by the deposition machine geometry may limit detection angles.

Figure 14 plots the correlation coefficient (Pearson r-value) for each cell parameter calculated at single scattering angles. Although correlations were calculated for angles from 4 to 73 degrees in 3 degree steps, only those which are "statistically significant" are plotted (i.e. those with p-value < 0.05). As shown in Figure 14, Pmax and FF exhibit stronger correlation than total Q>610 and Voc. It appears that the r-value for Pmax and FF is relatively independent of scattering angle for angles greater than 28 degrees, while there is a weak dependence for Q>610 and Voc. Next, the diffuse reflectance signal from 25 to 70 degrees

was integrated over small sections, 5 and 10 degrees, and the correlations recalculated. No significant change in the coefficients was observed.

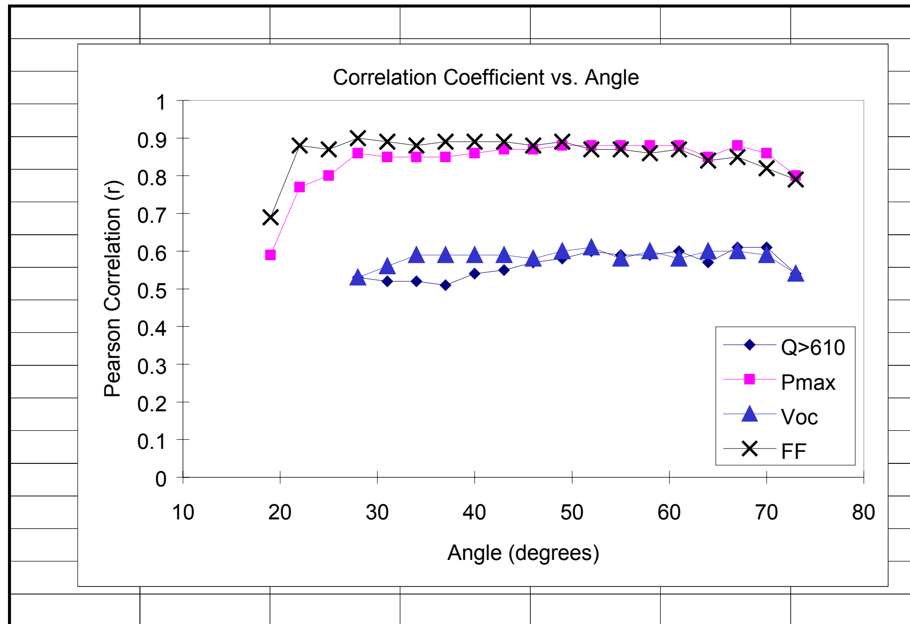

Figure 14. Plot of correlation coefficients for each cell parameter calculated at single scattering angles (17 R&D samples).

The study was repeated for 12 production 5BR samples (runs in 517-542 range). The structure is thin ZnO on textured aluminum on stainless steel substrate. The correlations between the cell parameters and single angle diffuse reflectance were calculated and are plotted in Figure 15. Again, only "statistically significant" correlation coefficients are plotted. No correlation is observed for Voc and FF. However, correlation is also observed for total Q>610 and Jsc near specular angles.

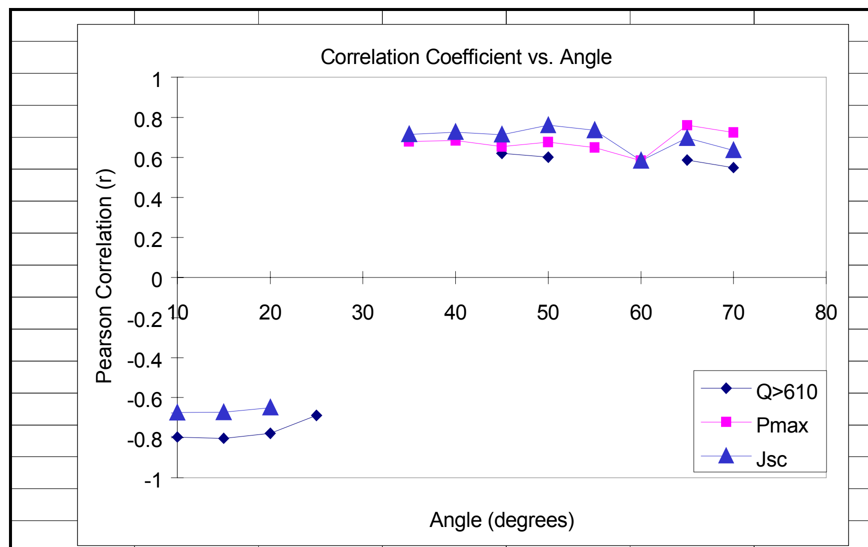

Figure 15. Plot of correlation coefficients for each cell parameter calculated at single scattering angles (12 5BR production samples).

Dependence of Diffuse Reflectance on Incident Angle

The configuration of the scatterometer was slightly modified in order to observe differences in diffuse reflectance between near-normal incidence (6°) and off-normal incidence (22.5°). The incident angle of the laser light onto the sample was set to 22.5° by rotating the sample stage as shown in Figure 16.

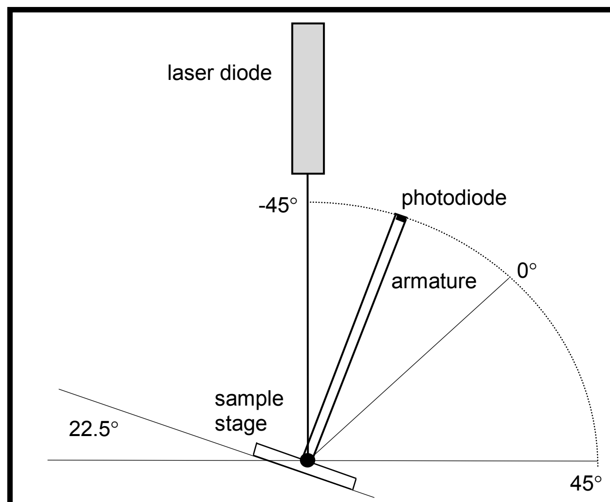

Figure 16. Schematic of the modified scatterometer configuration.

Measurements were repeated on one sample previously scanned with the near-normal incidence setup (6° incidence). Figure 17 compares the two scans for back-reflector sample 5BR 531. As is shown by the plot, the measurements for the two configurations are slightly different. With the modified setup, light scatter is slightly decreased at the oblique angles, 0 to 45 degrees. It remains nearly the same over the acute angles, 0 to -40 degrees.

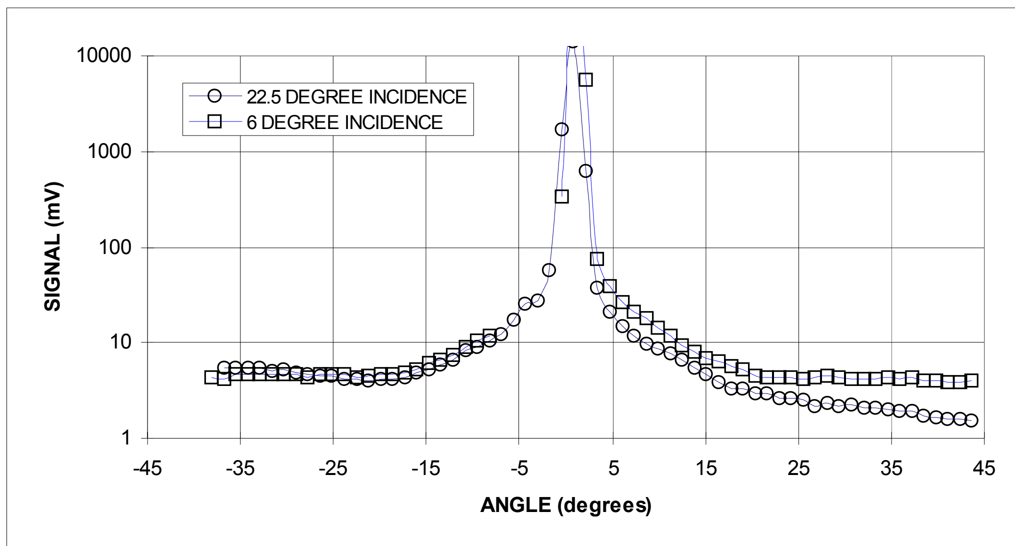

Figure 17. Comparison of light scatter for 5BR 531 using 2 different angles of incidence. "Angle" is with respect to the specularly reflected beam.

Data Analysis: ZnO Thickness Measurement

Reflection minima were measured for several 5BR samples from an R&D experiment, 5BR 534. Table 4 below shows the measured values together with the corresponding ZnO deposition current. A software routine is currently being developed to determine ZnO thickness using the measured reflection minima / maxima.

Table 4. Measured Reflection Minima for 15 R&D Backreflector Samples.

SAMPLE	MIN1 (nm)	MIN2 (nm)	MIN3 (nm)	MIN4 (nm)	ZnO Current (A)
534-2	887	449	377		3
534-3	858	625	499	427	9
534-4	930	582	440	384	6
534-6	894	462	376		3
534-7	956	608	456	387	6
534-8	957	617	463	389	6
534-9	953	609	457	388	6
534-10	805	458	372		3
534-11	752	551	447	391	9
534-12	931	585	442	368	6
534-13	828	607	487	420	9
534-14	886	440	370		3
534-15	880	435			3
534-16	895	558	426	350	6
534-17	833	607	485	419	9

2nd Generation Sensor Development

Backreflector Scatterometer

The overall phase 1 objective thus far, with regard to the backreflector scatterometer, has been to determine what measurement configuration and scattering angles are necessary and whether a correlation exists between light scatter data and cell performance. These issues are related to 2nd generation sensor design which will be incorporated into the production backreflector deposition machine. Initial design issues include the geometry and space limitations of the gas-gate ports and the required detection angles necessary for meaningful data. Advantages of sensing at the gas-gate ports are:

- the possibility for multiple sensors one after Al deposition and one after ZnO deposition
- the gas-gate ports already exist and no additional machining of the back reflector chambers is required (which would be cost and time prohibitive)

The disadvantage is that design space becomes limited and sensing angles may be restricted.

Backreflector ZnO Film Thickness Measurement System

Incorporation of the ZnO thickness sensor into the backreflector machine should be straightforward. Access will be provided by the gas-gate port located just beyond the ZnO cathode.

PV Capacitive Diagnostic (PVCD) System

Introduction

The PVCD is a non-contacting device that is being developed to measure parameters of the photovoltaic cells during the manufacturing process. We expect, at a minimum, to be able to measure the open circuit voltage (V_{OC}); other parameters that we may be able measure include quantum efficiency (Q), fill factor (FF), shunt impedance (R_{SHUNT}), and capacity (C). Since this is a non-contacting device, it is not necessary to have a TCO coating on the PV material in order to make these measurements; consequently, these parameters can be measured in the machine as the material is made. By placing one of these devices in the gas gates following each of the p-chambers, each of nip layer can be separately analyzed. These devices will provide the operator with nearly instant feedback of problems and potentially increase the bandwidth for optimizing machine parameters by a couple of orders of magnitude.

Principle Of Operation

Figure 18 is a schematic of the PV Capacitive Diagnostic (PVCD) device.

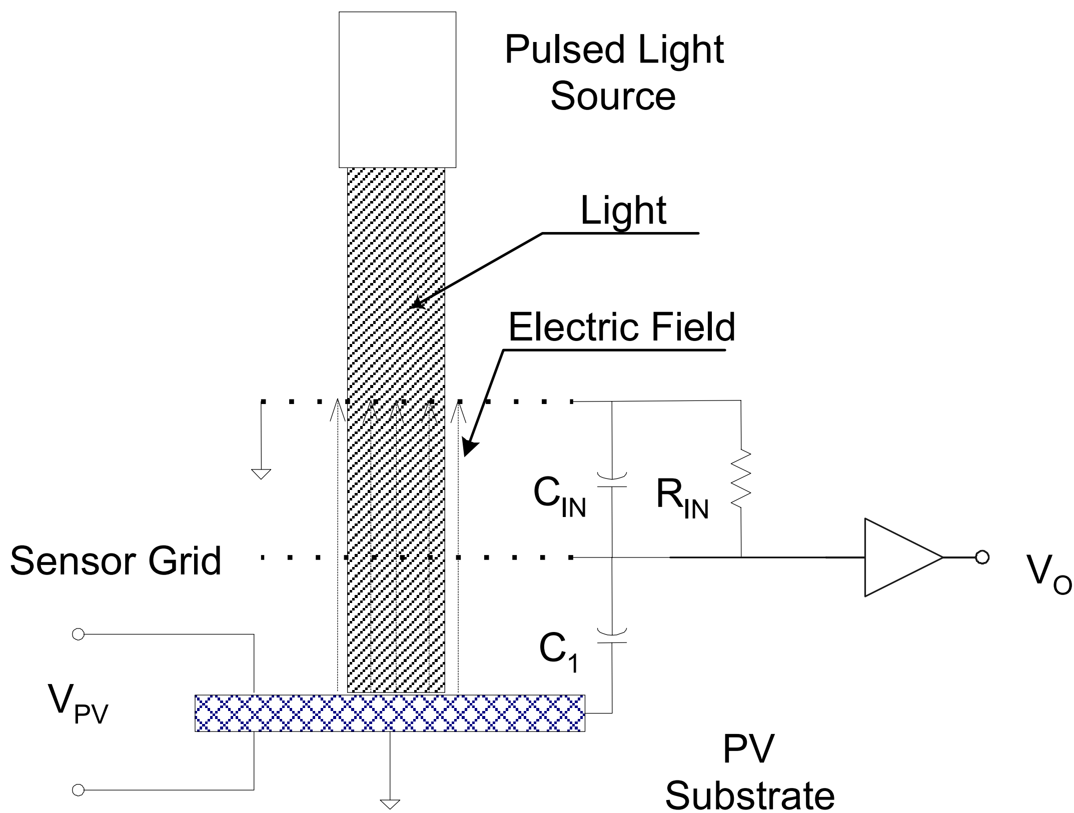

Figure 18. Electrical schematic of the PVCD.

In the regime where $C_{IN}R_{IN}$ is much greater than the time width of the pulse of light,

$$V_O = V_{PV} \bullet \left[\frac{C_I}{C_I + C_{IN}} \right]$$

$$\approx V_{PV} \bullet \frac{C_I}{C_{IN}}, \quad (C_{IN} >> C_I)$$

where C_I is the capacity of the sensor grid to the PV substrate, and C_{IN} is the capacity between the sensor grid and the grounded grid. C_{IN} is typically much greater than C_I due to the additional input capacity of the amplifier and the capacity of the cable connecting the amplifier to the sensor grid.

The simplest application of this device is to merely turn on and off the light with a square wave pulse; the output of the PVCD will then be a square wave proportional to the open circuit voltage of the PV material as shown in Figure 19.

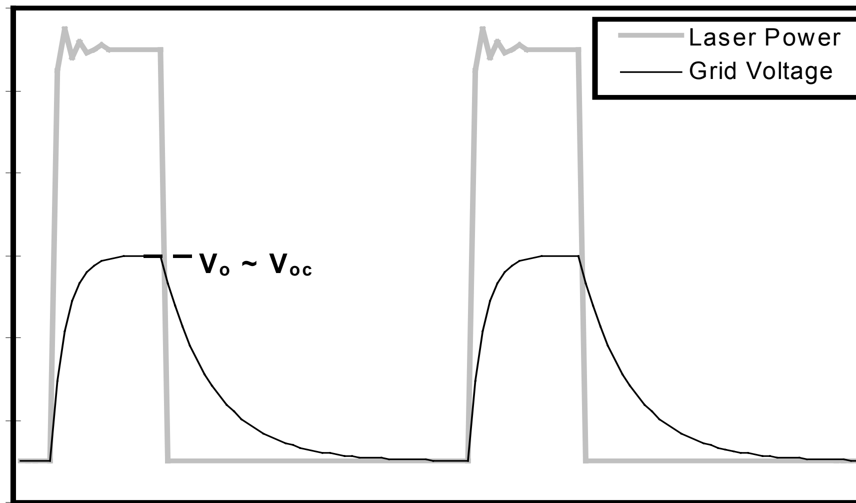

Figure 19. Light (laser) and voltage waveforms from the PVCD.

We conjecture that the peak voltage will be proportional to $V_{oc.}$ In the time period shortly after the light is first turned on, where $V_{PV} << V_{oc}$, the rate of change of V_{PV} should be proportional to the ratio of the device short circuit current to the device capacity, *C*. At the end of the light pulse, the capacitance charging current is 0, and the cell is at V_{oc}. When the light is turned off, the rate of change of V_{PV} should be inversely proportional to the product of *C* and the device shunt resistance, *Rs*. By measuring the charging current and open circuit voltage as a function of light intensity, we should also be able to derive the FF.

Bench-Top System Design

A benchtop test system was designed and built. This system is shown in Figure 20. The black rectangular object just left of center in the figure is a 20 mW 680 nm diode laser with an attached expander on the front to expand the 6 mm diameter beam by a factor of 3 in diameter. We have also procured an 80 mW 790 nm IR laser with a times expander. The laser power module is in the aluminum box to the left of the oscilloscope.

The high input impedance buffer amplifier is in the blue box behind the laser. The PVCD test device is located just to the left of the laser. The device has been designed to easily accept the standard 5 cm × 5 cm test cells produced at ECD and United Solar. On the front face of the device can be seen an aluminum screen corresponding to the top grounded grid in Figure 18. We have successfully used metal grids as well as ITO coated glass for the grids. On the oscilloscope to the right, one can observe the laser waveform (square wave) as well as the signal from the PVCD to be very similar in character with those shown in Figure 19.

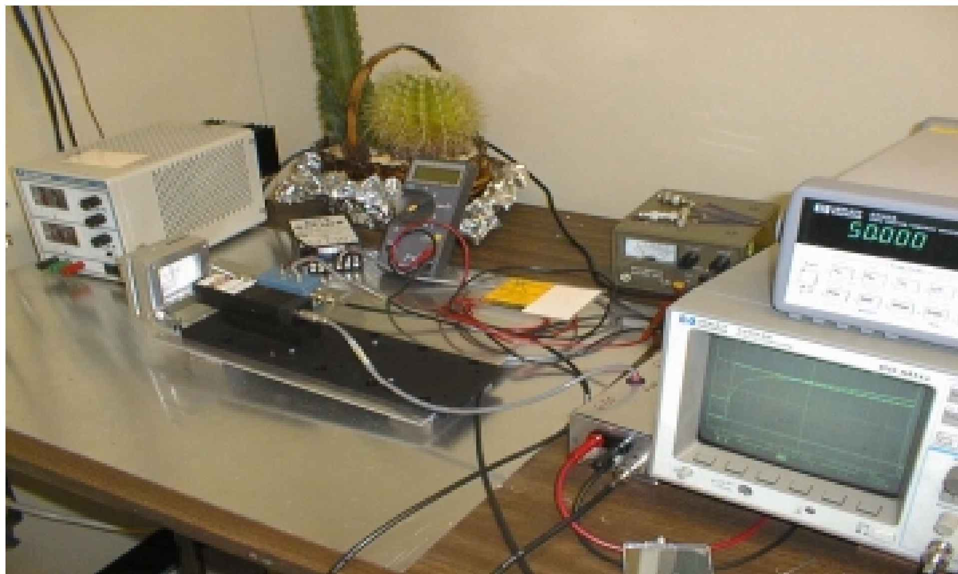

Figure 20. Photograph of the PVCD bench-test system. The oscilloscope is displaying the waveforms of the laser pulse (the step function) and the output of the PVCD. Notice the similarity between the stored traces on the oscilloscope and the waveforms in Figure 18.

Below we summarize some of the measurements made with this system and the design of the second generation system that is being installed in the 5 MW a-Si deposition machine.

Establish Basic Operation

We began tests using cells with a top ITO coating that allowed simultaneous measurements of the cell using a direct contact and the PVCD. These two measurements allowed the determination of whether the output of the PVCD accurately reproduced the voltage of the solar cell material. The agreement was near perfect as shown in Figure 21.

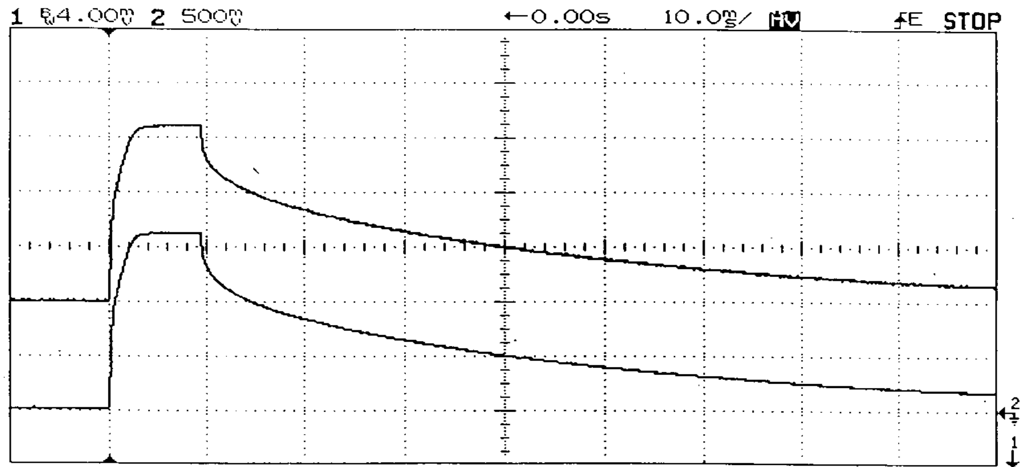

Figure 21. Oscilloscope traces of a PV cell using both the bench-top PVCD (upper trace) and a probe in direct contact with the ITO (10 ms/div). The laser is pulsed on after 10 ms, and switched of after 20 ms.

This agreement was verified using both aluminum screen and ITO coated glass for the sensor electrode.

Compensation for Finite Time Constant

A critical look at Figure 21, however, shows that the signal from the PVCD (upper trace) is actually decaying a bit faster than the direct measurement (lower trace). This is due to the finite resistance of the buffer amplifier (10^{11} Ω) which gives the circuit a time constant of about 1.4 s. The time constant is measured (as shown in Figure 22) and software is used to correct for this effect. We also designed an amplifier with a much higher input resistance ($\cong 10^{13}$ Ω) which will make future software corrections unnecessary. Prototype versions of this new amplifier are working well and the new amplifier design is being used in the second generation system that is currently being installed in the 5 MW.

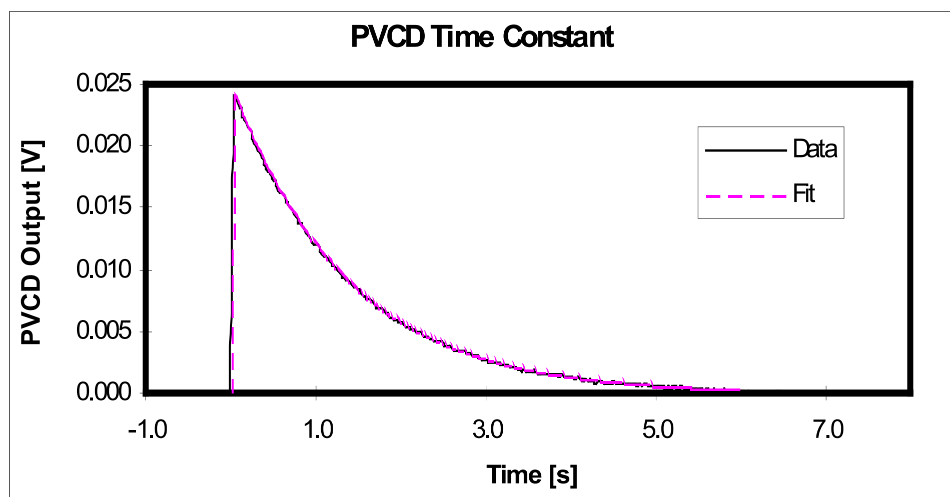

Figure 22. Measurement of PVCD time constant. A simple single pole filter with a time constant of 1.3686, fits the data over 3 seconds with less than a 0.01% relative error.

Measurement Reproducibility

In order for this system to be useful as a diagnostic system, a high degree of reproducibility is needed. Variations come from different sources, such as:

- Changes in the distance, and consequently capacity, between the pick-up grid and the substrate;
- Changes in the shunt capacity of the line connecting the grid to the buffer amplifier. A very significant change can result from a minor perturbation such as bending the coaxial cable between the pick-up grid and the buffer amplifier; and
- Changes in the amplitude of the laser pulse.

All of the above, and other, sources of "signal non-reproducibility" have been and are being investigated. Some of them have been corrected, and other are still being studied and will need software corrections and active feedback systems. In particular, we measured the stability of the laser and found a large difference in stability in different lasers. Whereas the IR laser and corresponding PVCD output are stable to within our measurement precision (1 LSB on the digital oscilloscope as shown in Figure 23), we found that the red laser, which we are installing in the 5 MW in the second generation device, has amplitude variations of the order of 5%. A software system will need to be developed in the second year of the program to provide active feedback for this system.

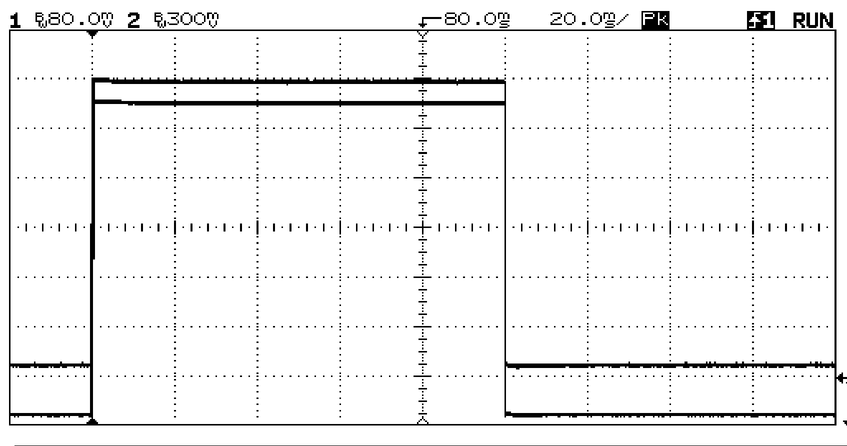

Figure 23. **Oscilloscope traces of the laser diode module Current monitor (top) and output of a photodetector (bottom). The oscilloscope recorded the peak voltages for each of these signals.**

Summary of Selected Preliminary Measurements

Figure 24 shows the output of the PVCD device for cells with the following structures:

- n1, i1, p1, n2
- n1, i1, p1, n2, i2
- n1, i1, p1, n2, i2, p2

One can clearly see the increase in the PVCD output as more layers are added. One can also observe the precision to which these PVCD waveforms can be fit to models using only a few parameters. We are now beginning the work of correlating these fitting parameter with cell properties measured using conventional techniques as shown in Figure 25.

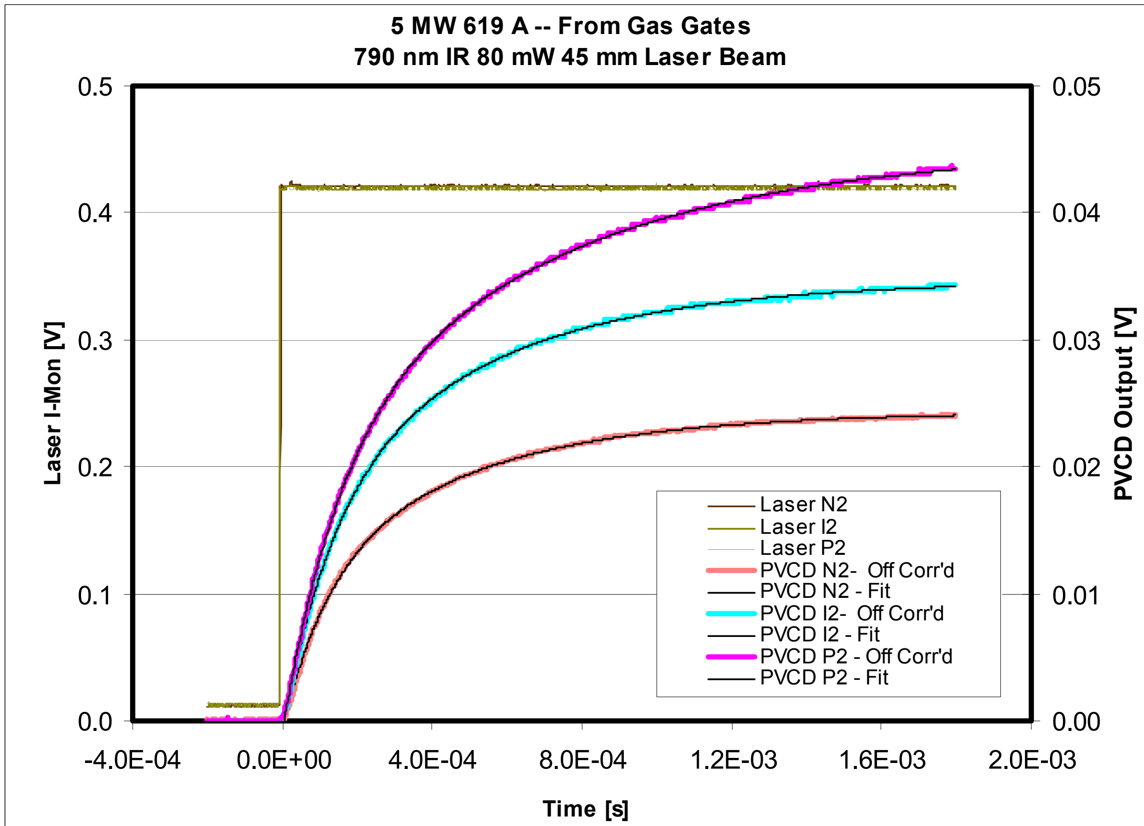

Figure 24. PVCD waveforms and fitted curves resulting from a 4-parameter fit.

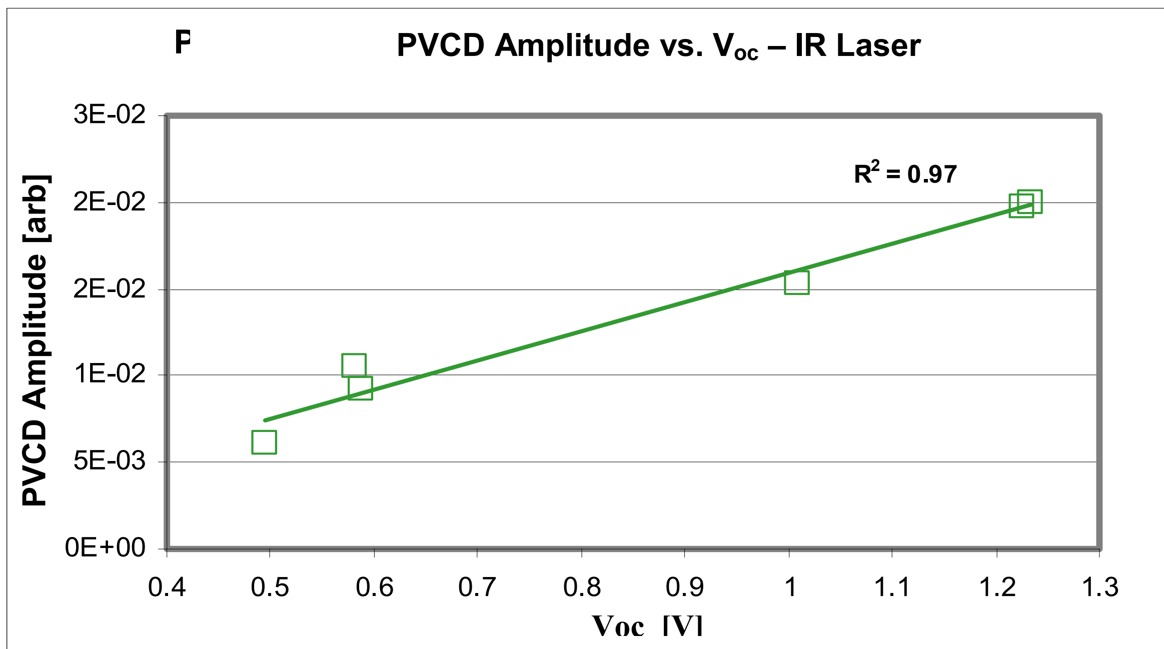

Figure 25. Parameter resulting from fit of PVCD waveform plotted vs. measured open circuit voltage for cell with a different number of layers.

Design of the Second Generation Device for Installation in the 5 MW

Two second generation devices have been designed:

- The first system was designed such that it could be mounted using windows in the gas gates of the production equipment. This system has several advantages: (1) there is no worry of contamination; (2) the system can be accessible at all times, even during operations, for modification; and (3) systems can be installed in the gas gates following each of the 3 p-layers to analyze separately each cell in the triple junction device.
- We designed the second system to be mounted in the vacuum system of the take-up chamber following deposition of all the layers of the triple-junction device. Because this system is separated from the deposition chambers by a gas gate, again the worries of vacuum compatibility are eliminated.

Windows were not initially installed in the gas gates of the 5 MW machine; consequently it would be necessary to remove and re-machine these chambers of this machine to implement the first design; the second design, however, could be installed without needed to disassemble the machine, and consequently offered a much lower risk approach.

Although we originally envisioned installing the second generation device in the pilot machine, we have instead decided to immediately install it in the production equipment for the following reasons:

1. We believe that this new system may be able to be immediately useful, for example, in alerting the operator to a serious problem in the system.
2. The production equipment is in operation nearly all the time, whereas the pilot machine is only intermittently operated and is frequently off-line for extensive modifications.
3. Consequently, we shall be able to obtain much more data by installing the system in the production equipment. Furthermore, all the production material goes through extensive off-line QA/QC electrical testing that will automatically provide us with data for comparison to the online measurement.

The hardware for this second generation system has already been installed in the 5 MW take-up chamber, as shown in Figure 26. The electrical hook-up will be completed in the near future.

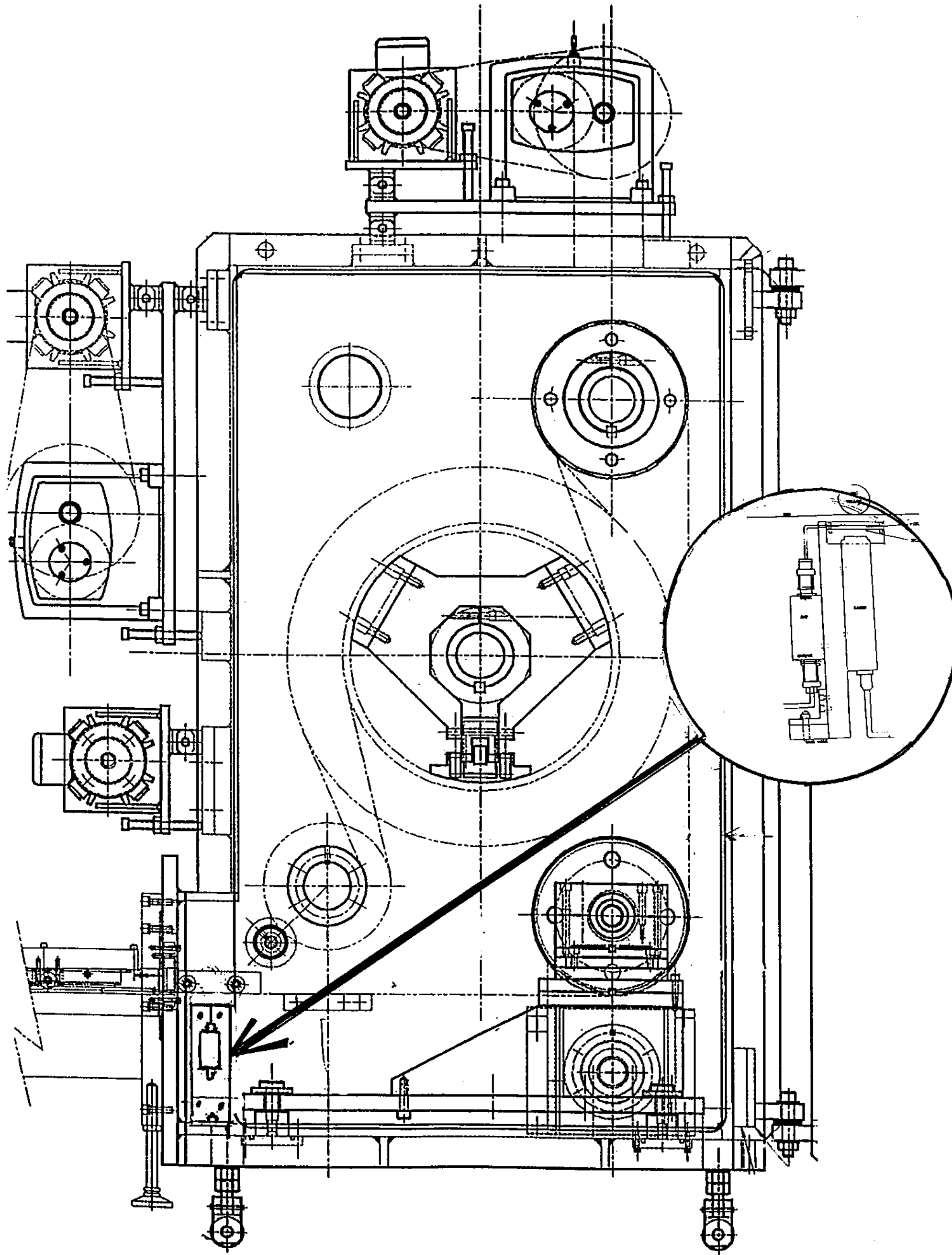

Figure 26. **Mechanical schematic showing the mounting of the PVCD in the take-up chamber of the 5 MW.**

Task 3 – Development of Reactive Sputtering Process Using Inexpensive Zn Metal Targets for Back Reflector Preparation

Background

An integral part of ECD's triple-junction solar cell design is the textured metal/ZnO back reflector which enhances the probability for multiple light passes through the semiconductor absorbing material. The increased number of passes increases the chances for light absorption which in turn leads to higher short circuit currents and higher cell efficiencies. While the back reflectors are needed in order to achieve certain efficiency goals, the cost of making these materials on the production level is significant. In particular, the materials costs exceed those for the semiconductor layer deposition process.

A significant expense in the magnetron sputtering process used to make the back reflectors is the cost of the ZnO targets. The cost of these targets alone accounts for over 40% of the total material cost for producing all of the thin films for the solar modules. Thus, if the ZnO targets could be eliminated from the process with a less expensive target, a significant cost savings would result.

Prior to this program, the ECD research team tested a reactive sputtering process which uses a Zn metal target in an Ar/O_2 atmosphere to create ZnO films for back reflectors. Since the price of Zn metal targets are $1/5^{th}$ the price of ZnO targets, and conceivably could be made in-house at an even lower cost, reduced cost was a major incentive to test the feasibility of this process. However, there were other motivations. With the present process, high quality back reflectors are obtainable at production level web speeds. However, at slower speeds (2/3 of the production level speed) back reflectors of even a higher quality can be obtained due to thicker ZnO layers obtainable at these slower speeds. Thus if higher sputtering rates could be obtained, the thick ZnO layers and higher quality back reflectors could be obtained at production level speeds. Since higher deposition rates are likely obtainable with the Zn metal target, improved efficiencies as well as reduced costs may be had with this new process.

Table 5 compares data from this initial feasibility study for single-junction a-Si:H cells prepared with back reflectors (Zn 29 and Zn 33) made using this new deposition process and cells made with back reflector from the 5MW production machine (5MWBR78 and 5MWBR82). The semiconductor layers for all of these cells were co-deposited in the same deposition chamber under deposition conditions which were not optimized. ITO and Ag contacts for the cells were also co-deposited in order to minimize any differences in the cells other than the back reflector materials. The data for samples Zn 29, 5MWBR78 and 5MWBR82 are all the same within experimental error. The J_{sc} for sample Zn 33 is higher than the other values, however the FF is lower with an overall slight improvement in efficiency. Thus, with little optimization it can be concluded from this data that back reflectors can be made using the new reactive sputtering process, having similar quality to those made using the present 5 MW process.

Table 5. Comparison of Data for a-Si:H Cells Co-Deposited on Al/ZnO Backreflectors. Cell Measurements Completed Using AM1.5 Light (R_s is the series resistance).

Sample	V_{oc} (V)	J_{sc} (mA/cm^2)	FF	P_{max} (mW/cm^2)	R_s (Ωcm^2)
Zn 29	0.952	14.54	0.644	8.91	10.7
Zn 33	0.955	15.06	0.638	9.19	11.5
5MWBR78	0.953	14.45	0.647	8.92	11.9
5MWBR82	0.953	14.30	0.646	8.80	12.5

Objective of Backreflector Studies

While the data from the initial studies are encouraging, there are several issues which need to be addressed before this new process can be incorporated into the 5MW production line. Although some of these issues can be addressed using small-scale machines, the process needs to be qualified on ECD's pilot roll-to-roll machine before implementing it in the production facilities.

In this program, we are testing the feasibility of using this reactive sputtering process in a roll-to-roll process to verify that it can indeed be used to make long rolls of back reflector coated stainless steel webs in production. A pilot roll-to-roll machine is being used to prepare and optimize ZnO layers prepared using the Zn metal targets. During initial optimization of the deposition conditions, small area cells are being fabricated using the new ZnO materials to judge the back reflector quality. Once the quality of the ZnO materials using the reactive sputtering process are judged to be similar or better than those made using the ZnO targets, 100M lengths of back reflector material will be made to demonstrate that the process can be reproducibly used over a long production level length. In the later stages of the program, the processing speed will be increased to a level 1.5 times faster than what is obtained in the 5MW production line.

Experimental

In the first year of the program, the reactive sputtering process was optimized in the pilot machine located at United Solar (see Figure 27). This roll-to-roll machine is part of United Solar's decommissioned 2 MW plant and is designed to deposit BR material over a 14 in. wide web. It can be equipped with two Al targets and four ZnO or Zn targets of size 4" x 20". To optimize the backreflector deposition conditions, the pilot machine was used to deposit thick ZnO layers onto a stainless steel web previously coated with a standard Al layer and a thin ZnO layer using the 5MW production equipment. Depending on the deposition conditions, Al thin films can have different degrees of texturing which strongly affect the reflection and solar cell properties. In using the Al/thin ZnO coated web made using the 5MW production line, we were assured that the degree of texturing was similar to that obtained in production and could thus optimize the thickness and quality of the ZnO layer accordingly to that amount of texturing. The thin layer of ZnO was used to prevent oxidation of the Al surface during transportation of the web from the production machine to the pilot test machine.

To optimize the properties of the ZnO layer, a number of deposition parameters were systematically varied including the substrate temperature, the oxygen and argon flows, web speed and the applied rf power. Also compared films were made using an Al doped Zn metal target to those made using an undoped target. As a reference, ZnO layers were also made using the standard ZnO targets and the pilot machine.

To test the quality of the back reflectors, a-SiGe:H nip structures were deposited on 2" x 2" experimental back reflector coated substrates using the 13.56 MHz PECVD technique and an R&D deposition system. This system has been used to prepare 1 sq. ft. modules with world record efficiencies (>10% stable efficiencies). For each PECVD deposition, nip structures could be deposited on nine different back reflectors. In many of these depositions, high quality back reflectors with the thick ZnO layers made in United Solar's small scale R&D RADLAS system were included for comparison. The back reflectors for most of their world record solar cells and modules were made using this system. The nip structures were then coated with separate 0.25 cm^2 ITO layers for collection. The top contact was completed by depositing Al grids on top of the ITO layers.

Figure 27. United Solar's roll-to-roll backreflector machine. This machine is also part of United Solar's decommissioned 2 MW plant and will be used for the bulk of Task 3, and for part of Task 2.

Cells were characterized using standard IV tests and quantum efficiency measurements. The IV measurements were made using AM1.5 light or AM1.5 light filtered using a 610nm low bandpass filter. The filter simulates absorption due to the top and middle cells allowing only red light which reaches the bottom cell in the triple-junction structure. It is important to compare data obtained using the filter due to the fact that in the high efficiency triple-junction structure, the bottom cell current is the parameter most effected by the use of the back reflector. Also using the filter eliminates any fluctuations in the blue/green light collection which is affected by a number of conditions unrelated to the back reflector including the quality of the p-layer and the ITO layer.

Results of Work Completed During Phase I of the Program

Web Handling Procedures

Initial experiments were done to determine the effect that air exposure between deposition on the Al/thin ZnO structure in the 5MW machine and placement of the coated web into the pilot machine had on the cell properties. Also the thickness of the thin ZnO layer used to eliminate Al oxide formation was determined. Three types of samples were made using the 5MW back reflector (BR) machine: 1) Al coated stainless steel, 2) same as 1) except with a thin layer of ZnO, and 3) same as 2) except the ZnO layer is twice as thick. After the 5MW deposition, samples from each of the three types were stored for one month in air or a nitrogen atmosphere. The one month exposure was to simulate the maximum time between a 5MW Al/thin ZnO deposition and our experimental ZnO depositions made using the TA2 equipment. Using United Solar's Radlus machine, we have deposited thick ZnO layers on each of these types of samples after the one month of storage to complete the back reflectors. Finally, a-SiGe:H nip cells were deposited on each of the samples to test the quality of the back reflectors and to see which type of sample we might use to complete our experiments with Zn metal targets.

Table 6 compares data for the different cells prepared using the different back reflectors. From this data, it was concluded that:

1) Use of the Al coated stainless steel without any thin ZnO coating led to poor small area cell yields and, for the most part, lower efficiencies.
2) The substrates with 40 and 80 nm ZnO stored in N_2 have the best performance in terms of the Quantum Efficiency data (Q.E.) for both the 2 day and 1 month exposure experiments.
3) The 80 nm ZnO substrate stored in N_2 has the highest Q.E. current for both the 2 day and 1 month exposure experiments.
4) The Q for both the 40 and 80 nm ZnO substrates stored in N_2 are similar for both the 2 day and 1 month exposures showing that the substrates are not changing as a function of time. For all of the other substrates, the Q is lower for the substrates left for 1 month compared with those left for 2 days demonstrating that the substrates are deteriorating as a function of time.

Considering these results, it was concluded that we would use Al/80 nm ZnO substrates and store them in an N_2 atmosphere prior to depositing the experimental ZnO layers prepared using the Zn metal reactive sputtering process.

Table 6. Data for Cells Prepared Using the Different Backreflectors After Different Exposure Environments and Exposure Times.

Sample	Storage Time Before Radlus ZnO	Storage Atmosphere Before Radlus ZnO	Efficiency (mW/cm^2)	V_{oc} (V)	FF	Integrated Q.E. Current (mA/cm^2)
Std 5MW Back Reflector	-	-	2.6 2.5 2.5	0.598 0.599 0.601	0.583 0.587 0.585	7.74 7.51 7.62
5MW Al only	2 days	Air	2.2	0.572	0.472	8.10
	1 month	Air	All	Devices	Shorted	
5MW Al/ 40nm ZnO	2 days	Air	2.5	0.588	0.506	8.82
	1 month	Air	2.6	0.598	0.600	7.45
5MW Al/80nm ZnO	2 days	Air	2.5	0.575	0.526	8.79
	1 month	Air	2.6	0.611	0.559	8.01
5MW Al only	2 days	N_2	All	Devices	Shorted	
	1 month	N_2	2.5	0.570	0.546	8.28
5MW Al/ 40nm ZnO	2 days	N_2	2.7	0.585	0.531	8.76
	1 month	N_2	2.9	0.577	0.572	8.89
5MW Al/80nm ZnO	2 days	N_2	2.8	0.574	0.533	9.67
	1 month	N_2	2.8	0.579	0.562	9.44

Reactive Sputtering Optimization

During optimization of the cells made using the ZnAl(5%) metal targets and the reactive sputtering process, a number of different deposition conditions were tested. Of the deposition parameters varied, the oxygen flow had the greatest effect on the cell properties, as one might expect. In particular, the oxygen flow strongly affected the short circuit current (J_{sc}) of the cells as is shown in Figure 28. Between oxygen flows of 40 and 70 sccm, the J_{sc} value increases by around 0.5 mA/cm^2. Further increases in the oxygen flow leads to no increase in J_{sc}. Also demonstrated in the figure is the fact that the substrate temperature has little effect on the J_{sc}. As can be seen from the data in Table 7, the average fill factors are slightly lower fill factors are obtained when the oxygen flow exceeds 90 sccm.

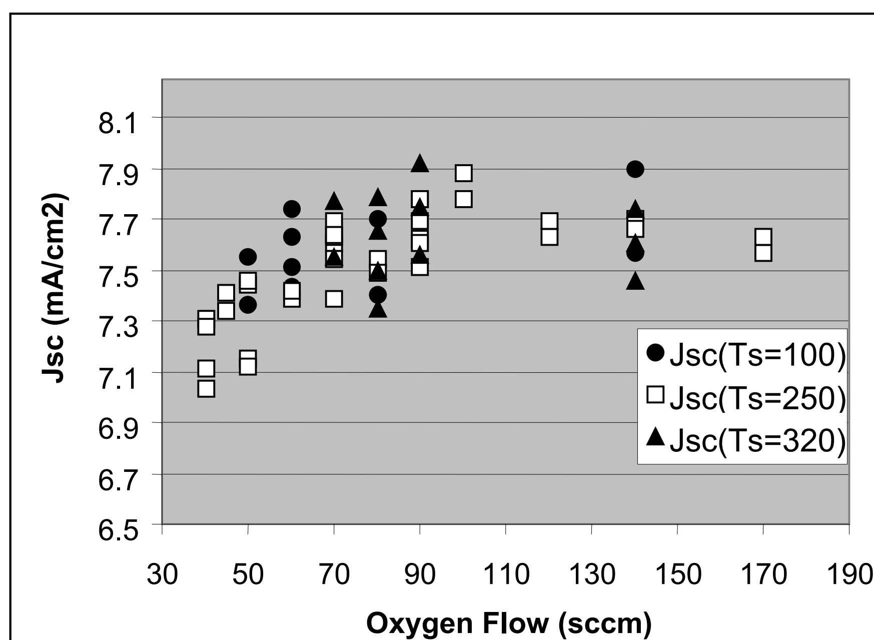

Figure 28. Dependence of J_{sc} for a-SiGe:H cells on oxygen flow. (Ts=substrate temperature)

Table 7 lists cell data for a number of cells whose ZnO layers were prepared under a variety of conditions. Parameters such as the Ar flow, the target current and the substrate temperature had little effect on the cell properties as can be seen from the data listed in the table. Also in the table are data for a cell made using just the Al/thin ZnO as the back reflector adding no additional ZnO layer using the reactive sputtering process. It is clear that the properties for this cell are inferior to those for the cells made with the additional ZnO layers demonstrating that properties for the cells are affected by the added ZnO layer.

Besides using the 5% Al doped Zn target, we also fabricated cells using a 3% doped target and an undoped target in the pilot machine. Table 8 compares cells made in the same nip deposition with back reflectors made using these three different sputtering targets. In terms of both cell properties and plasma stability, it does not matter whether the 3% or 5% Al target is used. In contrast, use of the undoped target led to poorer cell performance with the fill factors being significantly lower. In addition, optical measurements of the plasma demonstrated that the plasma with the pure metal target varied as a function of time. Specifically, the Zn plasma signal increases as does the sputtering target voltage with increased deposition time. Use of higher oxygen flows improves the plasma stability, however the plasma can not maintain the stability achieved with the doped targets. It is not yet known whether the lower FF are

associated with these plasma instabilities, however it is clear that use of the doped targets does lead to a more manageable process.

Table 7. Data for a-SiGe:H Cells Prepared with Backreflectors Made Using Reactive Sputtering Technique Under a Variety of Deposition Conditions.

Substr. Temp. (°C)	O_2 Flow (sccm)	Ar Flow (sccm)	Target Current (amps)	V_{oc} (V)	J_{sc} (mA/cm^2)	FF	R_s (Ωcm^2)	P_{max} (mW/cm^2)
250	40	30	8	0.723	7.11	0.684	11.9	3.5
250	40	30	8	0.725	7.31	0.685	11.9	3.6
250	45	30	8	0.723	7.34	0.684	11.6	3.6
250	50	30	8	0.726	7.12	0.676	11.6	3.5
250	70	30	8	0.726	7.54	0.675	12.0	3.7
250	90	30	8	0.730	7.78	0.681	12.7	3.9
250	100	30	8	0.728	7.78	0.664	12.9	3.8
250	120	30	8	0.723	7.69	0.669	11.2	3.7
100	70	30	8	0.726	7.61	0.679	11.5	3.7
250	70	30	8	0.729	7.69	0.676	10.9	3.8
320	70	30	8	0.734	7.77	0.671	12.1	3.8
320	70	30	6	0.724	7.79	0.671	13.9	3.8
320	70	30	8	0.734	7.77	0.671	12.1	3.8
320	70	30	10	0.728	7.65	0.674	14.0	3.8
250	90	10	8	0.726	7.78	0.674	12.7	3.8
250	90	30	8	0.729	7.78	0.681	12.7	3.9
250	90	50	8	0.732	7.69	0.678	11.2	3.8
No Added	ZnO layer	- Only	Al/thin ZnO	0.701	6.86	0.683	11.5	3.3

Table 8. Data for a-SiGe:H Cells Whose Backreflectors were Made Using Targets with Different Al Contents.

Target Material	V_{oc} (V)	J_{sc} (mA/cm^2)	FF	R_s (Ωcm^2)	P_{max} (mW/cm^2)
ZnAl (5%)	0.715	7.83	0.667	11.5	3.7
ZnAl (3%)	0.718	7.76	0.676	12.1	3.8
Zn	0.712	7.81	0.643	16.2	3.6

To truly judge the quality of the back reflectors made using the new reactive sputtering process, single-junction a-SiGe:H cells were made using three different types of back reflector listed below:

1) back reflectors made in the pilot machine under the optimized conditions using the experimental reactive sputtering process and the ZnAl(5%) sputtering targets,
2) back reflectors made in the pilot machine under the optimized conditions using the standard sputtering process and ZnO targets,
3) back reflectors made in the 5MW production machine using the standard sputtering process and ZnO targets.

Again, the nip structures for all three types of back reflectors were made in the same deposition run using United Solar's 1 sq. ft. R&D deposition system. The data for the three types of cells are listed in Table 9. Comparing data for the cells made using the back reflectors from the pilot machine, the cell properties for the cells made using the ZnAl (5%) targets are similar to those for the cells made using the ZnO targets demonstrating that the new reactive sputtering process can be used to prepare high quality back reflector material.

Table 9. Data for a-SiGe:H Cells Whose Backreflectors were Made with the Reactive Sputtering Process Using Zn Metal Targets and the Standard Process Using ZnO Targets.

Target Material	BR Machine	V_{oc} (V)	J_{sc} (mA/cm^2)	FF	Rs	P_{max} (mW/cm^2)
ZnAl(5%)	Pilot Machine	0.731	7.57	0.668	10.7	3.7
ZnO	Pilot Machine	0.731	7.49	0.665	12.0	3.6
ZnO	5MWProduction	0.730	7.42	0.662	13.2	3.6

As a final comparison of the back reflectors made with the Zn metal and ZnO targets, we have fabricated larger area (44.5 cm^2) single-junction a-SiGe:H cells using the two types of back reflectors. The nip structures for the two cells were prepared in the same deposition run in order minimize the differences from layers other than the ZnO materials. Table 10 displays data for these two types of cells. The slight differences in the properties for the two cells are within experimental error again demonstrating that the inexpensive ZnAl(5%) targets can be used to prepare high quality back reflector material. These cells fulfill the required deliverable D-1.4.9.

Table 10. Data for 44.5 cm^2 Modules Made with Different Backreflectors.

Target Material	BR Machine	J_{sc}(QE) (mA/cm^2)	V_{oc} (V)	FF	R_s (Ω/cm^2)	Efficiency (%)
ZnAl(5%)	2 MW Pilot	18.9	0.77	0.631	0.20	9.18
ZnO	5MW Production	18.5	0.77	0.649	0.18	9.24

Preparation for Tests in 5MW Production Machine

Having established that the reactive sputtering process can be used in the roll-to-roll design to make high quality ZnO layers, we are now making arrangements to fabricate a 100m long back reflector coated web to demonstrate that the process can be used to make the high quality material consistently over a long period of time, a requirement for production. At the beginning of this program, it was thought that the fabrication of the back reflector for this 100m long section of web would be done using the pilot machine. However, in order to expedite the implementation of the new sputtering process into production, we have decided to complete this test using the 5MW production equipment. In order to do this, we have made several preparation steps during this phase of the program including the purchase of six production size ZnAl (5%) targets, the changing of cathode shielding in the production machine and the purchase, at ECD's expense, a mechanical pump and blower capable of handling oxygen. We are presently waiting for the delivery of the pump and blower that is scheduled to occur in mid July. Shortly after delivery (August), we will begin depositions in the 5MW facility using the reactive sputtering process.

Plans for Phase II of the Program

In the next year, we plan to optimize the reactive sputtering process in the 5MW production plant to allow for the fabrication of a 100M long section of solar module material using the new process to prepare the ZnO layer. Since the optimized conditions in the production machine may differ from those for the pilot machine, this optimization process will include systematic variation of the Ar and O_2 flows, the web temperature and the applied power. We will also test the use of the new process to prepare the Zn material at the Al surface. Thus far, we have only used the new process after a thin ZnO layer has been deposited on the Al using the standard sputtering process and ZnO targets. Once small area cells have been fabricated using the small area equipment and the expected high efficiencies are achieved, a full scale 600M production run will be completed using the new sputtering process and all of the production equipment. This will include the deposition of triple-junction nip structures using the 5MW deposition machine. Using this material, standard QA/QC coupons will be fabricated and the sub-cells quality compared with that for the standard production sub-cells made using the standard sputtering process.

Task 4 - Cathode Hardware Studies for a-Si(Ge):H i-layer Depositions

Background

Efficiencies for small area a-Si:H based devices are being steadily increased; the present world record is 13% stable efficiency for a small area triple-junction cell (0.25 cm^2 active area) produced in a small scale reactor (4” x 4” maximum deposition area) by United Solar. This accelerating improvement suggests that even higher efficiencies should be obtainable. However, the efficiencies obtained for large area solar modules are still significantly lower than the 13% values being near 8-9%. The lower module efficiencies are due in part to back end processes such as lamination and module designs. However, even the small area cells fabricated in the large area, continuous roll-to-roll machines (in particular the 5 MW machine) have yet to demonstrate efficiencies that match the world record values even though thorough optimization studies have been carried out. This suggests that there are inherent problems with the present large area process and/or hardware designs that limit the efficiencies to their present day values.

One problem which is more difficult to achieve in the present large area production machines as compared with the smaller R&D machines is the ability to prepare reasonably uniform film depositions across the entire cathode area during PECVD depositions. This problem was of major concern during our optimization program for the 5 MW production machine. For example, a-SiGe:H i-layer depositions, in order to obtain relatively uniform film depositions across the length of the cathodes for each vacuum chamber, we were limited to work in a small area of deposition parameter space. If parameters outside this space were used, gradients across the length of the cathode were obtained for the Ge content as well as for the deposition rate as is shown in Figure 29 It was found that these non-uniformities were not related to unequal power distributions across the cathode or gas depletion, as one might expect. With a moving web substrate, this affect lead to cells and modules which had significant variations in the Ge content through the depth profile of the a-SiGe:H i-layers. Variations in the bandgap of the materials obviously accompanied the Ge content fluctuations that likely formed shallow carrier traps in the i-layers limiting the carrier collection and cell efficiencies. Also, since the quality of a-Si:H based materials prepared by the PECVD method depend strongly on the film deposition rates, the variations in the deposition rates led to the formation of high quality material in the region of the cathode where the deposition rates were low and poorer quality material in the region where the deposition rates were high. Under these conditions, the overall film and device performance was limited by the poor material produced in the high deposition rate region. If the overall deposition rate were lowered in order to improve the material produced in the high deposition rate region, the machine throughput was unacceptably low.

We should note that similar variations in the deposition rates across the lengths of the cathode were also observed for a-Si:H layers. Thus the non-uniformity problem was not related to differences in the decomposition rates of Si and Ge source gases but instead is inherent to the existing vacuum hardware design.

When limited to a small region of parameter space, the efficiencies are likely limited to low values. With a different internal hardware design that allows for uniform depositions across a large area of parameter space, the maximum efficiency would likely be outside the small area of parameter space we are presently restricted to. Thus, if such a deposition hardware design could be devised, higher cell and module efficiencies would likely be obtained.

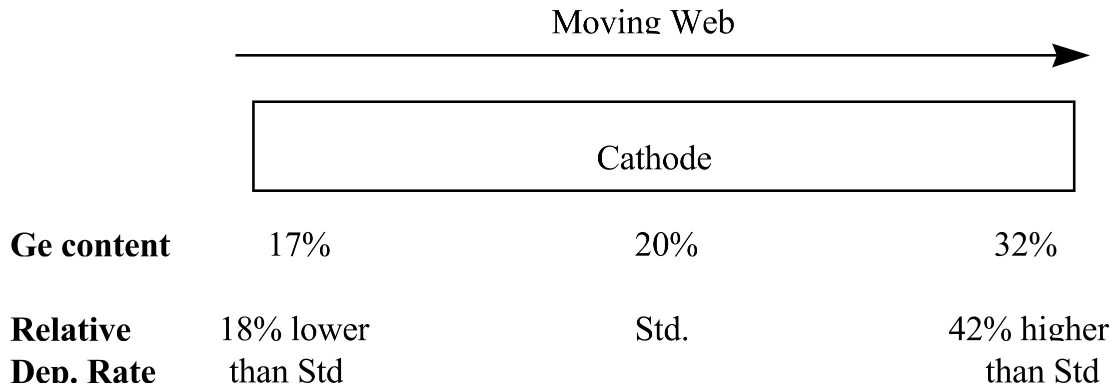

Figure 29. Variation of Ge content and deposition rate across cathode.

In attempting to achieve the record high efficiencies using the large machines, one must be assured that the film growth conditions used to prepare the large modules are similar to those obtained using the small area machines. In particular, the plasma chemistry, electrical potentials and film surface growth conditions must be duplicated in order to prepare the proper film quality and film microstructure. Specifically, a deposition system which comes close to replicating the plasma densities for all of the Si based radicals and H atoms in the plasma, the substrate self bias and the plasma potential, and the electron and ion bombardment of the growth surface must be designed. Only when this is done will one have the potential of achieving the high efficiencies with the large area systems. While the present internal hardware design for the 5MW chambers is not dramatically different from the design for the small scale systems used to prepare the high efficiency cells, a design for the large area chamber internal hardware which more accurately reproduces the small scale geometry might lead to higher large area cell efficiencies.

Objective of Cathode Hardware Studies

In this program, we will develop new internal hardware for the i-layer deposition chambers used in United Solar's 5MW production line in order to improve the quality and uniformity of these materials to increase the overall solar cell and machine efficiencies. Three newly designed cathodes will be built, tested and compared with the 5MW design during this three year program. To judge the usefulness of each design, single-layers are being made to test the ability to obtain uniform deposits over large areas and large regions of deposition parameter space while single-junction a-Si:H cells are being fabricated to test the quality of the deposited layers. Each design is first tested in a single chamber system with a static substrate.

Once final designs for the internal hardware are completed, the hardware is to be incorporated into an existing chamber on the 2 MW pilot semiconductor line at United Solar (see Figure 30). To test this new internal hardware, single-junction nip a-Si:H cells will be prepared using the new hardware on a moving web substrate. The i-layer conditions will be optimized for the highest FF for cells with similar J_{sc} values. Improvements in the hardware will be judged by increased FF for the cells and improved deposition uniformity over those obtained with the 5MW style cathodes. If necessary, alterations to the system hardware will be made so that the plasma and growth conditions more closely match those for the small area R&D system. Also, temperature, gas flow and pressure distributions throughout the chamber will be closely monitored. If it is demonstrated that this new design is an improvement over the presently used design, we will incorporate the new chamber design into the 5MW production line.

Figure 30. Double-junction roll-to-roll plasma-CVD processor, previously used as United Solar's production machine. This machine will be used as an experimental machine for much of the work proposed in Tasks 1 and 4.

This roll-to-roll PECVD processor was used as a solar cell production machine when United Solar's production plant had a capacity of 2 MW. It is capable of making nipnip tandem solar cell structures on a 14" web. The i-layer cathode lengths vary from 17" to 56" long.

Experimental

Thus far, we have developed three new cathode designs and have tested one design with the testing of two others in the later stages of the program. The new designs will incorporate several ideas that were devised during the 5MW machine optimization program, during which a great deal of knowledge was obtained. Further studies of the 5MW cathode design in this program has also proved beneficial towards the development of this new hardware. Incorporation of several improvements should lead to better control of the gas flow, temperature distribution and film uniformity across the cathode and deposition area.

Initial tests of the cathodes are being completed using a single test deposition chamber (see Figure 31) in which two different styles of cathodes can simultaneously be compared in the same environment. During this first year, we designed, built and compared one new cathode design with a cathode that mimics the design used in 5MW production machine. In the same system pump-down, single layer films to test deposition uniformity and/or i-layers for nip solar cells to test i-layer quality were made from both types of cathodes.

Typically, the same deposition conditions were used for both deposits including the same rf power density. For the single layer deposits on bare stainless steel substrates, film thickness across the deposition area was measured using standard optical techniques. The 13.56 MHz Plasma Enhanced Chemical Vapor Deposition (PECVD) technique is being used to deposit all of the materials.

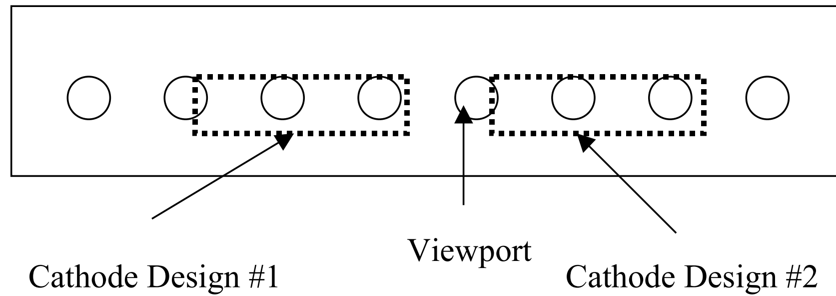

Figure 31. Single chamber system used for cathode development.

To fabricate 0.25 cm^2 a-Si:H single-junction test cells, the cathode hardware to be tested is only being used to prepare the i-layer materials. Preparation of both the intrinsic layer and the doped layers in a single chamber system is not desirable because of the cross contamination effects which hinder electron and hole collection in the cell. Therefore to make the cells for this study using the single chamber system, we are making the n- and p-layers by the PECVD method in a separate, proven load lock R&D system. This system has prepared high efficiency triple-junction devices in the past and is presently used to make high efficiency single junction cells. The steps we will use to prepare each of the devices are as follows:

1) deposit an a-Si:H:P n-layer using the load lock system,
2) quickly transport the n-layer coated substrates to the single chamber system attempting to minimize air exposure,
3) deposit i-layers using the two different cathode designs,
4) quickly transport the n/i coated substrates from the single chamber system to the load lock system again attempting to minimize air exposure,
5) deposit an a-Si:H:B p-layer using the load lock system,
6) deposit ITO/Al contacts using standard evaporation techniques.

Such a device is depicted in Figure 32. For these studies, we will focus on cells made without current enhancing Ag/ZnO backreflectors to minimize the complexity of the cells.

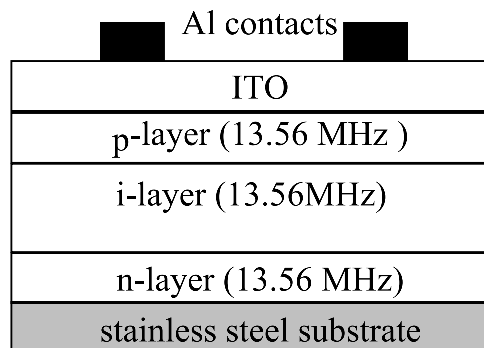

Figure 32. a-Si:H single-junction cell structure.

In the pilot machine, all three semiconductor layers (n-, i- and p-layers) are being deposited in the roll-to-roll process. Again, these layer are being deposited on bare stainless steel substrates. ITO contacts are deposited using a dc sputtering technique and a 1 sq. ft. R&D machine while Al contacts are evaporated onto the ITO using a small scale reactor.

To characterize the devices, current vs. voltage (IV) measurements are made to obtain standard solar cell device parameters (short circuit current (J_{sc}), Fill Factor (FF), Open Circuit Voltage (V_{oc}), etc.). Also, quantum efficiency measurements are also used to obtain integrated currents and determine collection losses in cell.

After initial cell measurements, the devices are being subjected to light soaking periods. We are first light soaking the samples for 10 and 30 hrs. under AM1.5 light at 50°C, after each of these periods measuring the cell properties. To measure the stable efficiencies, one must light soak them for 600 hrs. But to get preliminary data on how the deposition parameters are affecting the amount of degradation, we are making these limited light exposure measurements to optimize the deposition conditions for minimum degradation and optimum stable cell efficiencies. After initial screen testing, we are selecting certain cells for long term light exposures to obtain accurate values for the stable efficiencies.

Results of Work Completed During Phase I of the Program

The 5MW Style Cathode in the Single R&D Chamber

Testing Similarity to Cathodes Used in Production

Initially, several depositions were completed to verify that the 5MW style cathode in the single R&D cathode testing chamber behaved similar to the cathodes in the 5MW production machine. In particular, we were testing to see if the non-uniform deposits across the length of the cathode would be obtained at the production level deposition rates. Figure 33 compares deposition rate profiles across the length of the cathode obtained using different deposition conditions and the 5MW style cathode. These profiles were taken near the center of the deposit and the cathode as is shown in Figure 34. In Figure 33, we compare profiles taken at different applied power levels that led to different deposition rates while all other deposition parameters were nominally fixed. The average deposition rates in Å/s for each profile is listed in the figure legend in brackets. As is the case for the production line cathodes, as the power level is increased, the film thickness, and thus the deposition rate, near the gas inlet becomes much larger than the thicknesses obtained near the pump out port. This variation in deposition rate across the cathode length is partially due to a gas depletion effect but can not be the only cause due to the fact that there is not a drop in deposition rate near the pump out side of the cathode as the power is increased. This trend of poorer uniformity with increased power was the same effect observed during the optimization of the 5MW production line.

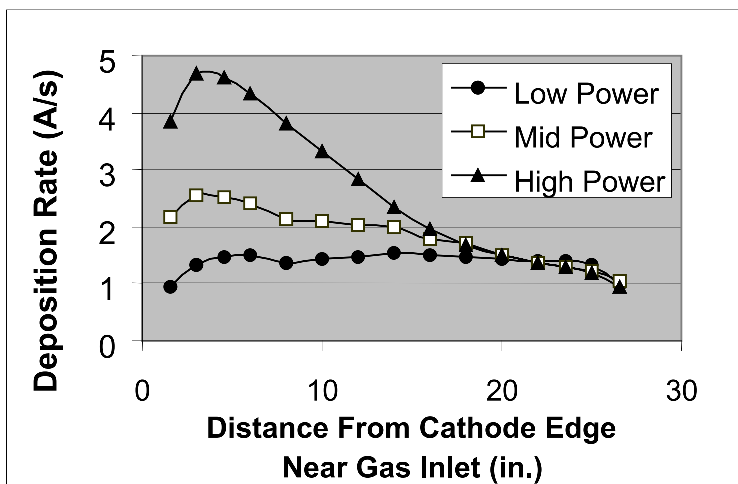

Figure 33. Thickness profiles for films made at different applied rf powers.

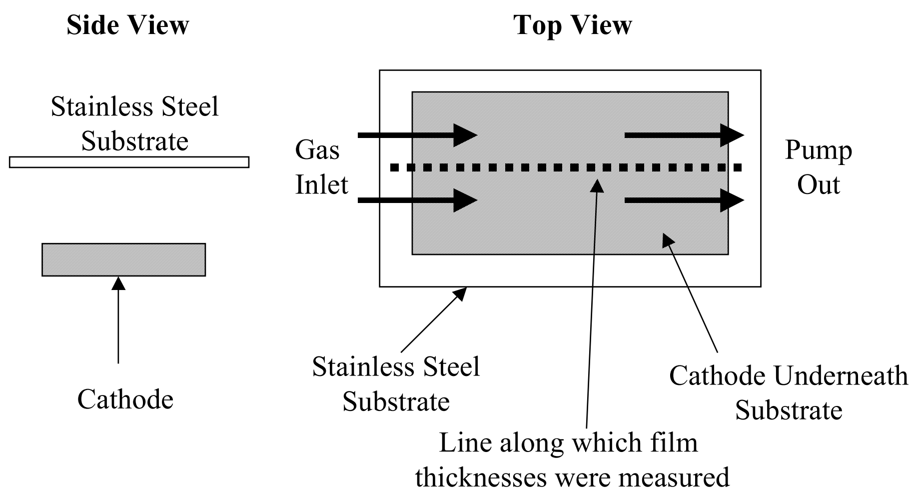

Figure 34. Orientation of film thickness measurements.

In these studies, it became obvious that the uniformity of the deposit across the cathode length was primarily dictated by the applied power level as it was for the cathodes in the production line. Figure 35 displays the degree of uniformity across the length of the cathode as a function of deposition rate. As a figure of merit for the film uniformity, the y axis in this figure denotes the difference between the maximum and minimum deposition rates obtained across the length across the cathode divided the average deposition rate for the deposit. The differences in applied power are denoted by the different icons. As can be seen from the figure, at each fixed power level, the degree on uniformity remains relatively unchanged while other deposition parameters including the hydrogen flow, the active gas flow (silane), and the substrate temperature were altered changing the deposition rate. In contrast, the uniformity becomes poorer with increased the power.

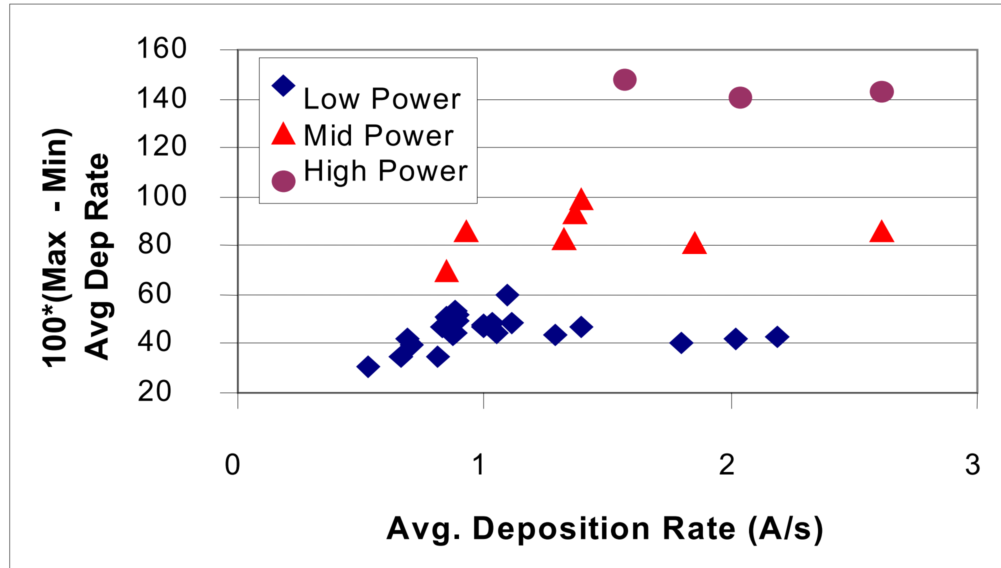

Figure 35. Variation of deposition uniformity over length of cathode as a function of deposition rate.

From the data in Figure 35, one can observe that fairly uniform deposits and relatively high deposition rates (greater than 2 Å/s) can be obtained at low power levels (80-120W). However to achieve these rates, low hydrogen dilution levels and high silane flows had to be used which led to polysilicon powder formation on the cathode leading to poor cell performance. This is shown in Table 11 where data for a-Si:H cells whose i-layers were made at the same rates but different applied powers are compared. The cell whose i-layer was made using the low power and less hydrogen dilution has significantly poorer FF and solar cell efficiency (P_{max}). Thus the poor cell performance eliminates the possibility of using the low power/low dilution conditions to obtain good deposition uniformity.

Table 11. Data for a-Si:H cells made at different applied powers but similar i-layer deposition rates.

Power (W)	i-layer Dep. Rate (Å/s)	V_{oc} (V)	J_{sc} (mA/cm^2)	FF	R_s (Ωcm^2)	P_{max} (mW/cm^2)
120	1.80	0.949	10.93	0.577	16.7	5.99
180	1.85	0.928	10.61	0.659	9.9	6.49

From the these results, it was clear us that in terms of deposition uniformity across the length of the cathode, this cathode behaves similarly to the cathodes in production in that at increased deposition rates, the deposits are either non-uniform or of poor quality.

Attempts to Improve Uniformity Using 5 MW Style Cathode

In an attempt to better understand the causes for the non-uniform deposits at high rates, slight alterations to the 5MW cathode design were studied. In one case, we altered the pumping manifold to see if the pumping geometry would strongly affect the deposition uniformity. In particular, it was thought that the uniformity across the width of the substrate (cathode) could be improved through an alteration of the gas flow pattern. After four alterations to the pumping manifold, no significant change in the uniformity was observed.

In terms of the uniformity across the width, it was also discovered in these studies that excess hydrogen gas from a source outside the cathode hardware and gas manifold, such as from our proprietary gate gates, does significantly affect the deposition uniformity. This is demonstrated by the data shown in Figure 36 where the deposition rate profiles across the width of the cathode is shown for different outside gas flows. Comparing the profile when hydrogen gas flowed with the profile when no outside gas flowed, there is a significant drop off in the deposition rate and thus the film thickness when hydrogen gas flowed. The thinner films lead to lower efficiencies for the subcells on the edges of the film and for the 12” wide modules. However, by adding a small amount of silane to the outside hydrogen gas flow, one can once again obtain the desired uniformity across the web as is shown in the figure. This result can immediately be applied to the 5MW production line, in particular to the gas gate flows, to improve the deposition uniformity across the width of the web.

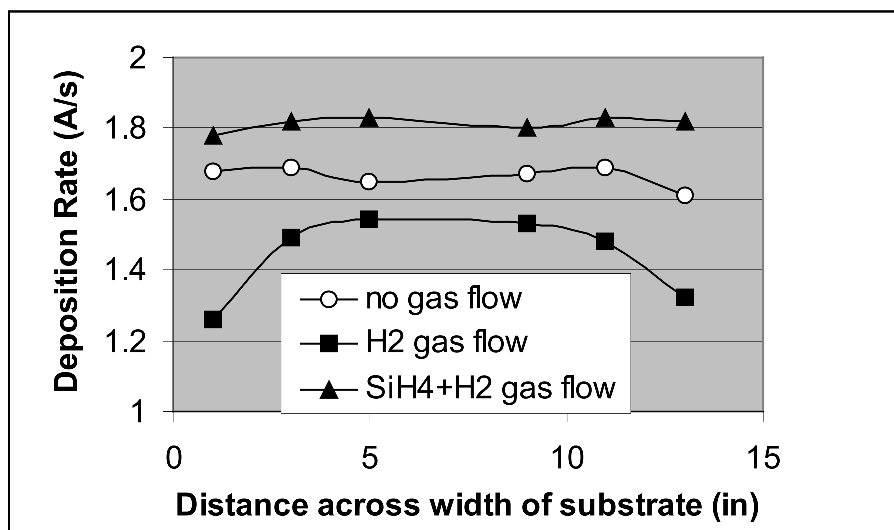

Figure 36. Uniformity across width of web (cathode) from deposits made using different gas flows from outside cathode and gas manifold hardware.

Use of pulsed rf plasmas was also tested as a method to improve the deposition uniformity across the length of the cathode. It was thought that by using short, high decomposition rate pulses, one would minimize radical interaction that may be a chief cause for the non-uniform deposits at high rates. Several experiments were completed using different duty cycles, pulse widths, and no-pulse power levels. In each case, more uniform deposits but lower deposition rates were obtained when the pulsed plasma was used instead of the continuous constant power conditions. Also, powder formed on the cathode each time a pulsed plasma was used leading to lower cell efficiencies. The source of this powder is not yet understood. Alteration of the gas flows and applied powers to match the deposition rates obtained using the continuous power conditions led to increased powder formation. Thus, use of pulsed power is not the answer to obtaining uniform deposits and we have still yet to find a method to obtain uniform deposits across the length of the cathode using the 5MW production hardware.

Testing of New Cathode Design in the Single R&D Chamber

One new cathode design has been thoroughly tested in the single chamber cathode testing system along with the 5MW style cathode. For each system pump down, separate deposits were made using both cathodes under similar gas flow conditions, substrate and cathode temperatures, power densities and chamber pressures. This new cathode has several features which mimic those for cathodes used in R&D which produce cells of high efficiencies. In particular, this new cathode differs from the 5MW style

cathode in terms of gas flow pattern and electrical potentials obtained during deposition, including the substrate self bias.

A number of deposits were made using both types of cathodes with the following deposition conditions varied; the substrate temperature, the cathode temperature, the applied rf power, and the silane and hydrogen gas flows. For each deposit, a large substrate was used for characterization of the deposition uniformity while 2"x2" n-layer coated substrates were also included for cell preparation and judgement of the i-layer quality.

It was found that with this new design, one could obtain uniform deposits (±8%) over the entire cathode area at a wide range of deposition rates (1-5 Å/s) using a number of different deposition conditions. Figure 37 displays uniformity profiles across the center of the cathode hardware for typical low rate and high rate deposition condition. One should note that the new cathode is roughly half as long as the 5MW cathode design. However, our engineers and scientists have determined prior to the construction of this cathode that because of the cathode's unique design, expansion of the cathode to twice it's present size will not cause a significant alteration of the deposition profile. The ability to obtain good uniformity over this relatively wide range of deposition rates is likely associated with the different gas distribution system from the 5MW cathode design. This is a significant improvement over the production style cathode.

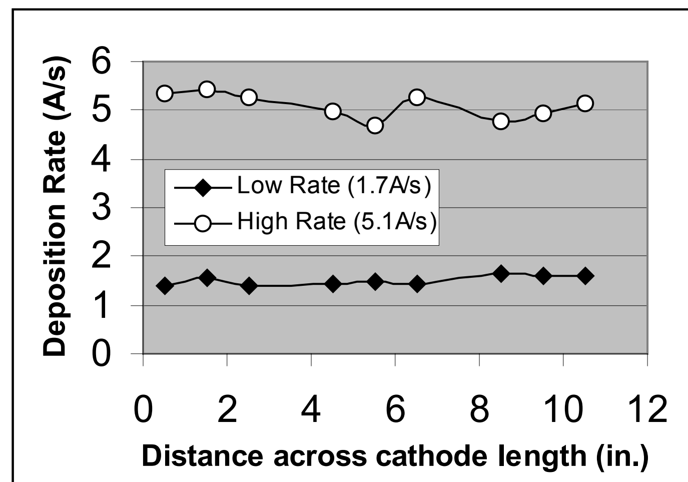

Figure 37. Deposition rate profiles across new cathode at different deposition rates.

In terms of i-layer quality, a number of cells were made as can be seen from the data shown in Figures 38 and 39. In the figures, the fill factor (FF) and maximum power (P_{max}), or cell efficiency, are plotted as a function of short circuit current. Both the fill factor and the cell efficiency depend strongly on the i-layer thickness. For these a-Si:H cells, the short circuit current depends almost linearly with film thickness in the range of J_{sc} studied. Thus, the figures roughly contain the trends of FF and P_{max} with i-layer thickness. To compare cells in this case i-layer quality, one should compare cells with the same i-layer quality and thus the same J_{sc} value. Of course during optimization of the deposition conditions, most of the cells were not made under the optimal conditions (the solid circles in the figures). For both types of cathodes, it was determined that i-layers made with high hydrogen dilution of the plasma and a substrate temperature of 225 ºC had, on average, the best cell properties. In the figures, the data for these cells are denoted by open triangles and open circles for the new and 5MW style cathodes, respectively. Under these conditions, the cells made using the new cathode had significantly poorer performance than the cells made using the standard 5MW cathode due to lower FF. This can be seen more clearly from the data shown in Table 12 where values for cells with similar i-layer thicknesses made under the optimal

conditions are compared. The disparity in cell performance becomes even larger as the deposition rate is increased.

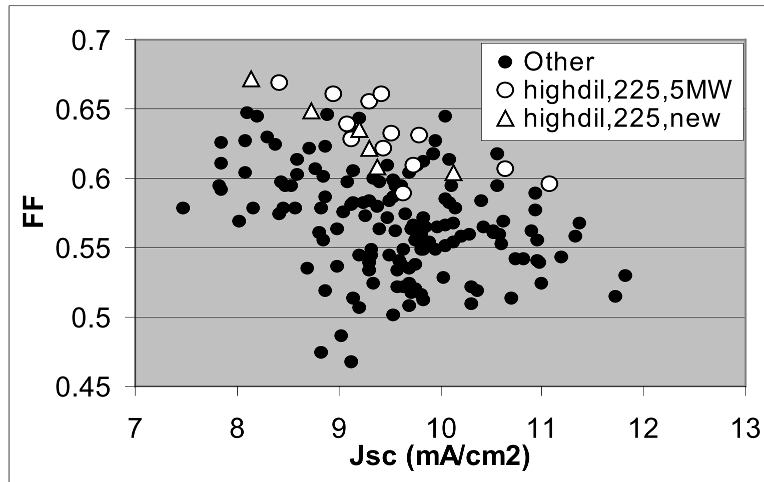

Figure 38. Plot of fill factor versus short circuit current for cells made using the new and 5 MW style cathodes.

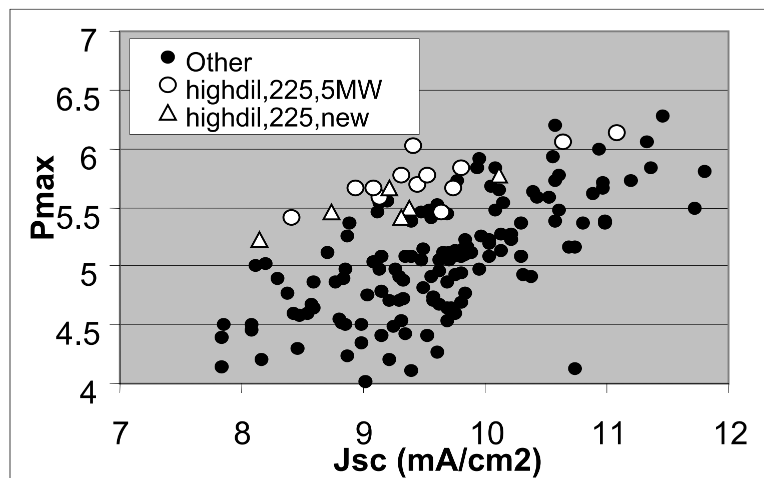

Figure 39. Plot of efficiency versus short circuit current for cells made using the new and 5 MW style cathodes.

Table 12. Data for a-Si:H Cells Made Using the New and the 5 MW Style Cathodes.

Cathode Design	i-layer thickness (Å)	Deposition Rate (Å/s)	V_{oc} (V)	J_{sc} (mA/cm^2)	FF	R_s (Ωcm^2)	**P_{max} (mW/cm^2)**
New	1800	1.0	0.956	10.05	0.585	21	**5.62**
5MW	1730	0.96	0.943	10.08	0.614	20.5	**5.84**
New	2250	1.9	0.944	10.53	0.561	14.8	**5.58**
5MW	2100	1.8	0.949	10.57	0.618	11.8	**6.20**

There are several possible reasons for these poorer properties for the cells made using the new cathode design. As mentioned before, both the gas flow pattern and the electrical potentials related to the plasma

are different in this new design. While the flow pattern and the potentials set up by the plasma can affect the i-layer quality, previous experience with different deposition reactors suggests that in this case, the different gas flow pattern in not likely the cause. Instead, we believe the electrical configuration is more suspect. It was also observed that powder formation occurred more easily in this cathode configuration than with the 5MW style. Build-up of this porous powder material can lead to absorption of water vapor during venting and air exposure of the deposition system. This water vapor can later lead to oxygen incorporation in the i-layers and poor cell performance. This increased powder formation could be a result of the gas flow pattern or the electrical configuration. If this is the case, this may be a signal that the plasma associated with the new design contains more complicated Si based radicals which lead to the formation of polysilicon chains. However, we believe that it is for the most part related to complicated design which leads to the exposure of colder surfaces to depositing species.

The experience gained during the study of this first new cathode design has led to the engineering of a second configuration. This design has a similar gas flow pattern to the first new design and thus we expect the deposition uniformity will be as equally good. Electrically and geometrically, this second design is more similar to the 5MW design and, thus, the cell properties and the i-layer quality should be improved over the first new design. This design has recently been built and will be installed into the cathode testing system during the early part of phase 2 of the program.

Establishment of Baseline "5MW-like" Cathode in Roll-to-Roll Pilot Machine

During this period of the program, we have also begun work for testing of the new cathode designs in the roll-to-roll pilot system for the moving web testing. This machine is equipped with cathodes similar to those used in the 5MW production machine and initially these cathodes will be used to set a baseline for the machine. This machine has not been in use for over three years and was thus in need of several repairs. A list of some of the repairs completed during this reporting period are listed below:

- Servicing and repair of five rf power supplies
- Installation of a complete new pressure monitoring system
- Full repair of the web drive system
- Repair of eight heating controls
- Reconfiguration of the gas handling system
- Extensive repair of the gas scrubber system
- Extensive repair of three of the five mechanical pumps
- Installation of a new nitrogen purge system for the exhaust gases
- Repair of a number of safety interlocks
- Complete replacement of the exhaust manifold for the mechanical pumps
- Complete replacement of Ar o-ring purge lines

The list was much more extensive then we initially thought when the program started. However, completion of the repairs was done at the end of this first phase of the program. Setting the baseline for the machine will begin at the beginning of phase 2 of the program.

Plans for Phase II of the Program

In the next year, we will focus on developing a second new style of cathode. This style has a gas flow pattern similar to the cathode first tested, but electrostatically similar to the 5MW style cathode. Eliminating the difference in electronic potentials between the new style cathode and the 5MW style cathode should lead to cell efficiencies similar to those obtained with the 5MW cathode. The improved deposition uniformity should come with the use of a different gas flow pattern from the 5MW style

cathode. The hardware for this cathode has been made and installation into the cathode testing single chamber should begin shortly. Thorough testing will be made of the deposition uniformity and i-layer material quality through systematic variation of a number of deposition parameters.

Final preparations of the roll-to-roll pilot machine have just recently been completed and plans for deposition runs in the month of July are now being made. The first set of runs will be made using the 5MW style cathode to set a baseline with a new cathode design tested soon after.

Modeling for Amorphous Silicon Deposition

Introduction

In the first year of this program the major accomplishment was to convert a Boltzmann code, previously developed for simulating diamond deposition, chlorine etching, and oxygen ashing in plasma reactors, to a code appropriate for modeling the plasma assisted deposition of amorphous silicon. An important component of this involved determining which neutral and ion gas species are needed to accurately simulate the gas chemistry. In addition, a crude model, appropriate for a one-point code, was incorporated to model diffusion to the walls and silicon deposition. The code was then debugged and run using conditions appropriate to a specific reactor run and the predictions of the code were compared to data. Comparisons with the thickness of the deposition at the center of the substrate showed good agreement. As a one-point code this simulation is incapable of showing either the effects of sheaths, and hence ions, at the walls or the effects of non-uniformity in the electric field, which can lead to non-uniformity in the deposition. To begin to address these issues we also adapted a 1D RF code to this problem and this code has been tested. Now that the Boltzmann code has been validated against data it will be run for a variety of electric field parametric values to generate a table of electron energy distributions and neutral densities appropriate to each value of the local electric field. These tabular values will be inserted in the RF code to generate predictions of sheath structure and ion dynamics. When this code is validated a 2D version will be constructed to more accurately account for neutral diffusion effects. These tools will provide a reliable means of simulating the major physical effects in the reactor.

Simulation Strategy

Simulating an RF system involves an analysis of local and global phenomena. In the pressure regime appropriate for the ECD reactor, these phenomena de-couple. On the global level we can write continuity equations for electron, ion, and neutral species particles and momentum. These equations treat each species as a fluid and do not solve for the velocity space distribution functions of the species. The continuity and momentum equations for each species would be an exact description of the system if we knew the pressure tensor. This however involves solving an unending chain of higher order moment equations. Fortunately, for the case at hand we are able to make simple and accurate assumptions as to the form of the pressure tensor for each species in terms of the species density.

The continuity equation for the electron and ion momenta requires a knowledge of the electric field distribution, which for this frequency range can be derived from the electrostatic potential. The potential is obtained by solving Poisson's equation given the electron and ion densities. Thus far all of the quantities required are global quantities, which involve solving equations on the scale of the reactor. However, the solution of the various continuity equations depends on local processes as well. Some of these involve neutral kinetics: neutral species A and B interact to form neutral species C and D. Others involve electron mediated processes: an electron impacts molecule A and produces molecules B and C, or an electron impacts species A and knocks off an electron producing an electron- ion pair.

While the neutral-neutral interactions can be obtained from kinetic rate information, calculating the electron rates for electron-neutral processes involves solving for the electron distribution function. The solution depends on the value of the electric field during the entire history of the particle. In low pressure systems this requires a global solution since electrons at one point may have been heated by electric fields at another spatial point at and earlier time. At the higher pressure of the ECD reactor, electrons move only a short distance in space during a typical heating time due to the short mean free path. Therefore the electron energy distribution function depends only on the local value of the RF electric field: an enormous simplification. This permits us to solve for the electron rates as a function of the local electric field at each point in space and then to use these rates in the various continuity equations. These continuity equations then advance the electron and ion densities, which produce a new global electric field that can then be used to recalculate the electron rates. Thus the simulation strategy is now complete. We discuss below further details of the solution method for the electron distribution function and describe how this local analysis can be used to approximate the entire reactor.

Solution of the electron energy distribution function - As described above the short mean free path permits a local solution of the electron energy distribution function. It also produces to lowest order an isotropic velocity distribution function with a higher order distortion in the direction of the electric field. This is the physical basis behind the ``two term expansion'' model of the Boltzmann equation, which is used to obtain the isotropic portion of the electron energy distribution function. The numerical solution to this model is referred to below as the Boltzmann code. However, the numerical solution of even this highly simplified model Boltzmann equation is time consuming and it is computationally tedious to solve this equation at every spatial point in the simulation. We therefore use the Boltzmann equation to fit the electron rates to an analytic function of the local electric field and then use this analytic function in the global solution for the fields.

One-Point Simulations

Although the Boltzmann code calculates the electron distribution function at a single point in space we can use it to investigate the chemistry of the entire reactor by simplifying the global continuity equations. In this model we write equations for the time dependence of globally averaged number densities of electrons, ions and neutrals. The local production and loss terms for each species are calculated as in a full global model, but the spatial loss rates such as convection or diffusion to the reactor walls are included parametrically as decay times for each specie. The electron-neutral rates however require a knowledge of the local electric field, which we do not know since we are only solving a one point problem. We obtain an estimate of the local electric field by requiring that the local power deposition have a particular value. At any moment we know the average electron density and we can compute the energy loss rate by electrons to neutrals for a given electric field. We adjust the local electric field to give the desired local power deposition. This approximation assumes that most of the RF power deposited is lost by electron-neutral inelastic collisions rather than into accelerating ions. In order to obtain a better estimate of this energy a 1D or 2D global solution is required to estimate the average RF sheath. This will be done in the coming weeks.

RF-Global Simulation

The field distribution within the reactor is the result of the applied potentials to the various metal surfaces within the reactor and the charged particle space charge densities. These charged particle densities in turn are affected by the electric fields. Specifically, electrons move rapidly in such a way as to screen out the electric field within the core of the plasma. Thus a combined solution of the electron and ion continuity equations together with Poisson's equation is required. There is a wide discrepancy in the time scales for the various processes, however. Electrons respond to an applied electric field on the plasma time scale, the fastest time scale in the process, typically much faster than an RF period. Ions however respond on a

much slower time scale, typically comparable to the RF frequency. They move through the core of the plasma on a time scale given by the inverse of the ion sound speed divided by the reactor plate separation. This time scale is typically several RF periods. The ion dynamics in the RF sheath can be complex since the ion sheath crossing time can either be fast or slow compared to the RF frequency. For applications in which the ion distribution function striking the powered electrode is crucial, this needs to be resolved accurately. For our purposes we can approximate the ions as falling through an RF averaged potential.

The solution of the electron dynamics can be approached at various levels of the approximation. In the RF code being used for this project the primitive electron momentum equation is solved. It is also possible to use a drift-diffusion approximation in which the inertial term in the electron momentum equation is neglected. Each solution method has its advantages and disadvantages.

It is useful at this point to review some of the main physical processes in an RF plasma since they help to set in context the one-point Boltzmann calculations that have been done thus far. If the ion mass is sufficiently heavy, ions that are created in the plasma core fall towards the powered and grounded electrodes. This outward motion to the walls is sped up by an electrostatic field that hinders electrons from escaping at the much faster rate that would be determined by their diffusion to the walls in the absence of electric fields. The ion and electron loss rates must be very closely matched or a large charge imbalance will occur in the calculation leading to large electric fields that inhibit the escape of the faster species. Thus within the plasma core there is a potential structure set up by the requirement of equilibrating electron and ion losses. This potential structure, which is concave downward would exist even if there is no RF voltage applied to the electrodes.

In an RF plasma one of the electrodes is driven sinusoidally. As this electrode goes negative it pushes electrons back into the plasma core producing an RF sheath. These electrons move through the core of the plasma and are deposited in the sheaths at the grounded surfaces reducing the width of these sheaths and hence their potential height. The movement of the electrons from the driven electrode sheath through the plasma core to the ground sheath is driven by an electric field that is superimposed on the ambipolar field structure, and which is hindered by collisions between the electrons and neutrals. This combination of an electric field that pushes electrons and collisions with neutrals, which randomize the directed velocity given to the electrons by the field, is what produces electron heating. It is in fact this electric field which will be used in the Boltzmann equation and which will return the electron rates and the average electron energy.

In the pressure regime of interest this is the primary heating mechanism for electrons. At lower pressures where the electron mean free path is larger than the plate separation, the interactions between the electrons and the moving sheaths must be taken into account. This is not yet a solved problem and we are fortunately able to neglect heating due to the sheath movement in this pressure regime.

In the RF code that will be used for this project, the primitive electron momentum balance equation is advanced in time. The short time step requirement that this introduces is relaxed by using an implicit solution for the fields. The RF code will generate the local electric field at every spatial point and also the electron currents. The electron currents will then be used to deduce the residual electric field; this is then used to calculate the electron rates using analytic fits to solutions of the Boltzmann code.

The Boltzmann Code

The primary purpose of the Boltzmann code is to calculate the electron energy distribution function for different spatial locations in the reactor, associated with different values of the electric field strength. The distribution will be determined by the electric field strength and the electron cross sections of the

dominant gas species. The input gas species are hydrogen (H_2) and silane (SiH_4). The electron energy distribution determines the rate of all electron processes including ionization, dissociation, vibrational heating, etc. To calculate the rates requires knowledge of these basic cross sections. Once the rates are established and applied, chemical radicals and ions are generated and neutral and ion chemistry ensues, usually coming to steady state equilibrium in times of the order of milliseconds to tens of milliseconds. The species also diffuse to the walls and substrate. In particular, in the reactor it is the radical SiH_3 that diffuses to the substrate and is deposited, leading to the amorphous silicon deposition.

A. *Chemistry Model* – The chemical species consist of neutrals, positive ions, negative ions, and electrons. We use a fairly large set, among which there are many that will exhibit very small concentrations. It might be thought that these could be disposed of to simplify the chemistry. This is not always the case, however. A species may have a small concentration resulting from a high production rate balanced by a high loss rate. The loss rate may be producing a more stable specie that could not be formed without the precursor specie. In other cases, in retrospect, some perhaps could be omitted. The model species are as follows:

Neutrals –	H_2, SiH_4, H, SiH_3, Si_2H_6, SiH_2, SiH, Si, Si_2H_5, Si_2H_4, Si_2H_3, Si_2H_2, Si_2H, Si_2, Si_3H_5, and Si_3H_8. Also, integrated are the first and second vibrational levels of hydrogen, $H_2(v=1)$ and $H_2(v=2)$.
Positive Ions -	H^+, H_2^+, H_3^+, SiH_3^+, SiH_2^+, SiH^+, $Si_2H_7^+$, $Si_2H_5^+$, $Si_2H_4^+$, $Si_2H_3^+$, $Si_2H_2^+$, Si_2H^+, $Si_3H_7^+$, $Si_3H_6^+$, $Si_3H_5^+$, and $Si_3H_4^+$.
Negative Ions -	H^-, SiH_3^-, $Si_2H_5^-$, and $Si_3H_7^-$.
Electrons -	e^-.

As we have stated, electron cross sections are needed to calculate the electron distribution function and the electron rates. The code carries 37 cross sections for this purpose, including those for H_2, SiH_4, H, SiH_3, and Si_2H_6. Figures 40a., b., c., d., e., f., and g. exhibit a selection of these cross sections.

B. *Boltzmann Simulation* – As outlined above, we are performing a one-point calculation. This requires us to approximate the diffusion of species to the wall and the effect at the wall, whether reflection or sticking. Fortunately, there is a fairly complete experimental measurement set for the sticking coefficients of the various radicals. Incorporating these coefficients generates a gradient in each specie density approaching the wall, which is used to estimate the diffusion rate through hydrogen of that specie to the wall. This is then used in the code to decrease (or increase) each specie density appropriately to approximately account for diffusion effects.

In addition, if we need to run the chemistry for perhaps as long as a few hundredths of a second to reach equilibrium we need to determine if a molecule of hydrogen or silane will remain within the plasma long enough for the radicals to reach equilibrium. Therefore, we calculate the residence time of molecules in the reactor. Figure 41 is a schematic of the reactor we are modeling. The reactor parameters are:

pressure = 1 Torr,
gas temperature, T_g, = 250 C = 523 K,
gas flow rate, F, is 1050 sccm of H_2 and 50 sccm of SiH_4, which implies a total of 1100 sccm.

From the figure, the cross sectional area for the flow is 17.16 in. x 1.5 in., which in centimeters gives an area, A, of 166.1 cm^2. Then the flow velocity, u, in cm/s is

$$u = (0.046)F(sccm)T_g/(A(cm^2)/p(Torr)$$

The constant 0.046 = 760/273/60 is needed to reconcile the units. Putting in the numbers gives a velocity of 159.3 cm/s. Thus if y is the length of the reactor (17.16 in.), the residence time, R, is

$$R = y/u = 0.27 \text{ s}.$$

Therefore, the molecules will be in the plasma long enough for the chemistry to come to steady state equilibrium.

The conditions for the simulation include a power source of 85 watts. For this one-point calculation we assume the plasma is uniformly distributed, so we divide by the volume to get the power per unit volume at any point in the reactor. We take the H_2 fraction to be 95.45% and the SiH_4 to be 4.55%, which gives initial densities of $H_2 = 1.76 \times 10^{16}$ cm^{-3} and $SiH_4 = 8.40 \times 10^{14}$ cm^{-3}.

Simulation Results – The simulation was run initially to 0.01 s. Upon plotting the results it was unclear if the critical radical, SiH_3, had reached equilibrium. Therefore, we reran the code, this time to 0.03 s, and replotted SiH_3. Thus, all the plots we show are out to 0.01 s except the one that includes the SiH_3, which is plotted to 0.03 s. We show, first, plots of the electron distribution function as a function of energy at different times after plasma turn-on, then plots of the neutral species, positive ions, negative ions, and electrons. Finally, we calculate, based on these results, the depth of the amorphous silicon deposition.

A. *Electron Energy Distribution Function* – Despite the fact that silane is present at less than 5% of the gas concentration, it does impact the distribution function. This is because the thresholds for ionization, dissociation, and vibrational excitation all are lower in silane than they are in hydrogen. Because the electron number density tends to fall off exponentially with increasing energy, the lower thresholds for the electron impact processes for silane overcomes to some degree the effect of the low fractional concentration of the silane. To illustrate the evolution of the electron energy distribution function we show in Figures 42a., b., c., and d. the distribution function respectively very soon after turn-on (1.75×10^{-8}s), at near 1 μs after turn-on, at approximately 0.1 ms, and finally at the end of the run, ~ 0.01 s. At the earliest time (42a.) the electron density is still low (~10^5 cm^{-3}) and the available energy is shared fairly evenly among the electrons. Thus, we have a flat energy profile with a very high average electron energy, ~29 ev. This high energy rapidly ionizes the gas further and by a microsecond (42b.) the electron number density has increased above 10^8 cm^{-3} and the average electron energy has dropped to about 4 ev. By about a tenth of a millisecond (42c.) the electron density has risen to ~10^9 cm^{-3} and the average energy is 2.3 ev. These values are nearly the equilibrium values that we see at 42d., electron number density ~ 1.8×10^9 cm^{-3} and average energy = 2.15 ev.

B. *Neutral Specie Evolution* – The major neutral species are shown in plots 43a., b., c., d., and e. The critical radical, for our purposes is SiH_3 and in plot 43a. it is shown as it evolves out to 0.03 s, where it has essentially reached steady state equilibrium. Its concentration is a few percent of the silane concentration. Other major species critical to the chemical evolution are atomic hydrogen, H, and disilane (Si_2H_6). In plot 43b., we show the first two vibrational states of hydrogen. $H_2(v{=}1)$, in particular, builds up to a density higher than that of any of the radicals and does have an impact on the chemistry. Several radicals are produced in appreciable quantities, such as Si_2H_5 (43c.) and Si_3H_5 (43e.).

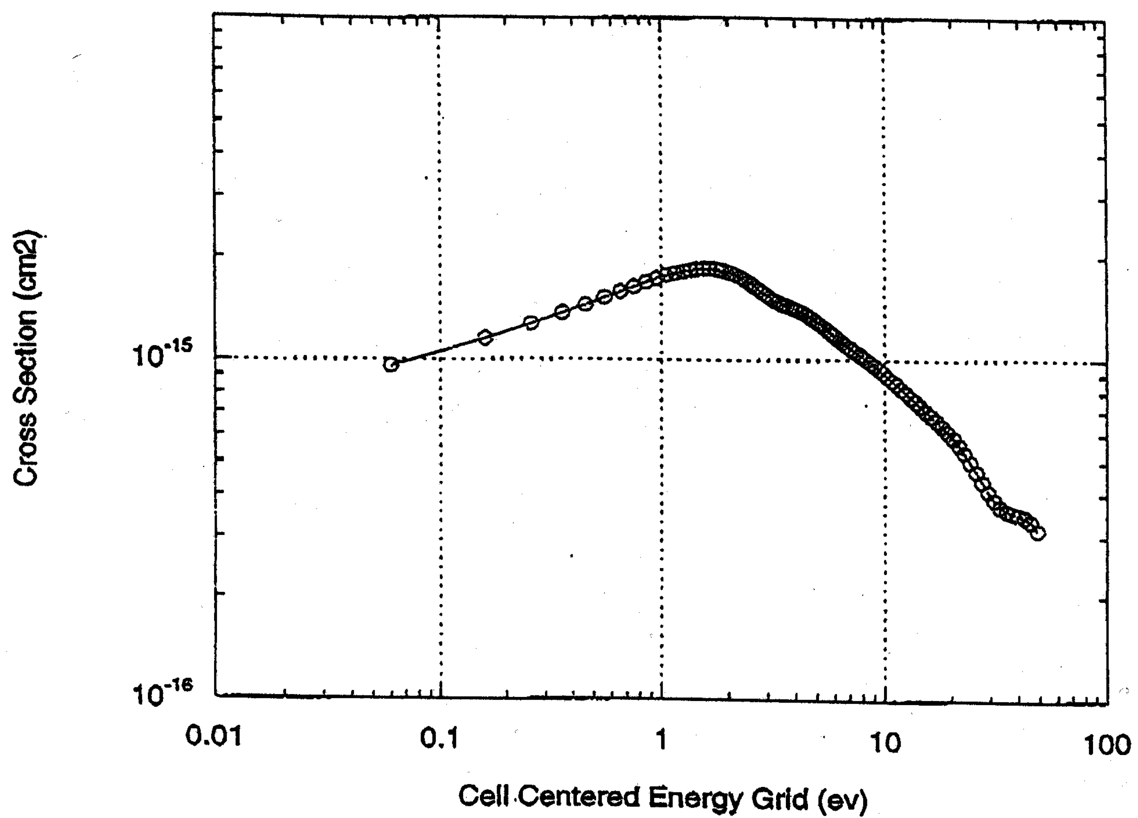

Figure 40a. **Electron Impact Cross Sections (cm^2): a. H_2 momentum transfer.**

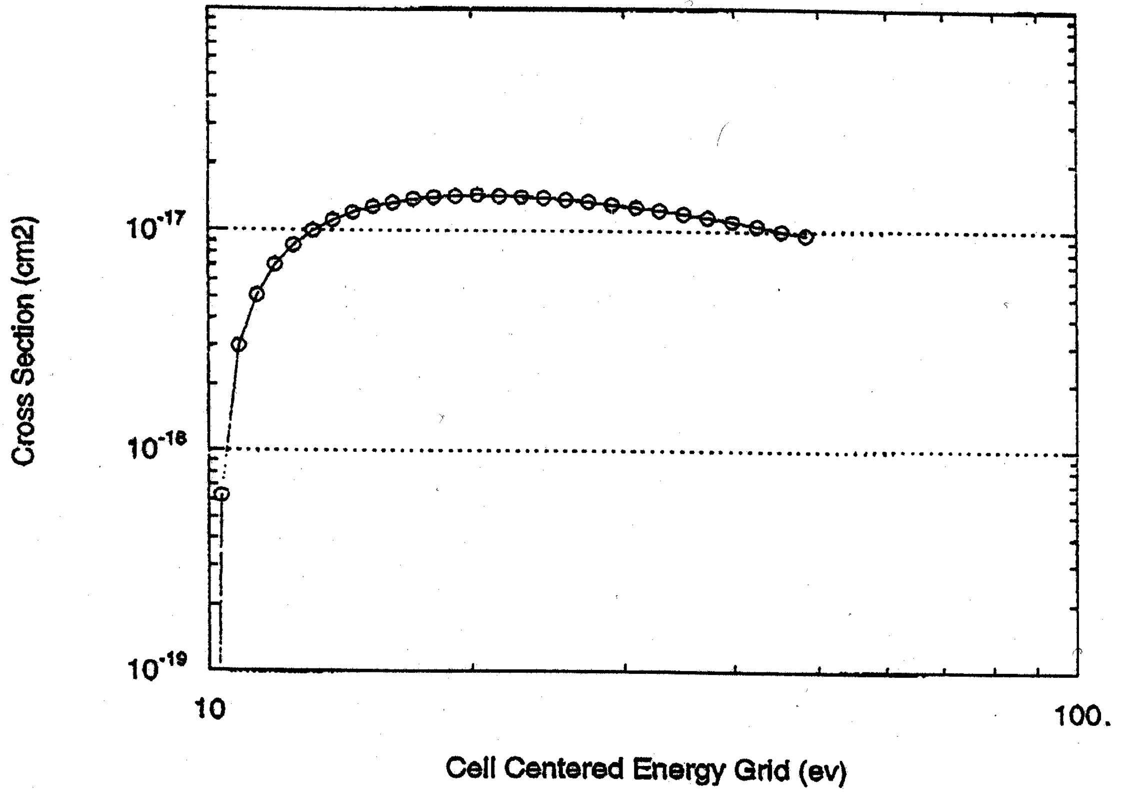

Figure 40b. **Electron Impact Cross Sections (cm^2): Lowest threshold H optical excitation.**

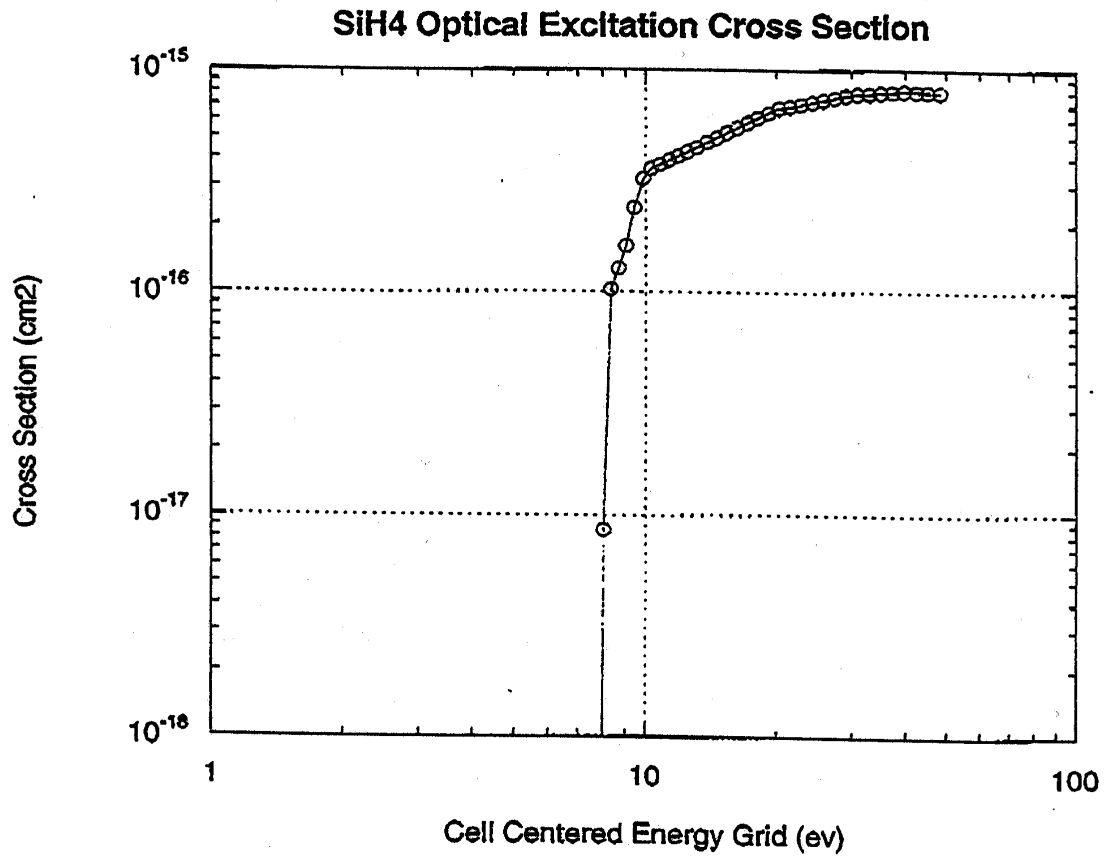

Figure 40c. Electron Impact Cross Sections (cm^2): SiH_4 optical excitation.

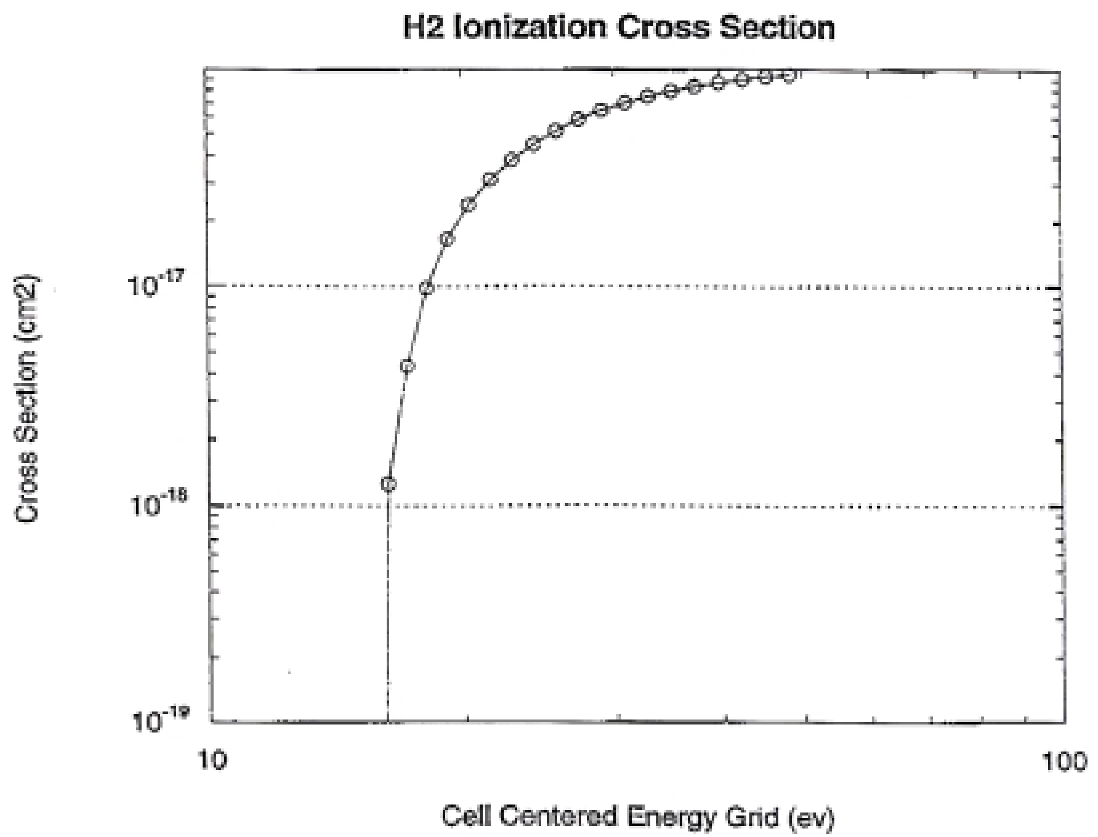

Figure 40d. **Electron Impact Cross Sections (cm^2): H_2 Ionization.**

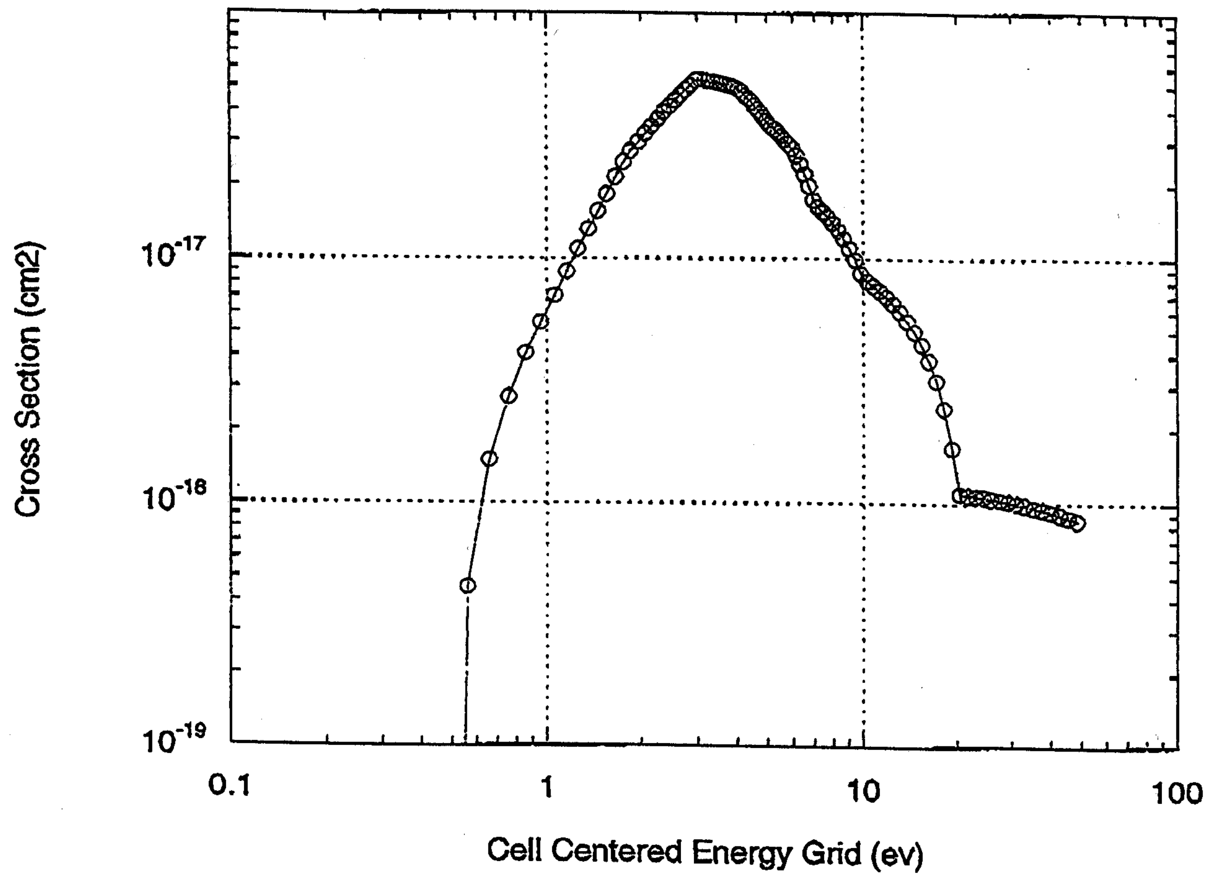

Figure 40e. **Electron Impact Cross Sections (cm^2): Lowest threshold H_2 vibrational excitation.**

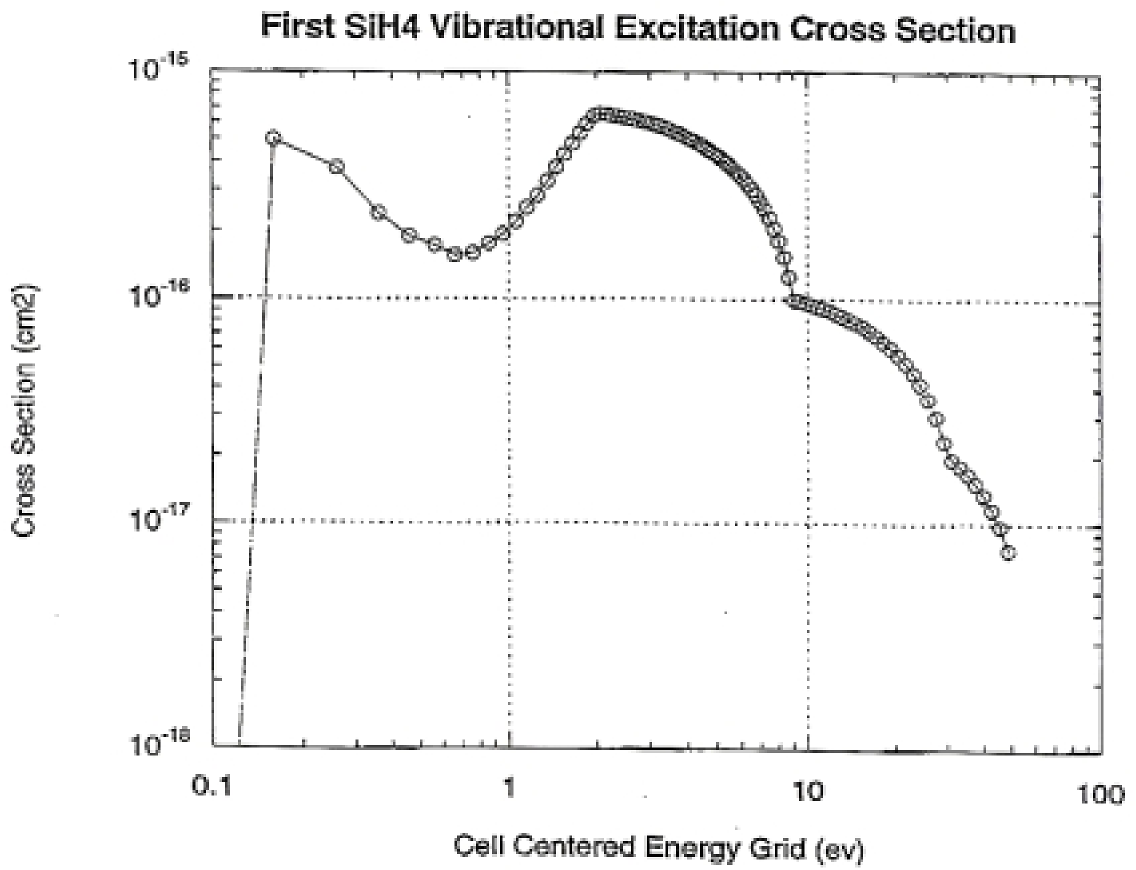

Figure 40f. **Electron Impact Cross Sections (cm^2): Lowest threshold SiH_4 vibrational excitation.**

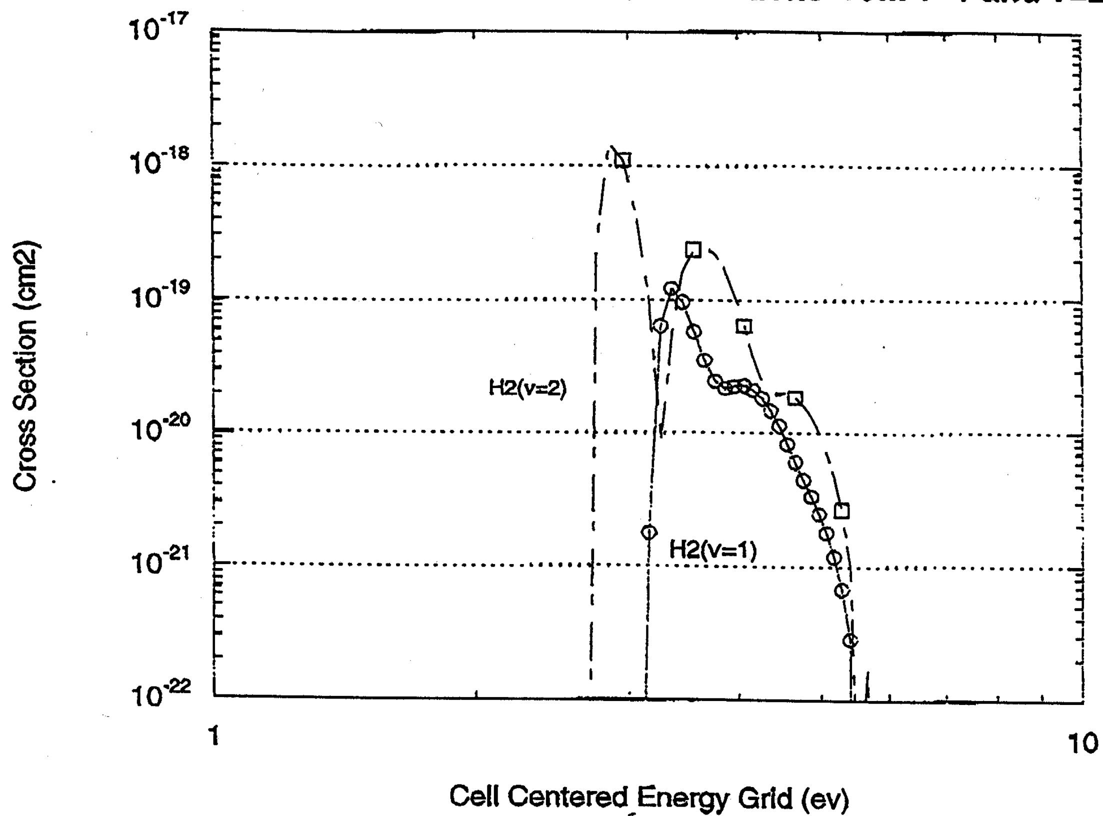

Figure 40g. **Electron Impact Cross Sections (cm^2):**
Dissociative attachment from the v=1 and v=2 vibrational states of H_2.

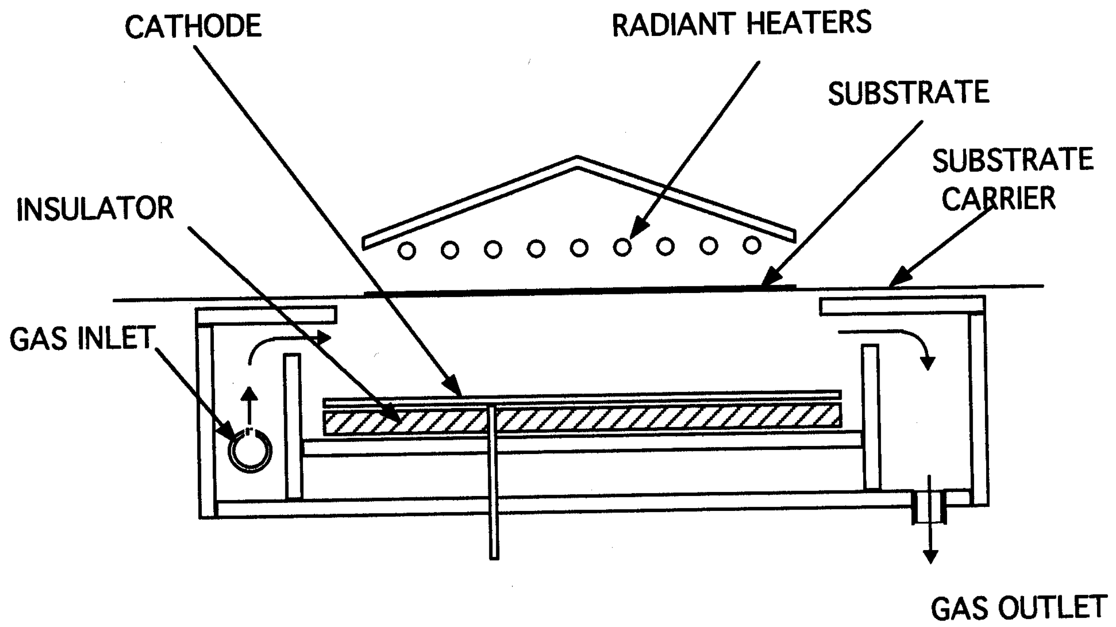

JD 9-16-99

Figure 41 Modeled RF Reactor Subchamber Design

C. *Positive Ion Evolution* – Figures 44a., b., and c. show the generation of the positive ions. Initially, H_2^+, H_3^+, SiH_3^+, and SiH_2^+ are the major positive ions as a direct result of ionization of H_2 and SiH_4 but there is a rapid evolution toward the heavier ions, including $Si_2H_7^+$, $Si_3H_7^+$, $Si_3H_6^+$, and $Si_3H_5^+$. These dominate by a millisecond or earlier.

C. *Negative Ion Evolution* – Figure 45 shows the negative ion evolution. As with the positive ions we start with SiH_3^-, a result of dissociative attachment of an electron reacting with silane, as the dominant ion. Again there is the conversion to heavier ions and by 0.01 s $Si_3H_7^-$ dominates.

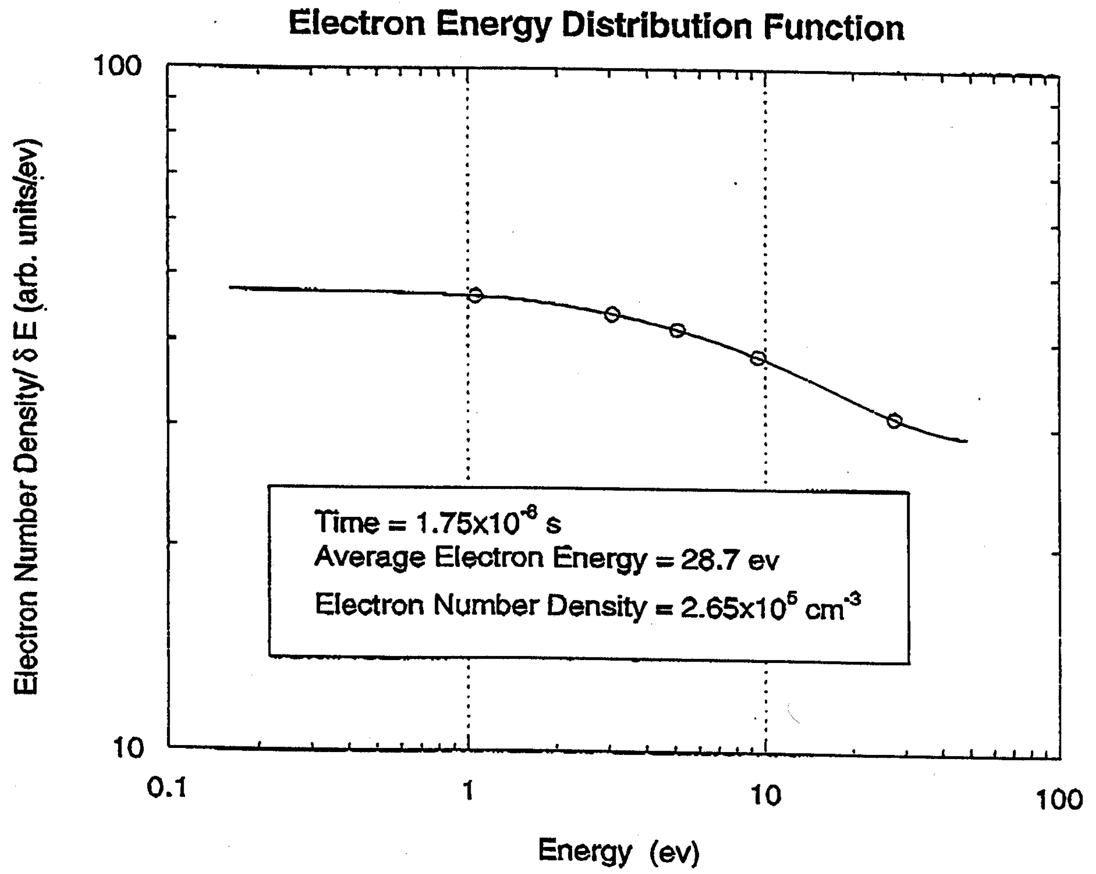

Figure 42a. Electron energy distribution functions at various times after turn-on: a. 1.75×10^{-8} s.

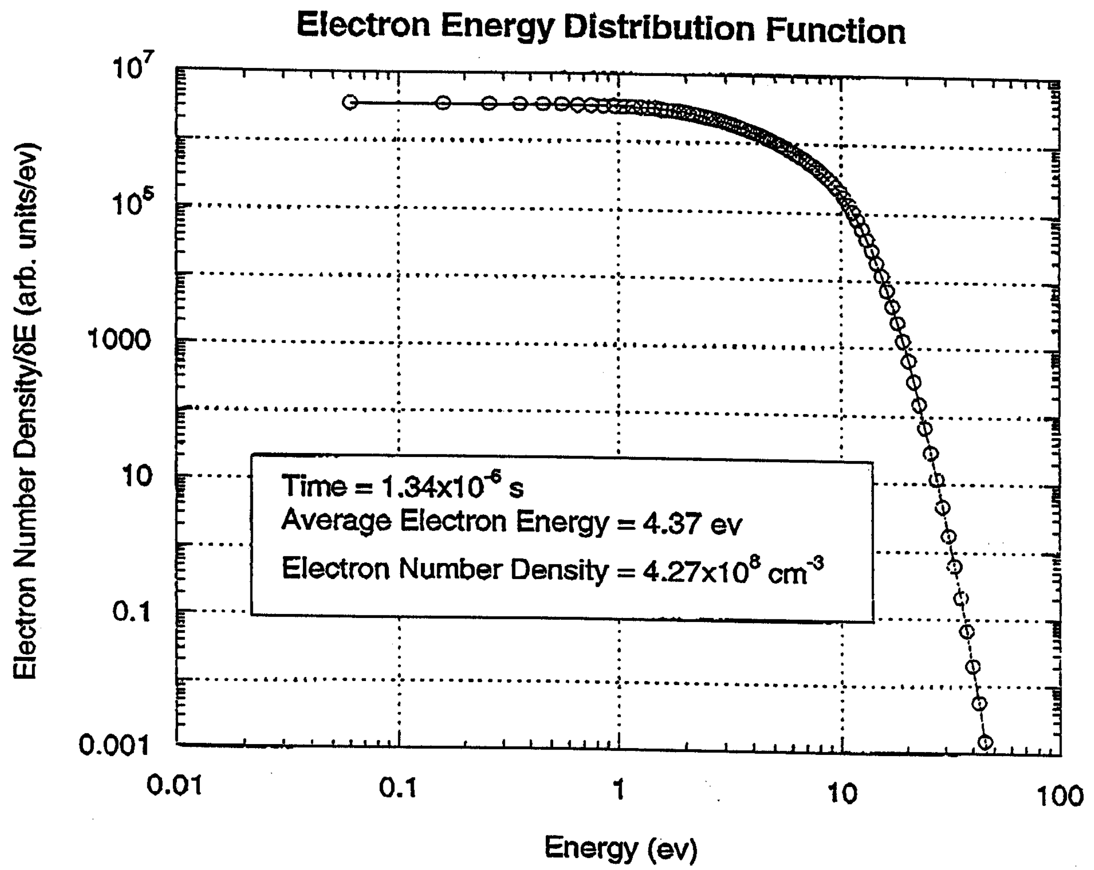

Figure 42b. **Electron energy distribution functions at various times after turn-on: b. 1.34×10^{-6} s.**

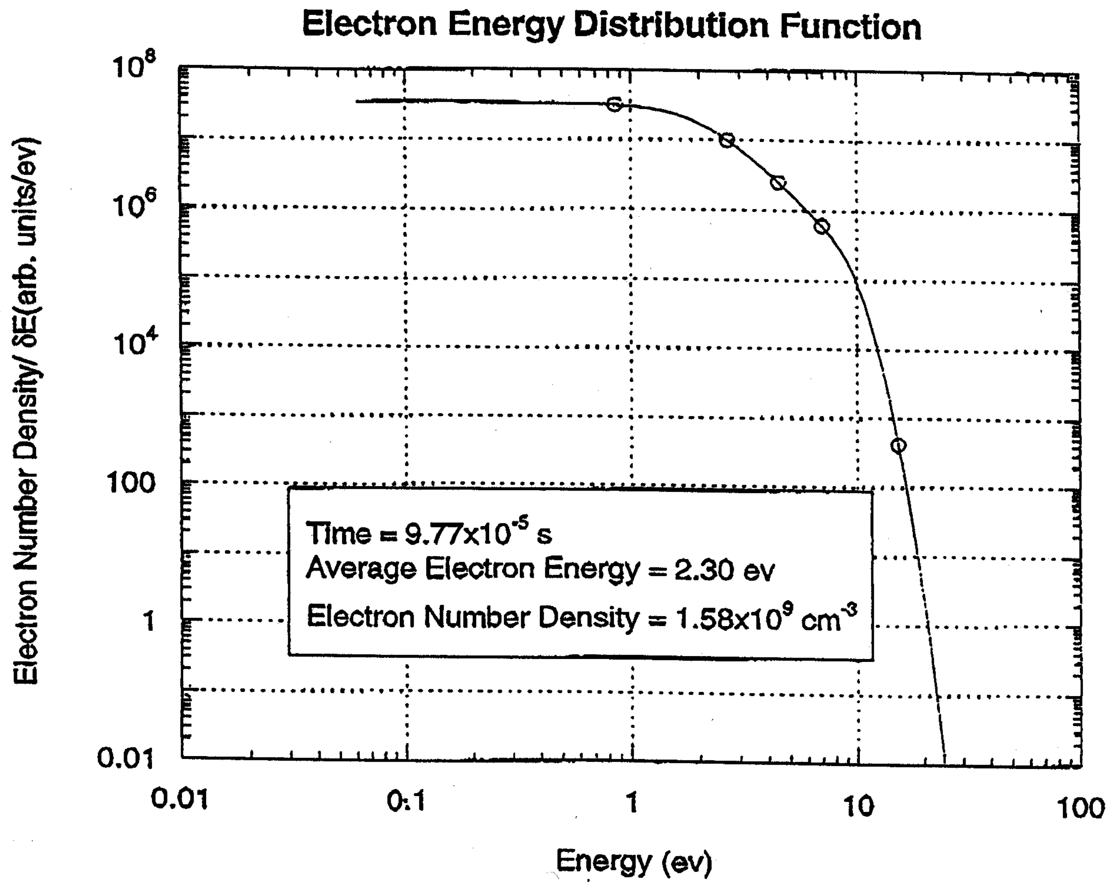

Figure 42c. Electron energy distribution functions at various times after turn-on: c. 9.77×10^{-5} s.

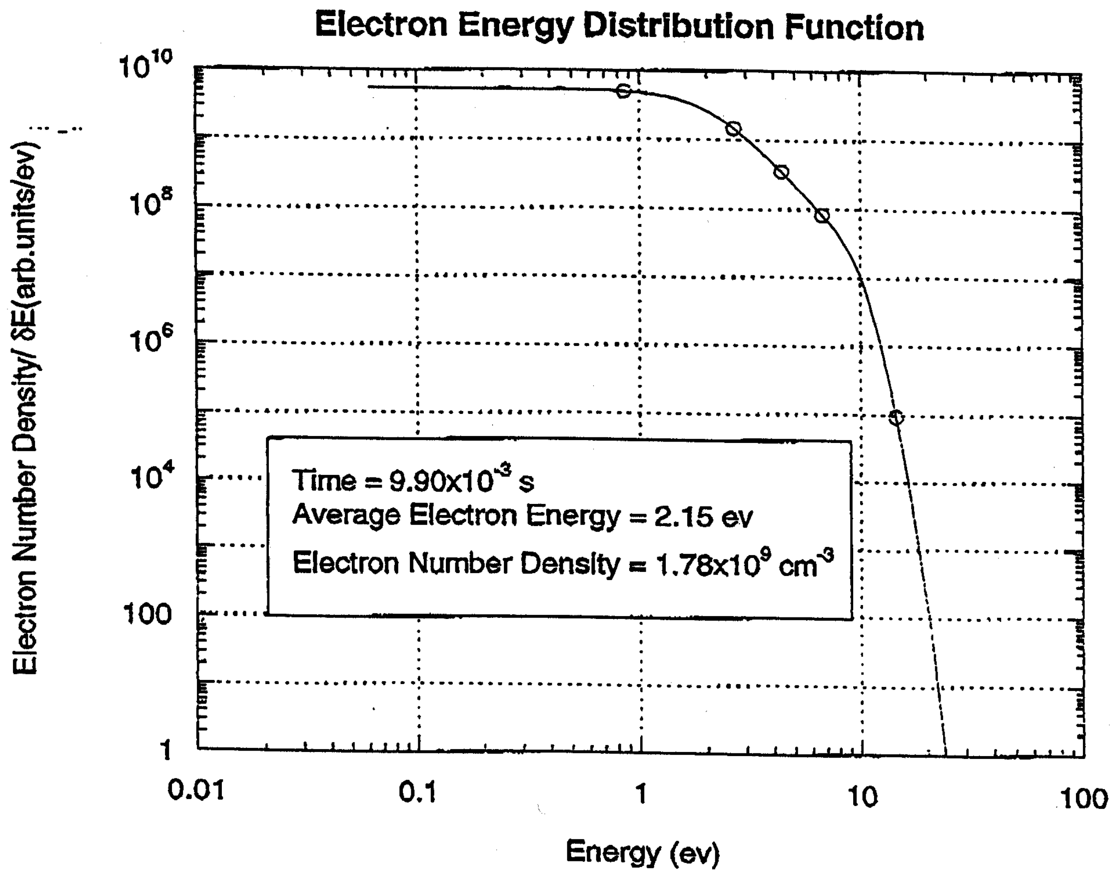

Figure 42d. **Electron energy distribution functions at various times after turn-on: d. 9.90×10^{-3} s.**

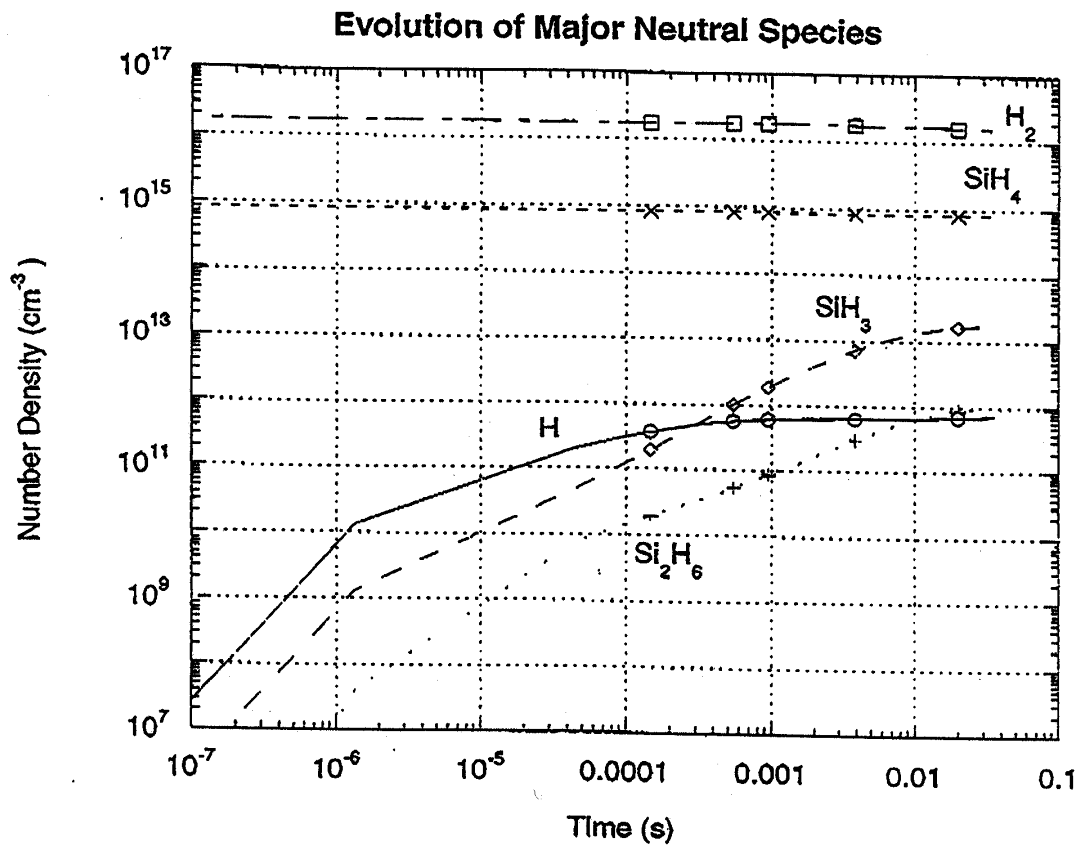

Figure 43a. **Evolution of Neutral Species (cm^{-3}): a. H_2, SiH_4, H, SiH_3, Si_2H_6.**

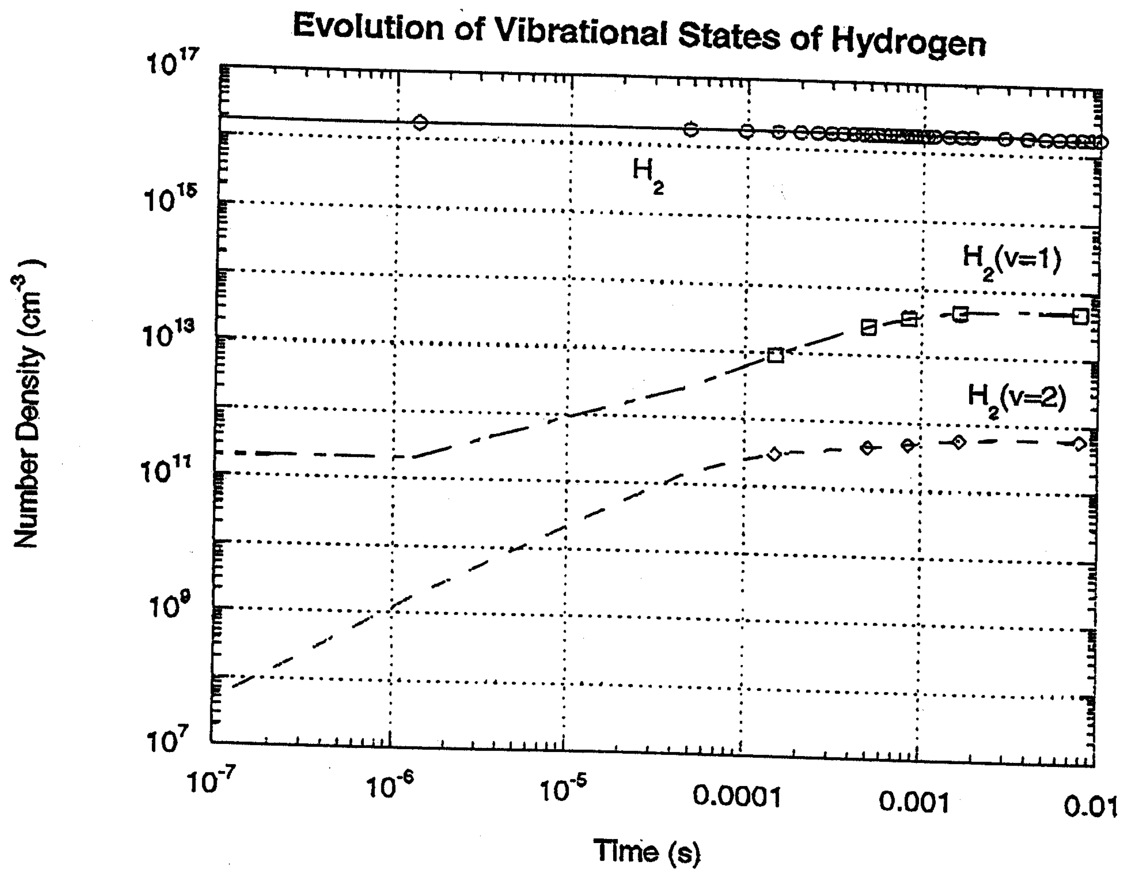

Figure 43b. **Evolution of Neutral Species (cm^{-3}):**
b. H_2, $H_2(v=1)$, $H_2(v=2)$.

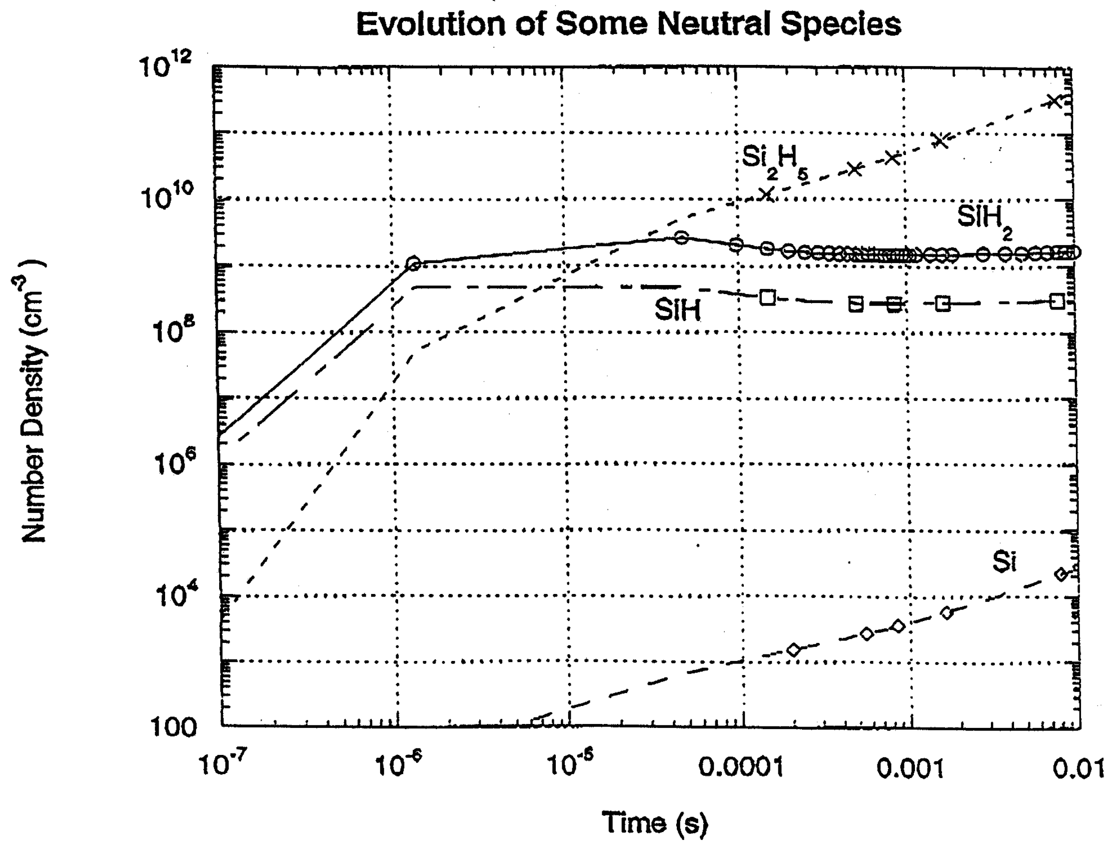

Figure 43c. **Evolution of Neutral Species (cm^{-3}): c. Si_2H_5, SiH_2, SiH, Si.**

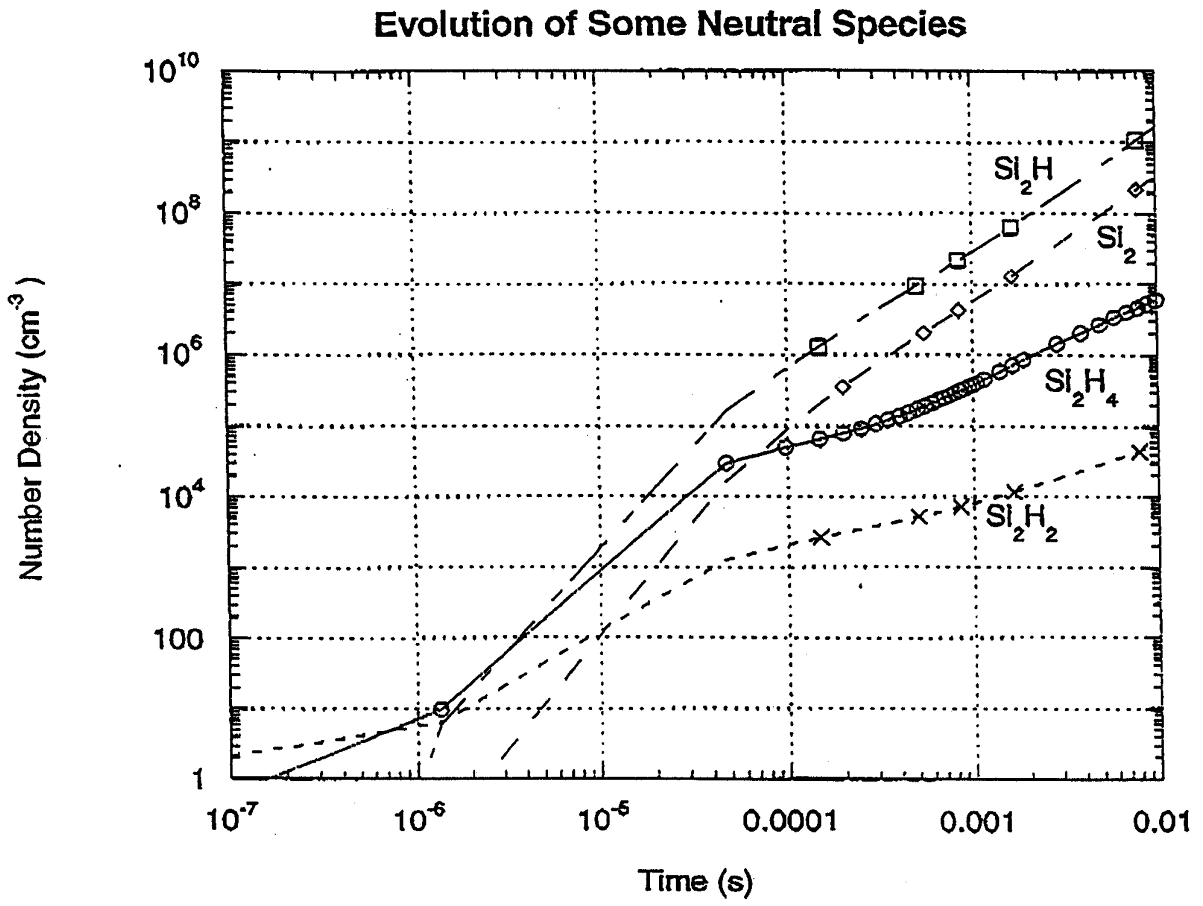

Figure 43d. **Evolution of Neutral Species (cm^{-3}):**
d. Si_2H_4, Si_2H_2, Si_2H, Si_2.

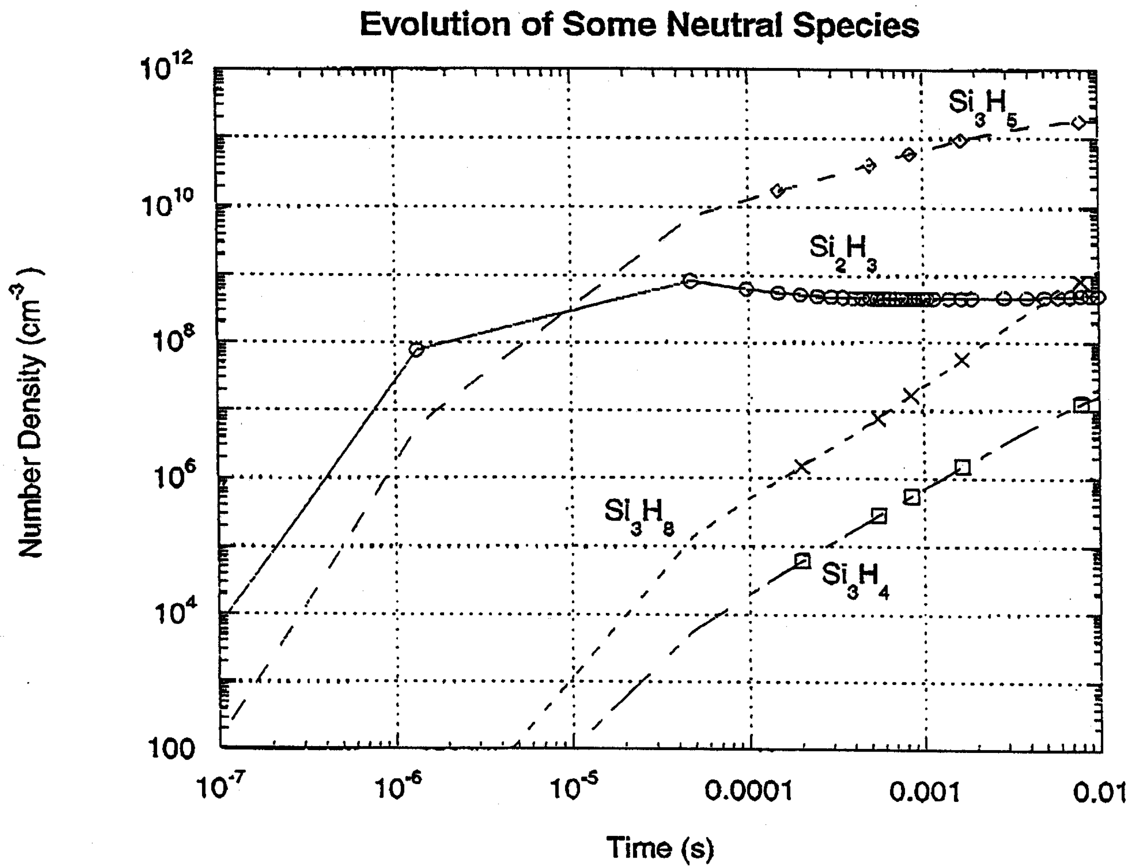

Figure 43e. **Evolution of Neutral Species (cm^{-3}): e. Si_2H_3, Si_3H_8, Si_3H_5, Si_3H_4.**

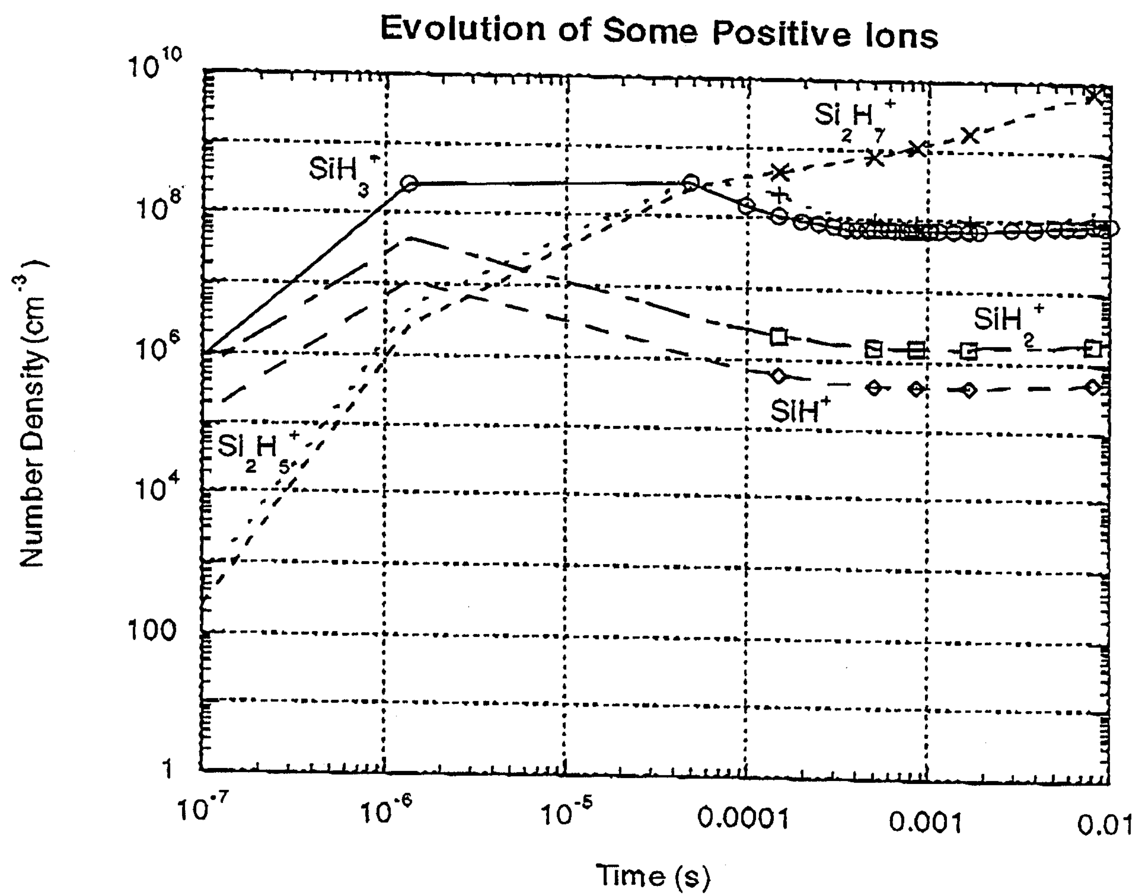

Figure 44a. Evolution of Positive Ions (cm^3):
a. SiH_3^+, SiH_2^+, SiH^+, $Si_2H_7^+$, $Si_2H_5^+$.

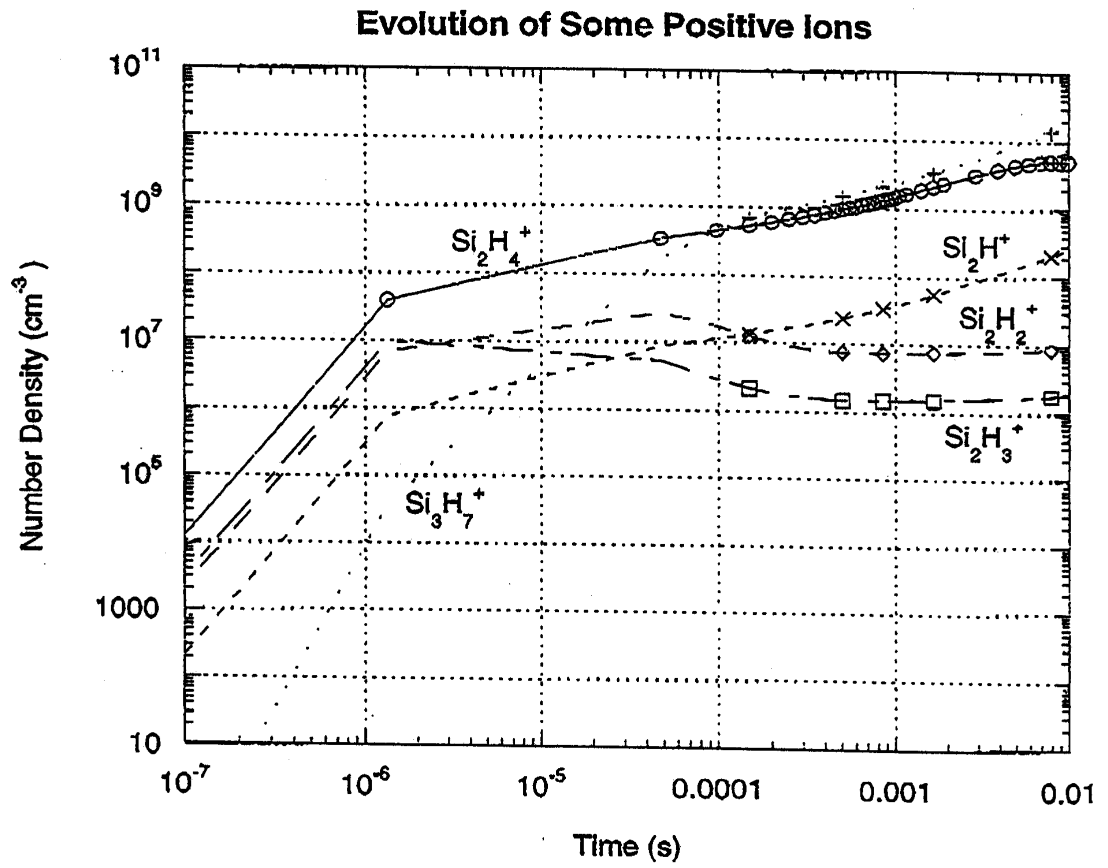

Figure 44b. **Evolution of Positive Ions (cm^{-3}):**
b. $Si_2H_4^+$, $Si_2H_3^+$, $Si_2H_2^+$, Si_2H^+, $Si_3H_7^+$

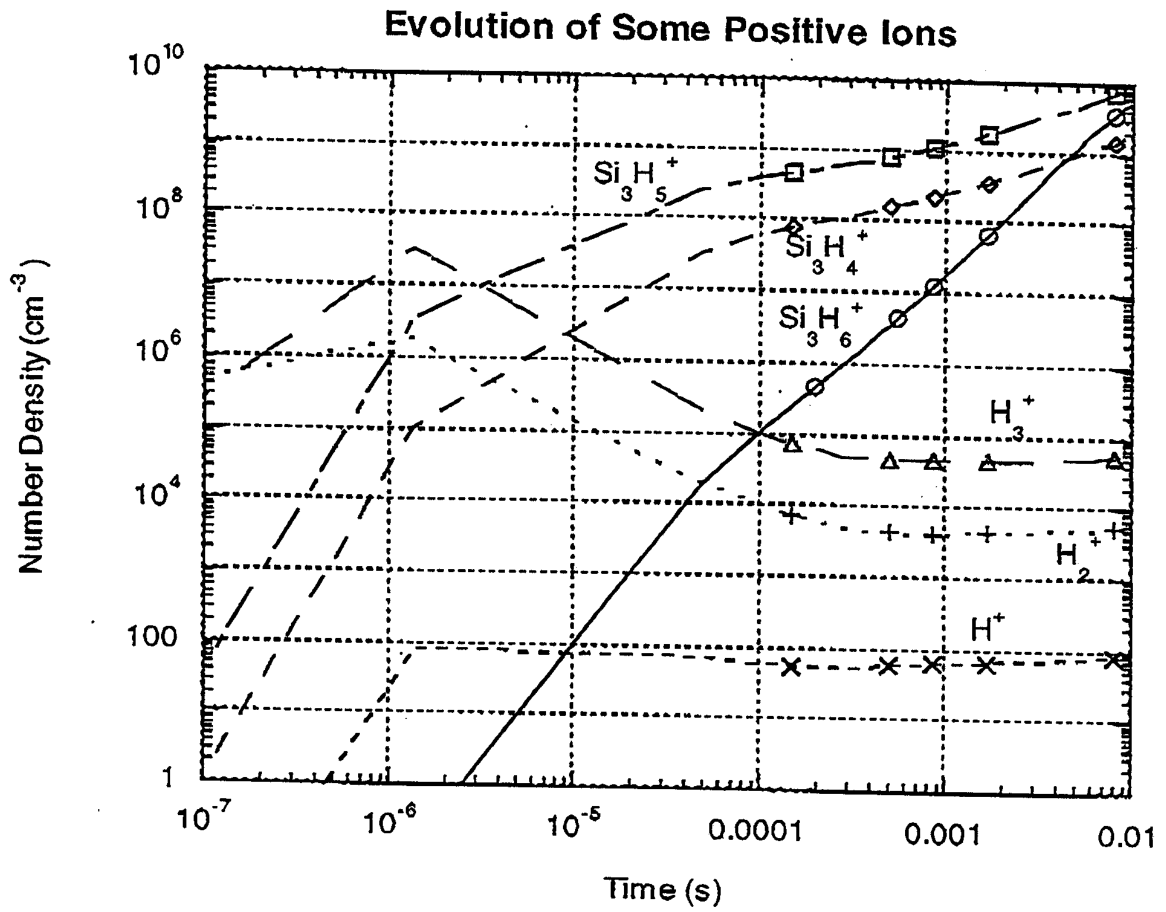

Figure 44c. **Evolution of Positive Ions (cm^{-3}):**
c. $Si_3H_6^+$, $Si_3H_5^+$, $Si_3H_4^+$, H_3^+, H_2^+, H^+.

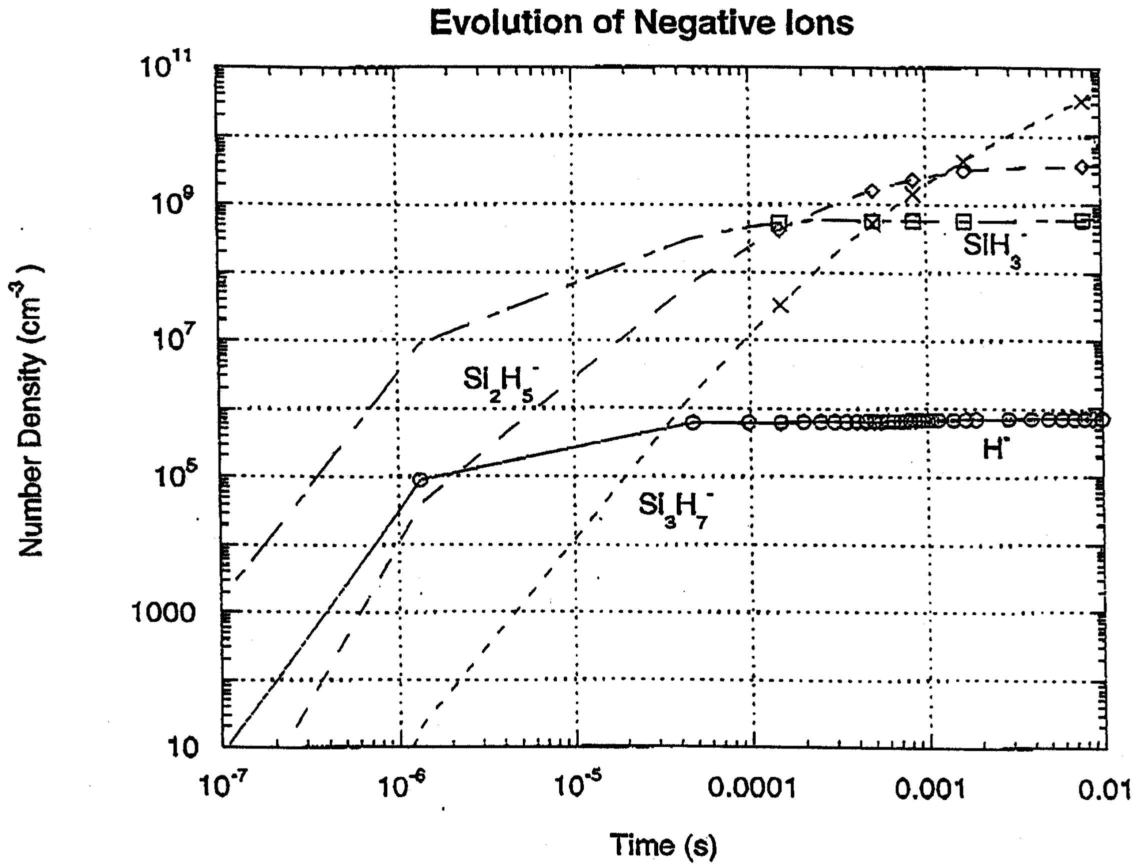

Figure 45. **Evolution of Negative Ions (cm^{-3}) : H^-, SiH_3^-, $Si_2H_5^-$, $Si_3H_7^-$.**

D. *Electron Density and Energy* – Figure 46 shows the evolution of the positive and negative ions and the electrons. Initially the electron density and positive ion density are equal to one another. As early as a few microseconds the electron density has come close to its equilibrium value ~ 10^9 cm^{-3}. The positive ions continue to increase and charge is conserved by the increase in the negative ions. Figure 47 shows a plot of the variation in the average electron energy with time. It reaches its equilibrium value, ~ 2 ev, by a few tenths of a millisecond.

E. *Amorphous Silicon Deposition* – The bottom line of the above simulation is comparison with measured data for the thickness of the deposition of amorphous silicon. To calculate this we need to know the density of amorphous silicon. According to the Handbook of Chemistry and Physics the value is 2.35 g/cm^3. Since silicon has an atomic weight of 28, the number of moles/cm^3 of amorphous silicon is 2.35/28 = 0.084 and the number of molecules/cm^3 is $N_m = 0.084 x 6.02 x 10^{23} = 5.05 x 10^{22}$, where we have used Avogadro's Number (=6.02 x 10^{23}).

To calculate the number of molecules of amorphous silicon on the substrate we need to know the flux of SiH_3 reaching the surface and we need to multiply that by the sticking coefficient. The measured sticking coefficient for SiH_3 in the published research data is 0.28. Because we are limited to a one-point calculation, we will assume that all of the gas originates from one point in the center of the reactor and that it diffuses from there to the substrate. To get the flux we need to calculate the diffusion velocity of SiH_3 through H_2. This is given by $V_d(SiH_3)$:

$$V_d(SiH_3) = (\nabla[SiH_3]/[SiH_3]) \text{ x } D(SiH_3,H_2) \text{ x } (\text{total gas density}/(15.5[SiH_3] + [H_2]))$$

In the first factor in the above expression, the gradient of SiH_3 between the center of the reactor and the substrate is calculated based on the assumption that, since at the substrate 28% of the molecules stick, there is just 72% of the SiH_3 density there as there is at the center. This gives for the first factor in the above expression, $0.28/\Delta x$, where Δx is the distance between the center of the reactor and the substrate (1.9 cm). The second factor, D, is the diffusion coefficient for SiH_3 diffusing through H_2. This is given approximately by $0.09(T_g)^{3/2}/p$, where T_g is the gas temperature in degrees Kelvin and p is the pressure in Torr. We take the gas temperature to be 523 K and the pressure to be 1 Torr. The last factor accounts for the need for overall mass balance in the diffusion process. From the simulation results we take the total gas density to be $1.8x10^{16}$ cm^{-3}, the density of SiH_3 as $1.9x10^{13}$ cm^{-3}, and the hydrogen density as $1.7x10^{16}$ cm^{-3}. When all the numbers are put in we find the diffusion velocity for SiH_3 to be 165 cm/s.

The number of molecules, N, sticking to the surface per square centimeter per second then is:

$$N = 0.28 \text{ x } V_d(SiH_3) \text{ x } [SiH_3] = 8.8x10^{14} \text{ molecules/cm}^2\text{/s}$$

The thickness of the deposition of amorphous silicon, δ, is then:

$$\delta = N \text{ x } \Delta t / N_m = 8.8x10^{14} \text{ x } 2.1x10^3 / 5.05x10^{22} = 3.7x10^{-5} \text{ cm}$$

The factor Δt is the run time, which was 35 minutes or $2.1x10^3$ s. The measured thickness of the deposition at the center of the substrate is 3.1 nanometers = $3.1x10^{-5}$ cm (see Figure 48). The discrepancy between measured value and simulation is 19%. Keeping in mind the crudeness of the simulation, based on a one-point model in which the SiH_3 is assumed to originate at one location at the center of the reactor and the neglect of ion effects, the agreement is remarkably good.

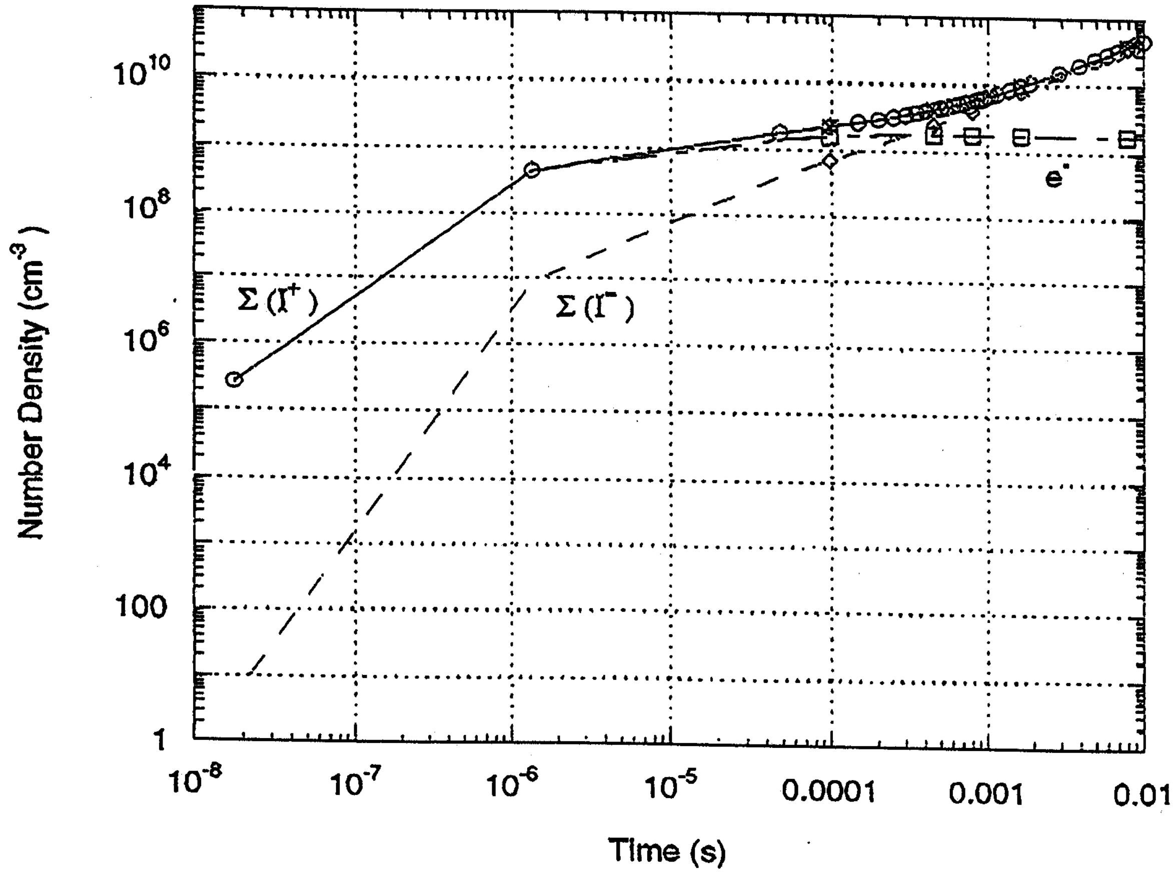

Figure 46. Evolution of Positive and Negative Ions and Electrons (cm^{-3}): total positive ions, total negative ions, electrons.

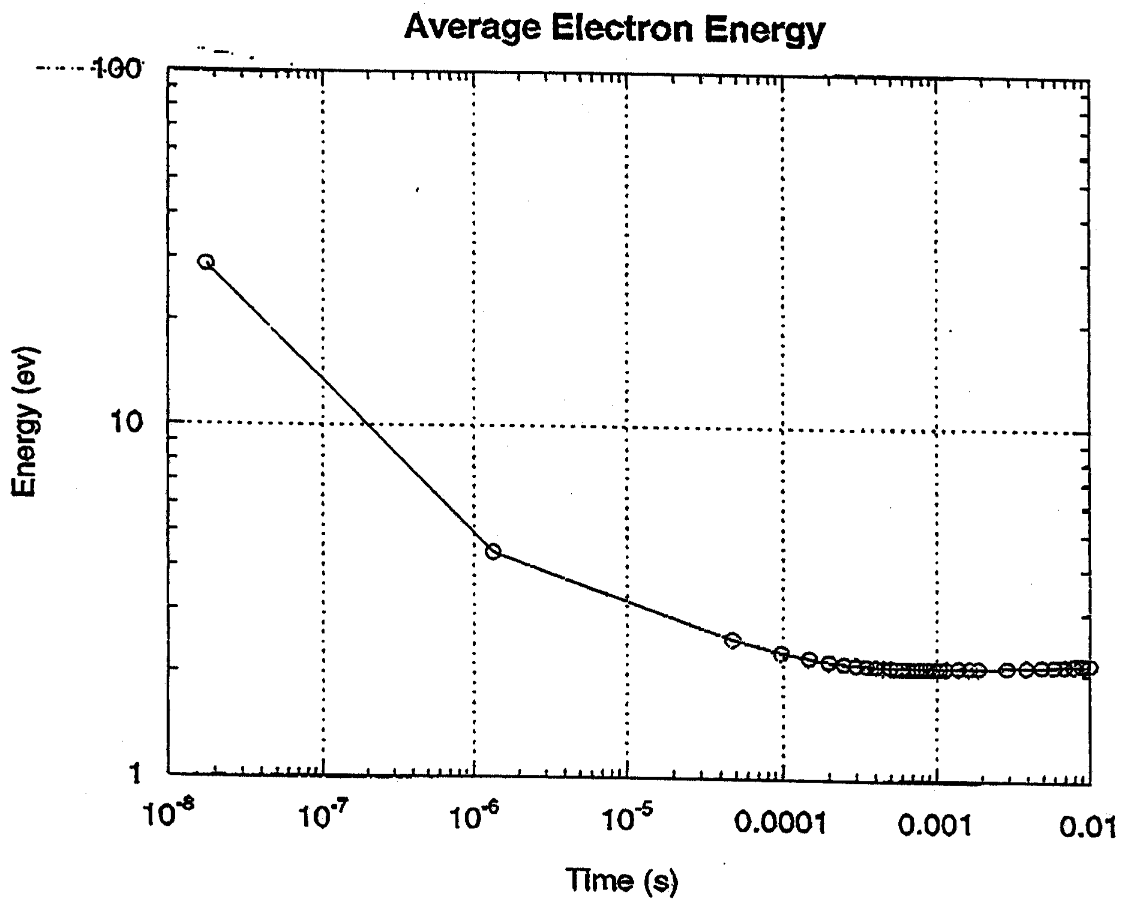

Figure 47. Evolution of Average Electron Energy (ev).

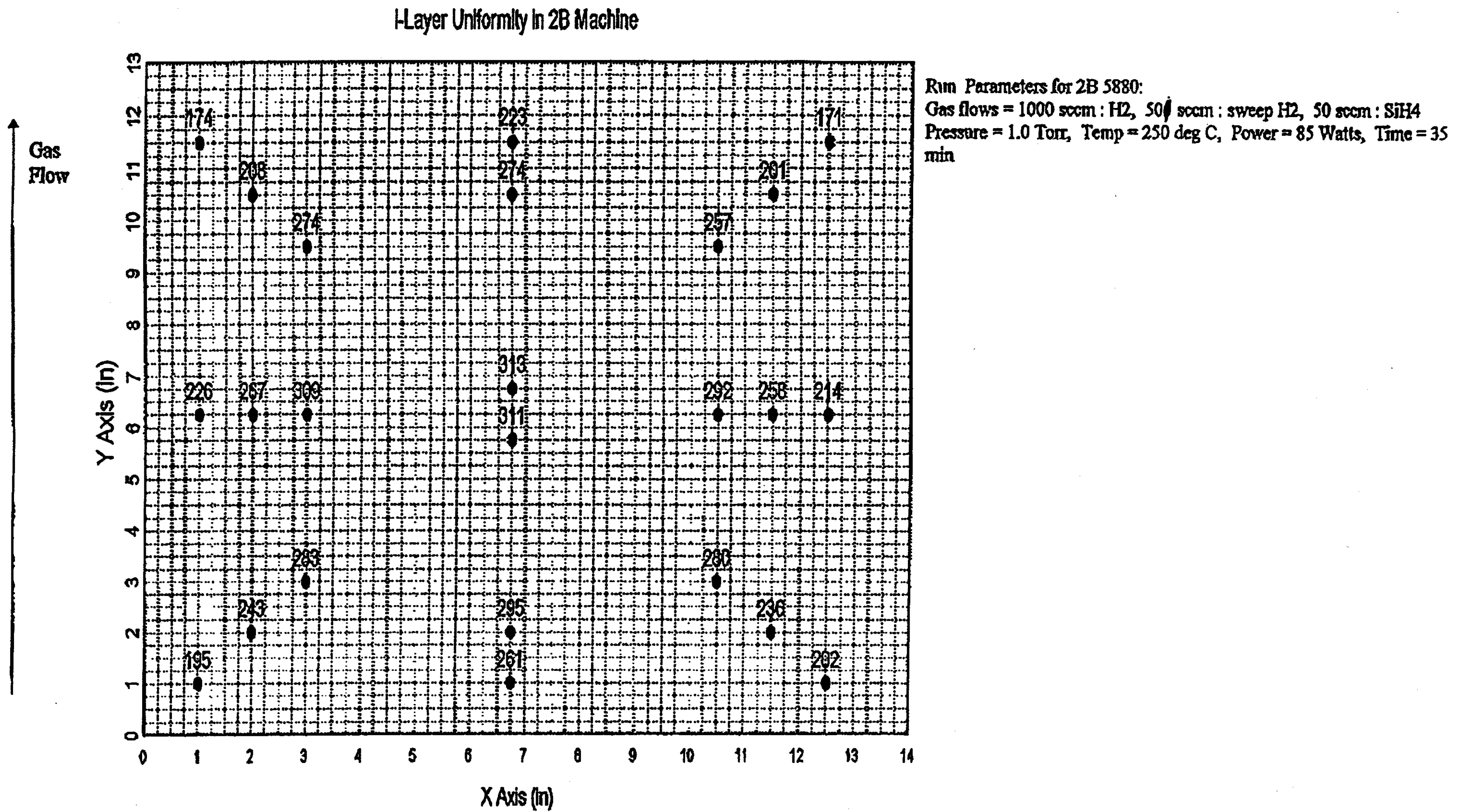

Figure 48. Measured Thickness of Amorphous Silicon Deposition (nm) in Reactor.

REPORT DOCUMENTATION PAGE

Form Approved
OMB NO. 0704-0188

Public reporting burden for this collection of information is estimated to average 1 hour per response, including the time for reviewing instructions, searching existing data sources, gathering and maintaining the data needed, and completing and reviewing the collection of information. Send comments regarding this burden estimate or any other aspect of this collection of information, including suggestions for reducing this burden, to Washington Headquarters Services, Directorate for Information Operations and Reports, 1215 Jefferson Davis Highway, Suite 1204, Arlington, VA 22202-4302, and to the Office of Management and Budget, Paperwork Reduction Project (0704-0188), Washington, DC 20503.

1. AGENCY USE ONLY (Leave blank)	2. REPORT DATE	3. REPORT TYPE AND DATES COVERED
	November 1999	Annual Technical Progress Report, 22 June 1998 – 21 June 1999

4. TITLE AND SUBTITLE
Efficiency and Throughput Advances in Continuous Roll-to-Roll a-Si Alloy PV Manufacturing Technology; Annual Technical Progress Report, 22 June 1998 – 21 June 1999

5. FUNDING NUMBERS
C: ZAX-8-17647-09
TA: PV006101

6. AUTHOR(S)
M. Izu

7. PERFORMING ORGANIZATION NAME(S) AND ADDRESS(ES)
Energy Conversion Devices, Inc.
1675 W. Maple Road
Troy, MI 48084

8. PERFORMING ORGANIZATION REPORT NUMBER

9. SPONSORING/MONITORING AGENCY NAME(S) AND ADDRESS(ES)
National Renewable Energy Laboratory
1617 Cole Blvd.
Golden, CO 80401-3393

10. SPONSORING/MONITORING AGENCY REPORT NUMBER
SR-520-27535

11. SUPPLEMENTARY NOTES
NREL Technical Monitor: R.L. Mitchell

12a. DISTRIBUTION/AVAILABILITY STATEMENT
National Technical Information Service
U.S. Department of Commerce
5285 Port Royal Road
Springfield, VA 22161

12b. DISTRIBUTION CODE

13. ABSTRACT *(Maximum 200 words)*
This document reports on work performed by Energy Conversion Devices, Inc. (ECD) during Phase I of this subcontract. During this period, ECD researchers:
1. Completed design and construction of new, improved substrate heater.
2. Tested and verified improved performance of the new substrate heater in the pilot machine.
3. Verified improved performance of the new substrate heater in the production machine.
4. Designed and bench-tested a new infrared temperature sensor.
5. Installed a prototype new infrared temperature sensor in the production machine for evaluation.
6. Designed a new rolling thermocouple temperature sensor.
7. Designed and bench-tested a reflectometer for the backreflector deposition machine.
8. Designed and bench-tested in-line non-contacting cell diagnostic sensor; PV capacitive diagnostic system.
9. Installed the in-line cell diagnostic sensor in the 5-MW a-Si deposition machine for evaluation.
10. Demonstrated a new low-cost zinc metal process in the pilot backreflector machine.
11. Fully tested a new cathode design for improved uniformity.

14. SUBJECT TERMS
photovoltaics ; Photovoltaic Manufacturing and Technology ; PVMaT ; process control ; reactive sputtering process ; substrate heaters ; temperature sensors ; reflectometers ; backreflector deposition

15. NUMBER OF PAGES

16. PRICE CODE

17. SECURITY CLASSIFICATION OF REPORT	18. SECURITY CLASSIFICATION OF THIS PAGE	19. SECURITY CLASSIFICATION OF ABSTRACT	20. LIMITATION OF ABSTRACT
Unclassified	Unclassified	Unclassified	UL